Hydrogen porosity interaction in a low alloy cast steel

Ahmed Yaktiti

N°d'ordre NNT : 2022LYSEM003

THESE de DOCTORAT DE L'UNIVERSITE DE LYON
opérée au sein de
l'Ecole des Mines de Saint-Etienne

Ecole Doctorale N° 488
Sciences, Ingénierie, Santé

Spécialité de doctorat : Sciences et Génie des Matériaux

Soutenue publiquement le 27/01/2022, par :

Ahmed YAKTITI

Interaction hydrogène-porosité dans un acier moulé faiblement allié

Hydrogen-porosity interaction in a low-alloy cast steel

Devant le jury composé de :

Nom, prénom	Grade	Etablissement	
DEPOVER, Tom	Professeur associé	Université de Ghent	Rapporteur
BOUHATTATE, Jamaa	Maitresse de conférences, HDR	Université de la Rochelle	Rapporteure
TANCRET, Franck	Professeur	Université de Nantes	Président du jury
CHRISTIEN, Frédéric	Professeur	Mines Saint-Etienne	Directeur de thèse
CARTON, Jean-François	Dr.-Ing	Safe Metal	Encadrant industriel
DHERS, Jean	Dr.-Ing HDR	Framatome	Invité
DREANO, Alixe	Maitre assistante	Mines Saint-Etienne	Invitée

Spécialités doctorales	Responsables	Spécialités doctorales	Responsables
SCIENCES ET GENIE DES MATERIAUX	K. Wolski Directeur de recherche	MATHEMATIQUES APPLIQUEES	M. Batton-Hubert
MECANIQUE ET INGENIERIE	S. Drapier, professeur	INFORMATIQUE	O. Boissier, Professeur
GENIE DES PROCEDES	F. Gruy, Maître de recherche	SCIENCES DES IMAGES ET DES	JC. Pinoli, Professeur
SCIENCES DE LA TERRE	B. Guy, Directeur de recherche	GENIE INDUSTRIEL	N. Absi, Maitre de recherche
SCIENCES ET GENIE DE	V. Laforest, Directeur de recherche	MICROELECTRONIQUE	Ph. Lalevée, Professeur

EMSE : Enseignants-chercheurs et chercheurs autorisés à diriger des thèses de doctorat (titulaires d'un doctorat d'État ou d'une

ABSI	Nabil	MR	Génie industriel	CMP
AUGUSTO	Vincent	MR	Génie industriel	CIS
AVRIL	Stéphane	PR	Mécanique et ingénierie	CIS
BADEL	Pierre	PR	Mécanique et ingénierie	CIS
BALBO	Flavien	PR	Informatique	FAYOL
BASSEREAU	Jean-François	PR	Sciences et génie des matériaux	SMS
BATTON-HUBERT	Mireille	PR	Mathématiques appliquées	FAYOL
BEIGBEDER	Michel	MA	Informatique	FAYOL
BILAL	Blayac	DR	Sciences et génie de l'environnement	SPIN
BLAYAC	Sylvain	PR	Microélectronique	CMP
BOISSIER	Olivier	PR	Informatique	FAYOL
BONNEFOY	Olivier	PR	Génie des Procédés	SPIN
BORBELY	Andras	DR	Sciences et génie des matériaux	SMS
BOUCHER	Xavier	PR	Génie Industriel	FAYOL
BRUCHON	Julien	PR	Mécanique et ingénierie	SMS
CAMEIRAO	Ana	PR	Génie des Procédés	SPIN
CHRISTIEN	Frédéric	PR	Science et génie des matériaux	SMS
DAUZERE-PERES	Stéphane	PR	Génie Industriel	CMP
DEBAYLE	Johan	MR	Sciences des Images et des Formes	SPIN
DEGEORGE	Jean-Michel	MA	Génie industriel	Fayol
DELAFOSSE	David	PR	Sciences et génie des matériaux	SMS
DELORME	Xavier	PR	Génie industriel	FAYOL
DESRAYAUD	Christophe	PR	Mécanique et ingénierie	SMS
DJENIZIAN	Thierry	PR	Science et génie des matériaux	CMP
BERGER-DOUCE	Sandrine	PR	Sciences de gestion	FAYOL
DRAPIER	Sylvain	PR	Mécanique et ingénierie	SMS
DUTERTRE	Jean-Max	PR	Microélectronique	CMP
EL MRABET	Nadia	MA	Microélectronique	CMP
FAUCHEU	Jenny	MA	Sciences et génie des matériaux	SMS
FAVERGEON	Loïc	MR	Génie des Procédés	SPIN
FEILLET	Dominique	PR	Génie Industriel	CMP
FOREST	Valérie	PR	Génie des Procédés	CIS
FRACZKIEWICZ	Anna	DR	Sciences et génie des matériaux	SMS
GAVET	Yann	MA	Sciences des Images et des Formes	SPIN
GERINGER	Jean	MA	Sciences et génie des matériaux	CIS
GONDRAN	Natacha	MA	Sciences et génie de l'environnement	FAYOL
GONZALEZ FELIU	Jesus	MA	Sciences économiques	FAYOL
GRAILLOT	Didier	DR	Sciences et génie de l'environnement	SPIN
GRIMAUD	Frederic	EC	Génie mathématiques et industriel	FAYOL
GROSSEAU	Philippe	DR	Génie des Procédés	SPIN
GRUY	Frédéric	PR	Génie des Procédés	SPIN
HAN	Woo-Suck	MR	Mécanique et ingénierie	SMS
HERRI	Jean Michel	PR	Génie des Procédés	SPIN
ISMAILOVA	Esma	MC	Microélectronique	CMP
KERMOUCHE	Guillaume	PR	Mécanique et Ingénierie	SMS
KLOCKER	Helmut	DR	Sciences et génie des matériaux	SMS
LAFOREST	Valérie	DR	Sciences et génie de l'environnement	FAYOL
LERICHE	Rodolphe	DR	Mécanique et ingénierie	FAYOL
LIOTIER	Pierre-Jacques	MA	Mécanique et ingénierie	SMS
MEDINI	Khaled	EC	Sciences et génie de l'environnement	FAYOL
MOLIMARD	Jérôme	PR	Mécanique et ingénierie	CIS
MOULIN	Nicolas	MA	Mécanique et ingénierie	SMS
MOUTTE	Jacques	MR	Génie des Procédés	SPIN
NAVARRO	Laurent	MR	Mécanique et ingénierie	CIS
NEUBERT	Gilles	PR	Génie industriel	FAYOL
NIKOLOVSKI	Jean-Pierre	Ingénieur de recherche	Mécanique et ingénierie	CMP
O CONNOR	Rodney Philip	PR	Microélectronique	CMP
PICARD	Gauthier	PR	Informatique	FAYOL
PINOLI	Jean Charles	PR	Sciences des Images et des Formes	SPIN
POURCHEZ	Jérémy	DR	Génie des Procédés	CIS
ROUSSY	Agnès	MA	Microélectronique	CMP
SANAUR	Sébastien	MA	Microélectronique	CMP
SERRIS	Eric	IRD	Génie des Procédés	FAYOL
STOLARZ	Jacques	CR	Sciences et génie des matériaux	SMS
VALDIVIESO	François	PR	Sciences et génie des matériaux	SMS
VIRICELLE	Jean Paul	DR	Génie des Procédés	SPIN
WOLSKI	Krzystof	DR	Sciences et génie des matériaux	SMS
XIE	Xiaolan	PR	Génie industriel	CIS
YUGMA	Gallian	MR	Génie industriel	CMP

Mise à jour : 04/02/2021

Acknowledgements

First of all, I would like to express my deepest gratitude to all the committee members for their insightful discussions and helpful suggestions in particular Dr. Jamaa BOUHATTATE and Dr. Tom DEPOVER for reviewing this manuscript. I really appreciate all the comments of the committee members that made my thesis better.

I am extremely grateful to my thesis supervisor Professor Frederic Christien for his invaluable advice, knowledge, time and assistance. Also, special thanks goes to Dr. Jean-François Carton, my industrial supervisor, for his useful suggestions and constructive criticisms. Thank you both for the helpful discussions, the supervision and the support over the years. Then, many thanks to Dr. Alixe Dreano for her insightful feedback and help, which allowed me to improve this thesis.

I take this opportunity to thank all the colleagues that I met during these three years and with whom I shared special moments. In addition, I would like to extend my sincere gratitude to everyone that was involved in my work in particular Claude Varillon, Gilles Blanc, Olivier Valfort, Maxime Minot, Claire Roume, Bernard Allirand, Marilyne Mondon and Yoann Garnier for their help and assistance.

Furthermore, from the bottom of my heart, my love and gratitude go to my wife, Islem Werghemi who is always by my side, encourages and supports me especially in hard times.

Finally, my warmest appreciations go to my parents who have encouraged me to continue my pursuit of higher education throughout my entire life.

Table of contents

General Introduction

A cast steel is a metallic product obtained by pouring molten steel into a mold cavity. After cooling, the product is removed from the mold and is usually heat treated in order to deliver the mechanical requirements that the customer demanded. Casting steels has the advantage of producing complex form components ranging from hundreds of grams to hundreds of tons [1]. Actually, cast steels are widely used in several areas such as energy, automotive, construction, mining… and due to the increasing demand for better mechanical properties, an extra effort has to be done to overcome certain issues, for instance hydrogen embrittlement which is being treated in the present work.

This document is a thesis manuscript realized in collaboration between the "Sciences des Matériaux et des Structures" (SMS) center of Mines Saint-Etienne and the foundry group Safemetal. The aim of this study is to increase our knowledge of hydrogen embrittlement (HE) for low-alloy cast steels, in particular about the interaction between hydrogen and porosity, cast steels usually having porosity defects due to different reasons, which are explained later in this document.

The industrial partner has a foundry at Feurs in France, which produces different parts of low-alloy cast steels. The hydrogen concentration is usually around 4 ppm on average. This concentration is measured at the molten state, during manufacturing, by means of Hydris sensor system. A compilation of data permitted to plot the evolution of the hydrogen concentration in the steel over a whole year as presented in Figure 1 (a). Each point represents the average hydrogen concentration for different steel grades (low-alloy steels), measured at the molten state, during a given month. It shows the effect of the local weather on the hydrogen concentration which increases in summer. Figure 1 (b) presents the hydrogen concentration as a function of the water vapor pressure, calculated using Antoine equation [2]. Figure 1 (b) indicates that the hydrogen concentration in the molten steel increases linearly with increasing the water vapor pressure in the shop atmosphere. After solidification, this hydrogen is trapped inside the final product, which can lead to HE. In fact, it has been well proved that hydrogen represents a harmful element for steels because it can lead to a serious decrease in mechanical properties, especially loss of ductility [3][4]. After the removal of the products from the molds and after heat treatments, tensile tests are usually performed on some samples in order to verify the mechanical properties. In few cases, investigation of the fracture surface using scanning electron microscope (SEM) shows a special defect known as

“fish-eyes” as illustrated in Figure 2. This defect is related to the presence of hydrogen in steel. In order to understand the formation of this defect, further investigations are made in this study. As it can be understood, it is important to explore first the effect of porosity in the hydrogen trapping and diffusion processes to be able to treat efficiently the HE problem in cast steels. Finally, it should be mentioned that there is a limited amount of data in literature about HE in cast steels.

In this work, a comparative study was made between two states of the same material: a porous state and a non-porous state in order to highlight the role of porosity in hydrogen diffusion, trapping and embrittlement. This document is divided into five chapters. The first chapter is a literature review in which the important points and the basic notions required to treat this issue are presented. Furthermore, some results from previous works are discussed in details. The second chapter is dedicated to the experimental methods that were used in this study. First, a general description of each instrument is given and then, the different experimental procedures and post-treatments are detailed. In particular, a special focus is set on the calibration procedure of the thermal desorption spectrometry (TDS) and the possible contribution of the adsorbed water to the TDS final signal. The third chapter is devoted to investigate the role of porosity in hydrogen diffusion and trapping using two main techniques: electrochemical permeation (EP) and TDS. Furthermore, from the TDS data, a method is proposed to estimate the hydrogen fugacity of the charging solution used in this work, as well as the hydrogen solubility of the material. The fourth chapter corresponds to a numerical study in which two models based on two different approaches are presented. These models are used to simulate permeation tests in porous specimens and to explore the effect of various parameters such as hydrogen fugacity and porosity fraction on the hydrogen diffusion behavior. In addition, a comparison between the experimental permeation data and the numerical results is made. In the last chapter, the focus is set on the combined effect of hydrogen and porosity on the mechanical properties of the studied steel. Tensile tests were performed on H-charged and uncharged specimens in order to underline this effect and to understand the formation of fish-eye. These findings are completed by a study of the fracture surfaces using SEM. Finally, a summary of the important findings of this work is presented. In addition, several perspectives are proposed in order to investigate further the relationship between hydrogen and porosity and to improve the numerical models.

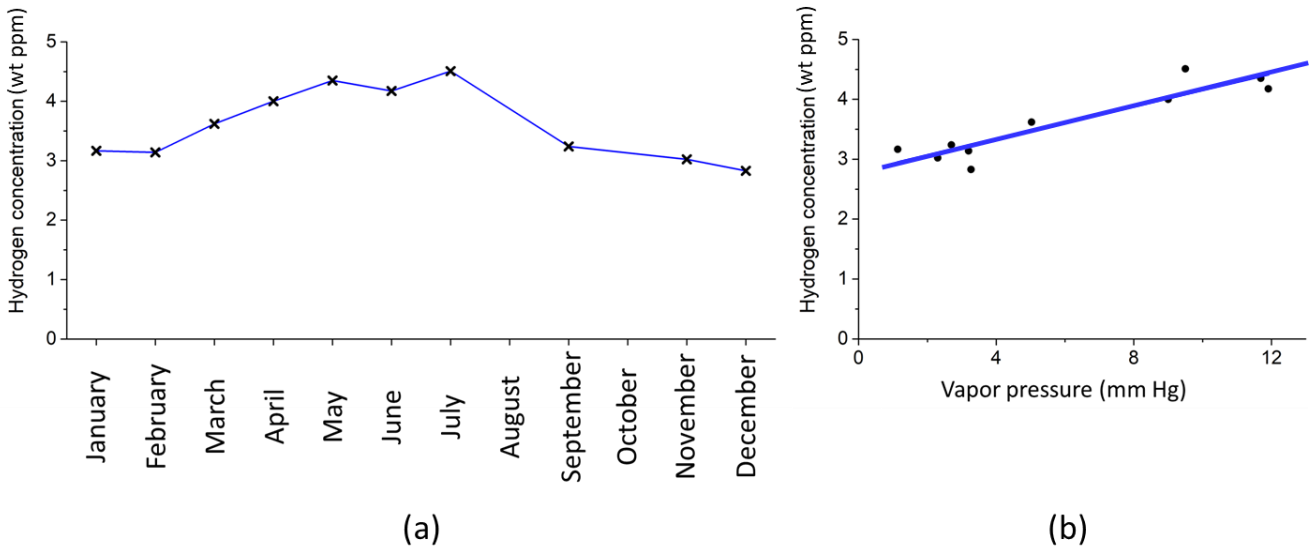

Figure 1: (a) The trend of hydrogen concentration in the molten steel for the year 2017 at SafeMetal, Feurs, France. The hydrogen concentration was measured by means of Hydris sensor system. (b) The hydrogen concentration as a function of the water vapor pressure.

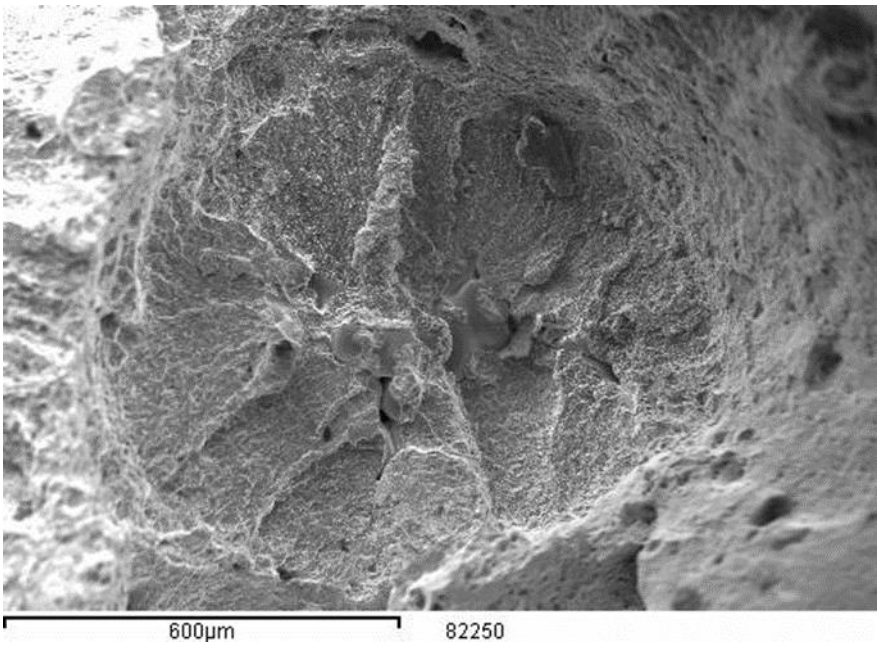

Figure 2: SEM micrograph showing the fish-eye defect, which is related to the presence of hydrogen in the material (from SafeMetal).

Chapter 1: Literature Review

I.1 Steel elaboration

I.1.1 Cast steel elaboration in arc furnaces

The most common manufacturing processes used for melting steels are electric arc furnaces and induction furnaces. The material used in this study is a low–alloy cast steel. It was elaborated in an electric arc furnace by a double-slag process, which permits the dephosphorization and the desulfurization of the steel [5]. In fact, phosphorous and sulfur can have an embrittlement effect on the steel when their concentrations exceed certain thresholds [6]. The elaboration process is presented in Figure 3. The first step consists of loading the charge (shop returns and purchased scrap) into the furnace and adding lime (calcium oxide). Then, the charge starts to melt under the high voltage applied by means of the electrodes. In fact, the metal is heated due to the current flow. Once the charge is fully melted, a first slag is created on the molten steel. At the same time, a continuous oxygen lancing is performed in order to oxidize phosphorous and reduce carbon content (decarburization) [7]. As a result, tricalcium phosphate is formed in the slag [8]. At this point, the slag has to be removed because it is very rich in phosphorous. After that, the melter checks the bath chemistry by collecting a sample from the molten steel. Based on the analysis results, alloys (ferromanganese, ferrosilicon, ferromolybdenum…) are added to adjust the chemical composition. It should be mention that oxygen lancing is stopped just before adding the alloys. Then, a second slag is added combined with aluminum ingots in order to reduce the bath and remove sulfur [8][9]. It should be mentioned also that the reduction of the bath permits to recover the alloys that were oxidized during the oxygen-lancing step (oxidation). After a second check of the melt chemistry, a new alloy addition is performed. Afterwards, the slag has to be removed before pouring the molten steel in the ladle. Once in the ladle, a last adjustment is made, if required, by using a small amount of alloys and the steel is “killed” by adding different chemical components (aluminum, titanium, zirconium, silicon…). The aim of this operation is to reduce the content of gases such as O and N (by forming non-gaseous stable phases: SiO_2, Al_2O_3, TiN, ZrN…) in order to avoid gas evolution during solidification, which can lead to the formation of gas porosity [10]. Unfortunately, this operation cannot be performed on hydrogen [11]. Therefore, other solutions have been proposed such as vacuum degassing and inert gas flushing. However, the cost and the efficiency of these operations limited their use in the steelmaking industry. Finally, the molten steel is poured into a mold.

Then, the final product is removed from the mold after solidification. Finally, heat treatments are performed on the product in order to fulfill the mechanical requirements and to reduce hydrogen concentration. This hydrogen degassing operation is known as “baking. It consists in heating steel for a certain time at a given temperature in order to obtain hydrogen desorption.

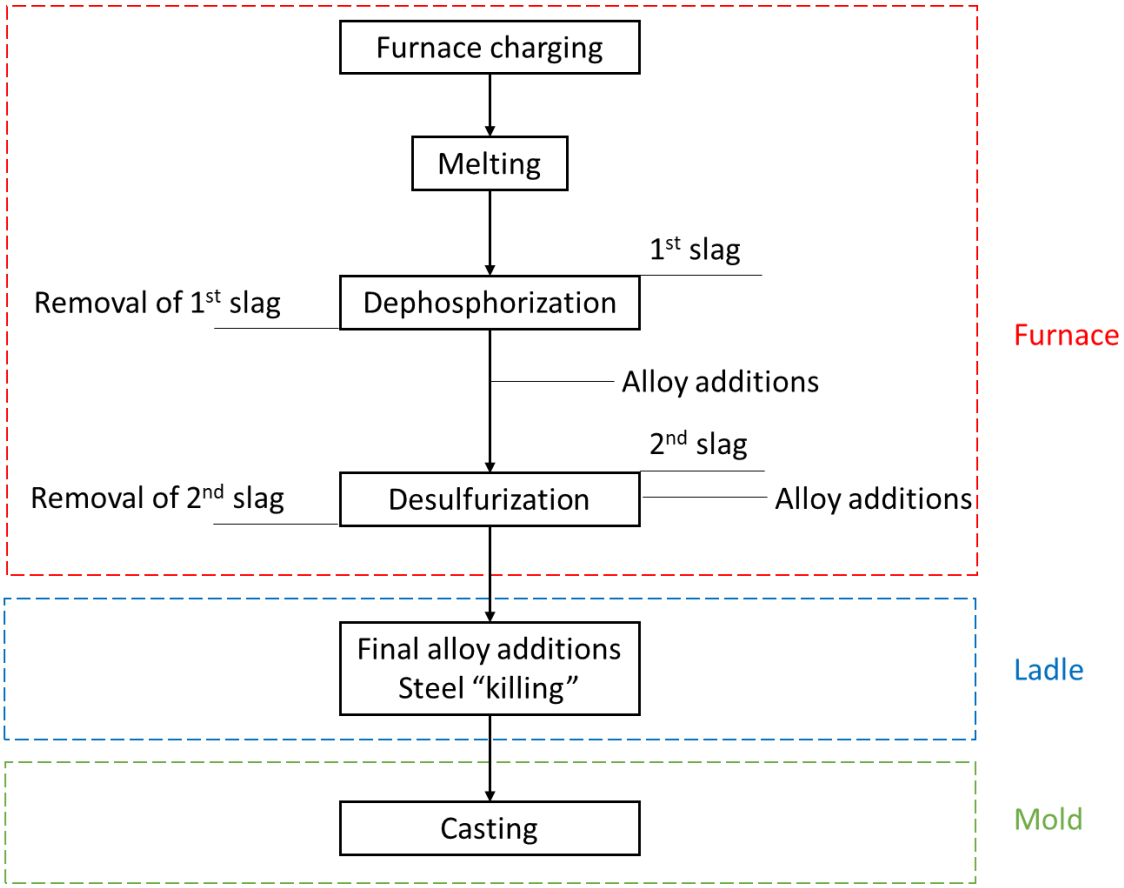

Figure 3: The operating cycle for cast steel elaboration in an electric arc furnace with a double-slag practice.

I.1.2 Porosity formation

The final product of casting has usually porosity defects with different sizes and shapes. There is mainly two major reasons for the porosity formation in castings during solidification: shrinkage and gas evolution[12][13]. Shrinkage porosity is a result of the volume reduction of steel due to the phase transformation from the liquid to the solid state. This problem can usually appear when the feeding system is inadequate and cannot provide enough liquid metal. As a result, the porosity is generally localized at the last zones to solidify [12]. The shape of this type of porosity is usually not spherical and it takes the form of the remaining space

between dendrites [14][15]. In the other hand, gas porosity is caused by the evolution of the dissolved gases during solidification. In fact, the solubility of elements such as N and H (illustrated in Figure 4) decreases significantly from the liquid to the solid state, which leads to strong partitioning between the liquid and the solid, and gas evolution in the liquid phase [12][16], with formation of porosity. It was shown that these pores are formed at the early stage of solidification or even possibly in the complete liquid state. They have spherical or ellipsoidal shapes [14][15]. Finally, it should be mentioned that the rolling and forging operations allow the elimination of these porosities [17]. For cast parts, as there is no rolling or forging operation, the porosity is not suppressed.

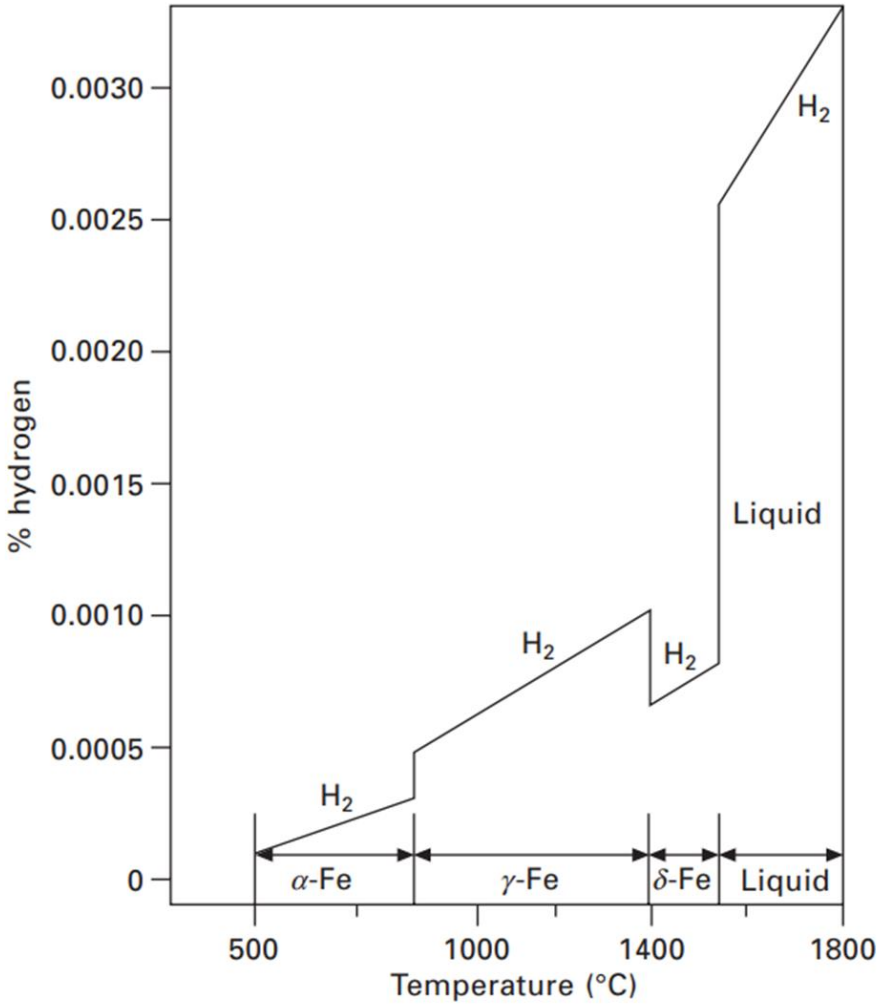

Figure 4: Hydrogen solubility in pure iron as a function of temperature. Hydrogen content is expressed in wt% [18].

I.1.3 Hydrogen sources

Hydrogen is introduced in steel either at the manufacturing process or/and in service when exposed to hydrogen-containing environments [19]. In the first case, hydrogen is absorbed mainly during melting, as hydrogen solubility is very high in the liquid state as presented earlier in Figure 4. In fact, there are numerous sources of hydrogen. The primary main source of hydrogen lies in the water vapor (humidity) in furnace atmosphere [20][21], which can be reduced into hydrogen at the molten steel surface according to the chemical reaction presented in Eq.(1). Another potential source is wet refractories [22]. Furthermore, hydrated lime and humid ferroalloys can induce hydrogen in the molten steel [23]. For this reason, a special care must be taken to the storage of lime, ferroalloys and raw materials in order to keep them dry as much as possible.

$$H_2O \rightarrow H_2 + O \quad (1)$$

I.2 Hydrogen interaction with steels

I.2.1 Chemical potential and hydrogen fugacity

The chemical potential is a thermodynamic concept that was first introduced by Gibbs in the late 1800s [24]. Its typical definition is: *"the chemical potential of a given species i is defined as the rate of increase in the Gibbs free energy of the system with respect to the increase in the number of moles of species i under constant entropy, constant volume, and constant number of moles for all species except species i"*[24]. Chemical potentials are very useful to describe phase equilibrium. For instance, when a component is under two phases (solid and gas), the equilibrium is reached when the chemical potential of the component in the solid phase is equal to that in the gaseous phase. Furthermore, it is possible to define diffusion fluxes using the gradient of chemical potentials.

The fugacity of a chemical element (usually noted *f*) is a thermodynamic function that represents its tendency to escape from a given phase to another [25][26]. It is a measure of its chemical potential [27]. For example, the relationship between the chemical potential of hydrogen (μ) and hydrogen fugacity (*f*) at a constant temperature is:

$$\mu = \mu^0 + RT.\ln\left(\frac{f}{f^0}\right) \quad (2)$$

where μ^0 is the chemical potential of hydrogen at the reference pressure (generally 1 atm) and f^0 is hydrogen fugacity at the reference pressure.

The concept of fugacity was first introduced by G.N.Lewis in the early 1900s [28]. It has the same dimension as pressure and it can be described as an adjusted pressure for real gases (at low pressures, the fugacity is equal to the pressure but it deviates at high pressures due to the non-ideal behavior of gases).

By using and combining thermodynamic relationships, San Marchi et al. provided a simple expression (Eq.(3)) that relates hydrogen fugacity to the pressure [29].

$$\ln\left(\frac{f}{P}\right) = \int_0^P \left(\frac{v}{RT} - \frac{1}{P}\right) dP \quad (3)$$

where P is the pressure, v represents the molar volume, R is the universal gas constant and T is the temperature.

I.2.2 Sieverts' law

In 1929, Adolf Sieverts presented a relationship that describes the equilibrium for the dissolution of diatomic gases in metals [30][31]. This relationship is known as Sieverts' law. For hydrogen, the expression is given in Eq.(4) [32]:

$$C = K_H\sqrt{f_{H_2}} \quad (4)$$

where C represents the concentration of atomic hydrogen dissolved in the material, K_H is the Sieverts constant (hydrogen solubility) and f_{H_2} is hydrogen fugacity. In this study, we refer to K_H as "Sieverts constant" or "hydrogen solubility" indifferently. It is important to point out that hydrogen solubility is dependent on temperature. It increases as the temperature increases as illustrated in Figure 4.

Sieverts' law can be easily demonstrated by expressing equilibrium between the respective chemical potentials of hydrogen in the solid phase (H_{Solid}) and the gaseous phase (H_2). Eq.(5) represents the chemical reaction of the dissociation H_2 into hydrogen atoms.

$$H_2 \leftrightarrow 2H_{Solid} \tag{5}$$

The first step is to calculate the chemical potentials of hydrogen in the system. In our case, the chemical potential of atomic hydrogen in the solid phase can be expressed as follows:

$$\mu_H^{Solid} = \mu_H^0 + RT \ln\left(\frac{C}{C^0}\right) \tag{6}$$

where μ_H^0 is the standard chemical potential, C is the H concentration and C^0 is the H concentration at the standard state. In the same way, it is possible to define the chemical potential of molecular hydrogen:

$$\mu_{H_2} = \mu_{H_2}^0 + RT \ln\left(\frac{f_{H_2}}{f_{H_2}^0}\right) \tag{7}$$

where $\mu_{H_2}^0$ is the standard chemical potential of molecular hydrogen, f_{H2} represents the hydrogen fugacity and $f_{H_2}^0$ is the hydrogen fugacity at the standard state. Since the chemical potential of the atomic hydrogen at the gaseous phase is equal to the half of the chemical potential of the molecular hydrogen ($\mu_H^{gas} = \frac{1}{2}\mu_{H_2}$), we can express the chemical potential of atomic hydrogen inside the gas as:

$$\mu_H^{gas} = \frac{1}{2}\mu_{H_2}^0 + RT \ln\sqrt{\frac{f_{H_2}}{f_{H_2}^0}} \tag{8}$$

At equilibrium, the chemical potential of hydrogen in the solid is equal to the chemical potential of hydrogen in the gas, which leads us to the following expression:

$$\mu_H^0 + RT \ln\left(\frac{C}{C^0}\right) = \frac{1}{2}\mu_{H_2}^0 + RT \ln\sqrt{\frac{f_{H_2}}{f_{H_2}^0}} \tag{9}$$

Thus, the equilibrium hydrogen concentration in the solid phase can be expressed as:

$$C = \frac{C^0}{\sqrt{f^0_{H_2}}} \times \exp\left(\frac{\frac{1}{2}\mu^0_{H_2} - \mu^0_H}{RT}\right) \times \sqrt{f_{H_2}} \qquad (10)$$

which is the same expression as the one presented at the beginning in Eq.(4), with $K_H = \frac{C^0}{\sqrt{f^0_{H_2}}} \times \exp\left(\frac{\frac{1}{2}\mu^0_{H_2} - \mu^0_H}{RT}\right)$ which represents hydrogen solubility. As it can be seen from the expression, this solubility is dependent on the temperature. It increases with increasing the temperature. Figure 5 shows the evolution of hydrogen solubility as a function of the temperature. Hydrogen solubility is higher in the austenitic phase (ϒ) than in the ferritic phase (α) but this difference decreases at high temperature. Furthermore, hydrogen solubility in the 16MND5 steel is higher than in pure iron because this is an "apparent" solubility, which takes into account hydrogen trapping in the different microstructural defects.

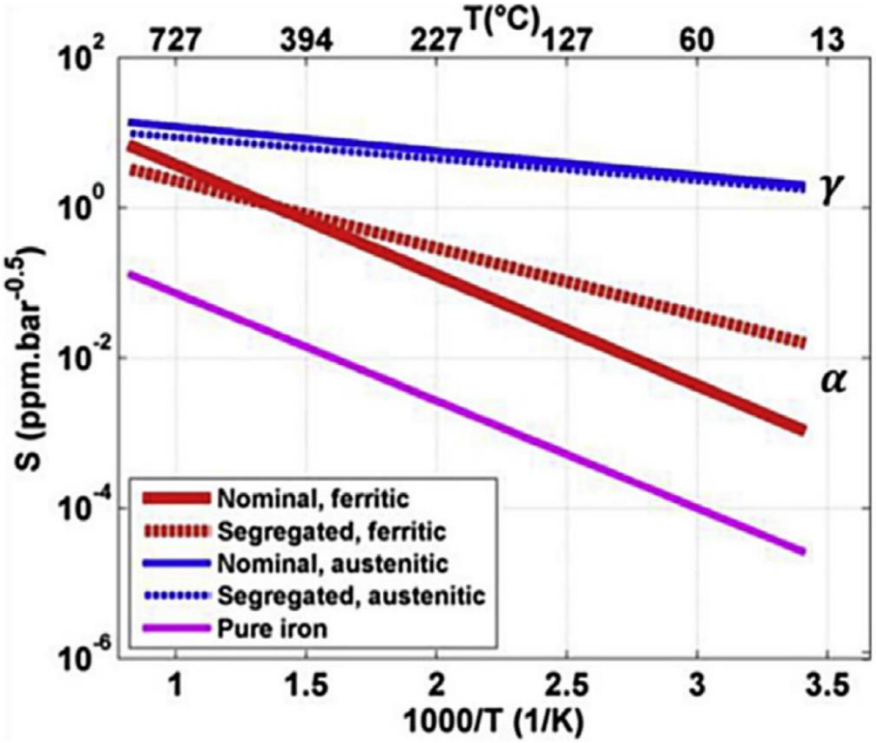

Figure 5: The evolution of hydrogen solubility as a function of temperature for the ferritic phase (α) and the austenitic phase (ϒ) of a 16MND5 steel. The dashed lines correspond to an adjusted composition representing segregated bands. For more details see reference [33].

I.2.3 Hydrogen diffusion and trapping

Hydrogen atom has the smallest atomic radius which facilitates its diffusion in solid solution. In body-centered cubic metals, hydrogen occupies tetrahedral sites whereas it occupies octahedral sites in the face-centered cubic metals [34][35]. In general, hydrogen diffusion from one interstitial site to another, also called lattice diffusion, is governed by Fick's laws [36]:

$$J = -\mathrm{D}\nabla\mathrm{C} \tag{11}$$

$$\frac{\partial \mathrm{C}}{\partial \mathrm{t}} = \nabla(\mathrm{D}\nabla\mathrm{C}) \tag{12}$$

where J is the hydrogen flux, D is the diffusion coefficient, C is the hydrogen concentration and t represents the time. However, in reality, hydrogen diffusivity is highly affected by microstructural defects such as dislocations, voids, grain boundaries and precipitates [34] known as hydrogen traps. Figure 6 presents a compilation of the hydrogen diffusion coefficients taken from several works [4][33][35]. It shows that the diffusion coefficient increases with increasing the temperature. In addition, it shows that the diffusion coefficient varies from one microstructure to another, which can be explained by the interaction of hydrogen with the different phases and defects in the microstructure. In fact, these sites are called traps because their potential well is deeper than that of the interstitial sites and as a result, hydrogen atom stays in the trap for a longer time than in the interstitial site [35]. At a given temperature, these traps can be categorized in two groups based on the energy required to escape the trap: reversible traps and irreversible traps as illustrated in Figure 7. However, the limit between the two types of traps is arbitrary [35]. For instance, Lee suggested that the energy limit is situated at 26.4 kJ/mol [37] whereas, it was mentioned in other works [38][39][40] that this limit is about 60 kJ/mol. It can also be mentioned from the data presented in Figure 6 that hydrogen diffusion is much faster in the ferrite (BCC) than in the austenitic (FCC), although the difference tends to decrease at high temperature.

(a)

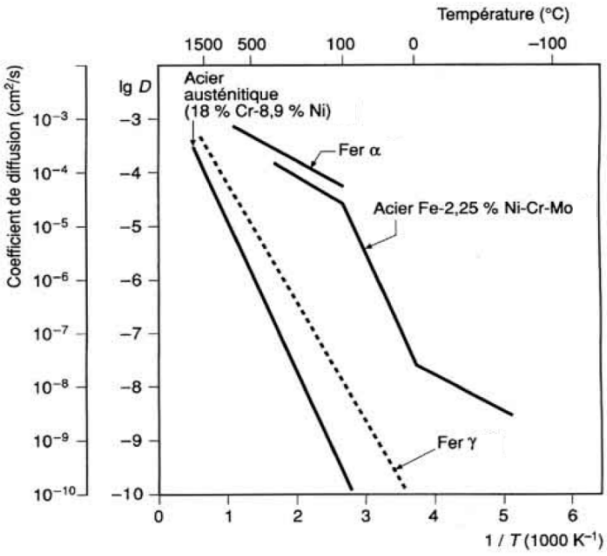

(b)

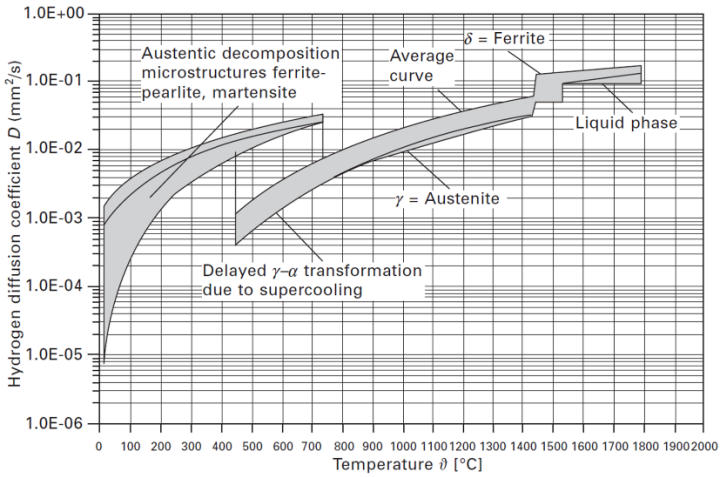

(c)

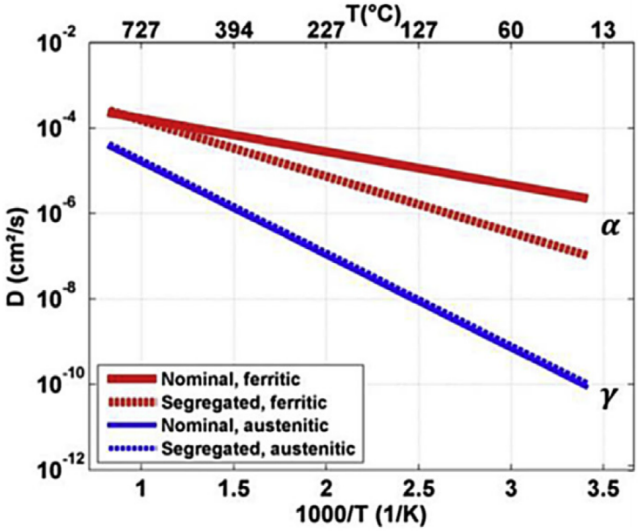

Figure 6: Compilation of the evolution of hydrogen diffusion coefficients as a function of the temperature. (a) for iron and steel [4]. (b) for carbon steels and low-alloy steels [35]. Note that D is presented in mm²/s. (c) for 16MND5 steel. The dashed lines correspond to an adjusted composition representing segregated bands. For more details see reference [33].

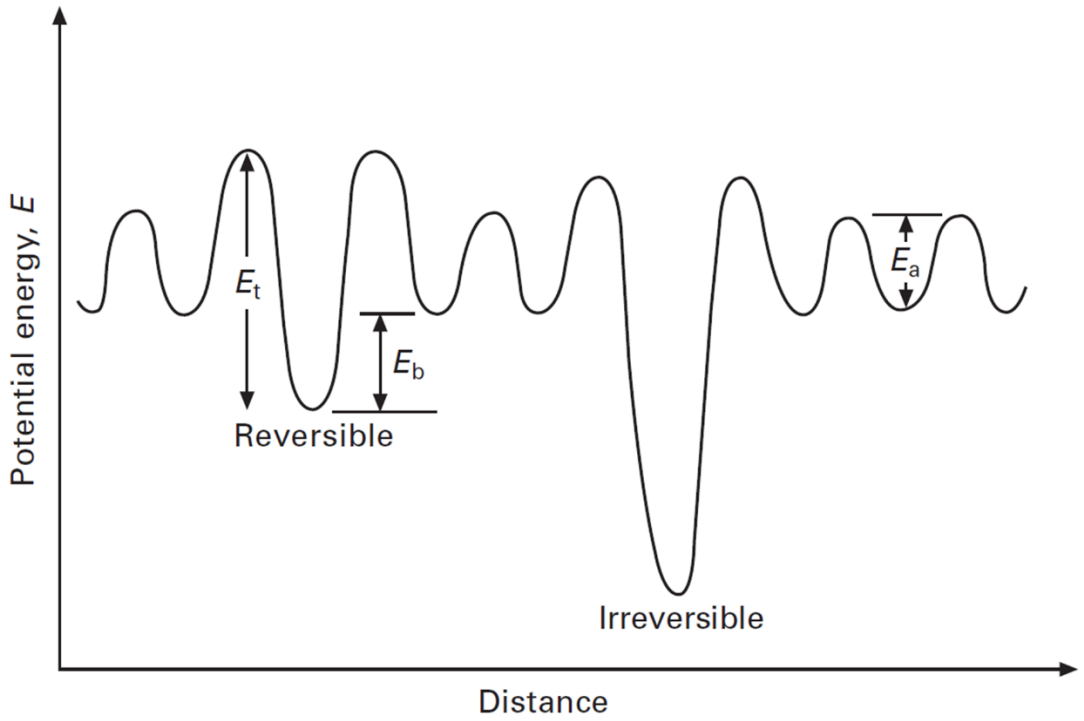

Figure 7: A schematic illustration of the potential energy for the lattice diffusion with activation energy E_a, and trapping site with binding energy E_b and activation energy E_t. The activation energy depends on the nature of the trap. The figure is extracted from Turnbull work [35].

In ferritic-pearlitic steels, some studies [41-45] have demonstrated that the interfaces in pearlite act as trapping sites for hydrogen. For instance, Chan et al. [41] have studied hydrogen trapping by performing a series of experiments on Fe-C alloys in which they increased the pearlite-ferrite interface density by varying the carbon content in the alloy. They have shown that hydrogen diffusivity decreases with increasing the pearlite-ferrite interface density. Moreover, it was reported, in other studies [42][43], that the interfaces in pearlite correspond to irreversible hydrogen trapping sites at room temperature and that the trapping energy is about 65 kJ/mol.

I.2.4 Modelling of hydrogen diffusion and trapping

As mentioned earlier, hydrogen can be trapped by the defects present in the steel and as a result, the diffusion behavior is affected. Through the years, several theoretical models were developed to describe hydrogen diffusion and trapping. For instance, McNabb and Foster developed a general mathematical model that took into consideration the trapping effect in the hydrogen diffusion process [46][47]. This model describes the hydrogen diffusion behavior in steel where trap sites are uniformly distributed. It is important to point out that no

assumption was made about the nature of the traps. They succeeded to incorporate this trapping effect by integrating a trapping term in the second Fick's law. Then, Oriani reformulated their work and provided simpler equations that are based on the assumption of local equilibrium between lattice and trapped hydrogen [48]. He has shown that the hydrogen apparent diffusion coefficient depends on the trap sites density and the trapping energy. Later, Turnbull et al. established a model that is not only able to treat the case of high trapping occupancy but also gives the possibility to treat irreversible traps as well as reversible traps [49]. In fact, it seems that Leblond and Dubois [50] were the first ones to treat this issue (combination of reversible and irreversible traps) but they only treated the case of low trapping occupancy. More recent works [51-56] have been made in the last decade in order to simulate the hydrogen diffusion process with the presence of traps. These studies have permitted to increase our knowledge of the effect of different traps on hydrogen behavior. In the present work, the focus was set on one specific trap, which is the porosity (i.e. voids). This porosity can store molecular hydrogen as explained by the hydrogen pressure theory proposed by Zappfe [57]. It assumes that atomic hydrogen H diffuses through the material and recombines as molecular hydrogen H_2 inside the cavities. Several studies [58-64] were carried out on this specific topic. In his work [64], J.G Sezgin introduced a refined equation of state (EOS) for gas hydrogen based on the National Institute of Standards and Technology (NIST) database. This EOS describes the real behavior of hydrogen better than the other EOS do. This point is discussed in details in the next section. In this study, this EOS was used in two different numerical models.

I.2.5 Hydrogen and porosity

I.2.5.1 State of hydrogen trapped in porosity

In this work, the main objective is to study the interaction between hydrogen and porosity. Little work has been done in existing literature on the effect of porosities on hydrogen diffusion and trapping. These few studies [37][65-70] mentioned that voids act as trapping sites for hydrogen. For instance, Choo [70] worked with pure iron samples that have different densities (obtained by cold drawing) and he showed that, after hydrogen charging, the amount of hydrogen trapped in voids increases with increasing the voids volume fraction as illustrated in Figure 8. He also determined a trapping energy of 35.2 kJ/mol for the microvoids based on these measurements [70]. Some studies mentioned that voids are reversible traps

for hydrogen [68][69] while others considered them as irreversible traps [37][65-67]. Lee et al. studied hydrogen trapping in porosities in pure iron and in nickel. For pure iron [37], they developed a mathematical model for hydrogen retrapping which was verified using experimental data. The specimens used in their study were cold-drawn in order to create microvoids. Then, these specimens were thermally charged with hydrogen followed by a rapid quench to room temperature. After quenching, the specimens were analyzed by the gas chromatography technique to determine the amount of trapped hydrogen. The microvoids trapping energy was estimated to be 40 kJ/mol. Furthermore, they mentioned that this energy was equal to 56 kJ/mol for an AISI 4340 steel [66]. Finally, they concluded that microvoids act as irreversible traps for hydrogen. The same authors investigated the effect of voids on hydrogen trapping in nickel [65] and they came to the same conclusion that voids are strong trapping sites for hydrogen. In addition, Padhy [67] carried out a literature review on the different aspects of hydrogen in steel weldments and he classified the voids as irreversible traps too. As can be understood from this literature review, the reversible or irreversible nature of voids is not entirely clear. For this reason, this point is discussed in details in this study for the case of cast steels. Finally, it should be noted that no information about the size of these microvoids was given in the references mentioned above.

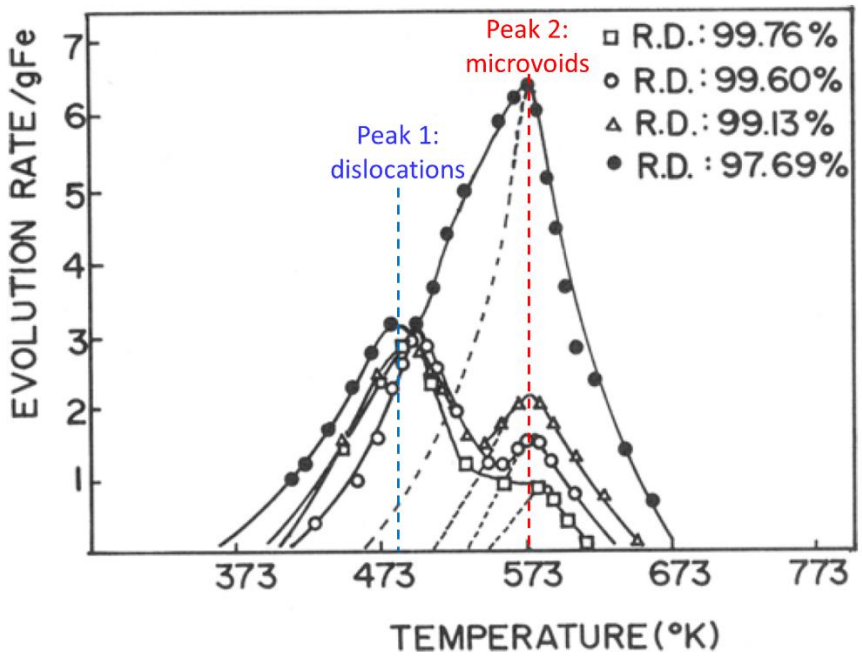

Figure 8: TDS curves for pure iron samples charged with hydrogen. The samples have different relative density (R.D) achieved by cold drawing. Heating rate: 2.6 K/min. The peak height corresponding to microvoids (peak 2) increases with increasing the volume fraction of voids [70].

Another question can be raised about the physical state of hydrogen in the voids: it can be either in the atomic state, adsorbed on the internal surfaces of the voids or inside the voids as H_2 molecules, i.e. gaseous. From literature, the exact state of hydrogen in voids is not completely clear. It depends on various parameters such as the pressure inside the voids, the volume fraction of porosity, the temperature… Figure 9 presents the ratio of hydrogen between the adsorbed and the gaseous form as a function of the void radius for different pressures (1, 100 and 10 000 atmospheres). These results are based on theoretical calculations obtained by Wong [71] in iron. It shows that the amount of adsorbed hydrogen increases with decreasing the void size for a given pressure. In the case of 1 atmosphere and a void radius of 10^{-6} cm, the majority of hydrogen is under the atomic form. However, for high pressures the amount of adsorbed hydrogen tends to be negligible compared to the amount of molecular hydrogen. For our case, this ratio will be discussed later based on experimental and theoretical calculations.

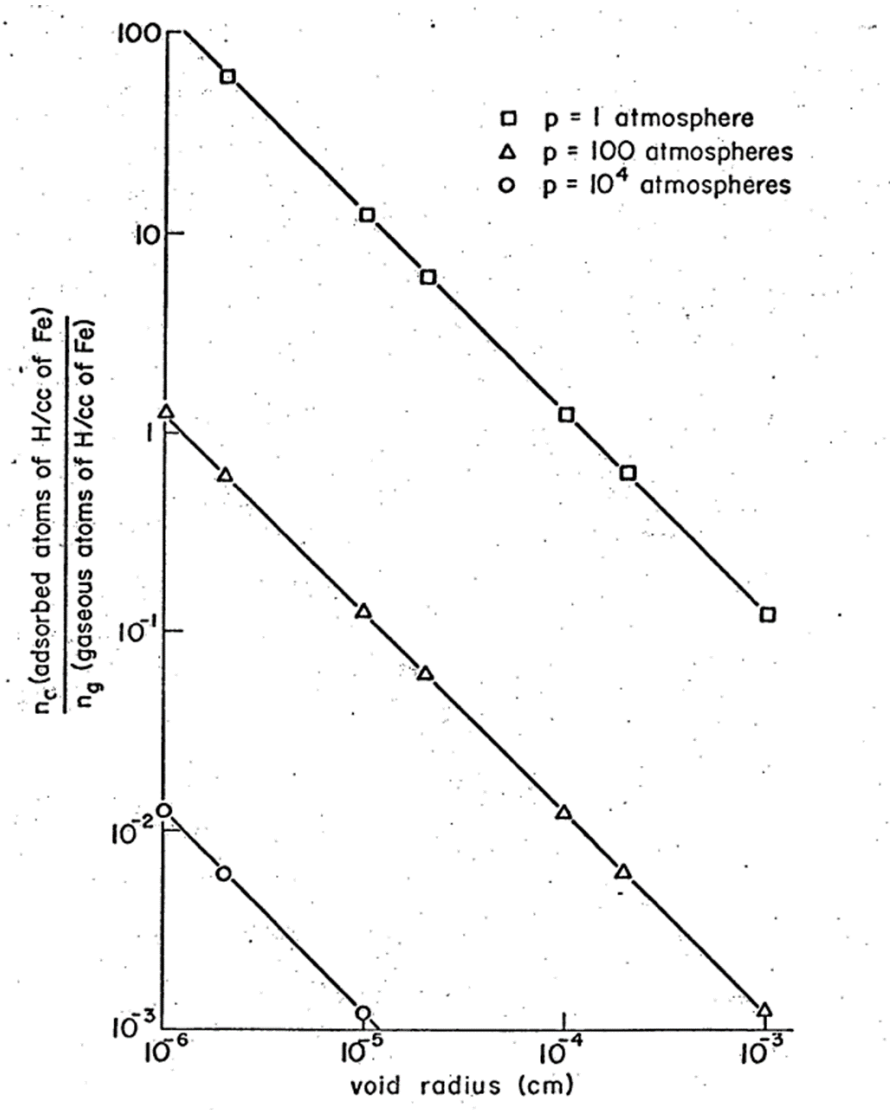

Figure 9: The ratio of adsorbed to gaseous hydrogen with respect to the void radius for three different pressures: 1, 100 and 10 000 atmospheres [71].

I.2.5.2 Equation of state of gaseous hydrogen

An equation of state (EOS) is an equation that relates the state variables of a system in order to give a description of its thermodynamic state. There are many EOS and each one is only valid under certain conditions [72].

Under low pressures, gases behave according to the ideal gas law presented in the following equation:

$$Pv = RT \tag{13}$$

where P is the pressure, v represents the molar volume, n is the number of moles, R is the universal gas constant and T is the temperature. However, at high pressures, the gas behavior deviates from the ideal gas law. At high pressures, the volume occupied by the molecules (co-volume) becomes important compared to the total volume and as a result it has to be considered in calculations. In addition, at low temperatures, the kinetic energy of gas molecules decreases significantly, which promotes the interaction between the molecules. For hydrogen gas, this latter effect can be neglected for temperatures above 200 K [64]. There is in fact a number of different EOS that can be applied to hydrogen: Van-der-Waals, Hemmes, Able-Noble… and each EOS is only valid in a certain range of temperature and pressure. For instance, Eq.(14) corresponds to the Able-Noble EOS, which is equivalent to Van-der-Waals EOS at room temperature.

$$\mathrm{Pv} = \mathrm{RT} + \mathrm{Pb} \tag{14}$$

where, b represents the co-volume (1.584×10^{-5} $m^3.mol^{-1}$) [29]. In this study, we needed a consistent EOS that gives an accurate description of hydrogen especially at high pressures. Therefore, a new EOS, which has been developed by Sezgin [64][73], was used (see Eq.(15)). In his work, Sezgin proposed a new EOS based on Abel-Noble model and on thermodynamic data from the National Institute of Standards and Technology (NIST), which relates hydrogen density to pressure. This new EOS is referred to as “NIST” in this study. The model is valid for temperatures above 200 K and pressures up to 2000 MPa.

$$\mathrm{Pv} = \mathrm{RT} + \mathrm{Pb}^0 - 1.955 \times 10^{-15} \times \mathrm{P}^2 \tag{15}$$

where b^0 is a constant (1.4598×10^{-5} $m^3.mol^{-1}$). For a given EOS, the relationship between hydrogen pressure and hydrogen fugacity can be obtained from Eq.(3). Figure 10 [64] presents the relationship between hydrogen fugacity and hydrogen pressure at room temperature plotted using the EOS of Able-Noble, Van-der-Waals and the NIST data. As it can be seen, the same results were found until 300 MPa then, for a given fugacity, the NIST pressure is higher. In fact, this difference is due to the pressure dependency of the co-volume, which is included in the NIST data whereas the co-volume was a constant for the two other EOS. These findings motivated J.G Sezgin to develop the new EOS in order to overcome this problem.

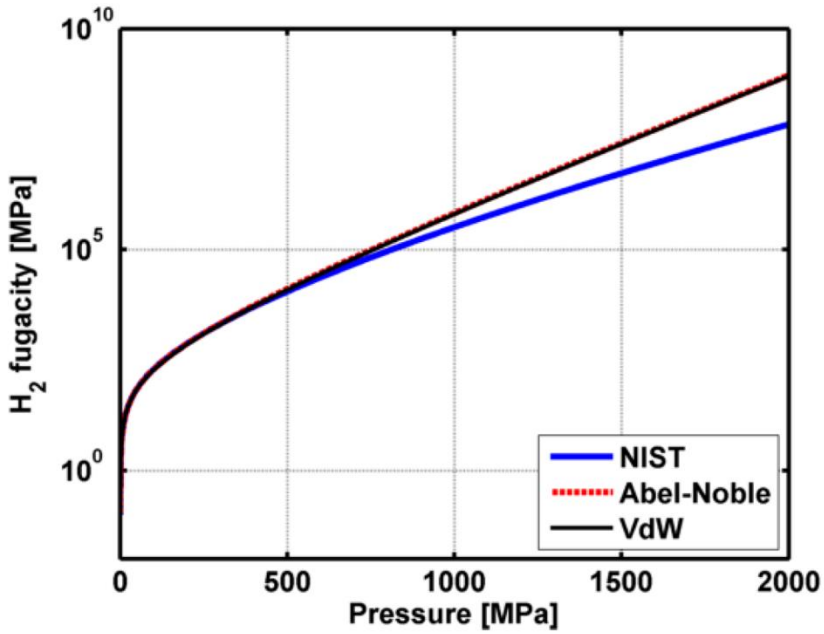

Figure 10: Hydrogen fugacity as a function of the pressure at room temperature for three different EOS. The blue curve corresponds to the EOS developed by J.G Sezgin. The red and black curves correspond to the Abel-Noble and Van-der-Waals model, respectively [64]. Note that the fugacity values are presented on a logarithmic scale.

I.2.5.3 Distribution of hydrogen in a steel containing porosities

At room temperature

In order to have a better understanding of the effect of the EOS on the hydrogen behavior, a comparison between hydrogen as a real gas (by using the NIST EOS) and as an ideal gas is made. We consider a case where a steel sample has a porosity fraction equals to 0.1% and the hydrogen solubility is equal to 0.18 mol/(m^3×$bar^{0.5}$). The solubility value used here is obtained from the experimental data that are presented in chapter 3. In addition, we assume that hydrogen is only distributed between the bulk and the porosity and that there is no exchange with the environment. Therefore, the total hydrogen concentration in the sample is the sum of hydrogen in the porosity and in the bulk as described in Eq.(16).

$$C_{Total} = C_B + C_P \quad (16)$$

where C_{Total} is the total hydrogen concentration in the sample, C_B represents the hydrogen concentration in the bulk and C_P is the hydrogen concentration in the porosity. The calculation results of hydrogen distribution are presented in Figure 11. These results are obtained by the resolution of a system of equations composed of the following equations {(3), (4), (13), (15)

and (16)}. Furthermore, all calculations were performed at room temperature. It should be mentioned that the temperature has a significant effect on the hydrogen distribution between the bulk and the porosity. A detailed description of this effect is provided in in the next section. Figure 11 (a) shows the evolution of the equilibrium hydrogen pressure in the pores as a function of the total hydrogen concentration inside the sample for the two EOS. The pressure in the two cases increases similarly with increasing the total amount of hydrogen until 1 wt ppm. Then, the hydrogen pressure calculated using the real gas EOS becomes higher than that of the ideal gas until 60 ppm. This increase is a consequence of the co-volume, which becomes more significant at high pressures. Above 60 wt ppm, the pressure calculated using the real gas EOS becomes smaller than that of the ideal gas. Actually, the pressure increase becomes slower and slower for the real gas compared to the ideal gas. This is a direct result of the fugacity, which tends to increase significantly the hydrogen concentration in the bulk (Sieverts' law in Eq.(4)) especially when the pressure is high. Figure 11 (b) represents the distribution of hydrogen between the bulk (C_B) and the porosity (C_P) as function of the total hydrogen concentration. In both cases, C_P is lower than C_B for C_{Total} below 0.2 wt ppm. Then, above this concentration, C_P becomes higher than C_B for the ideal gas. However, for the real gas, C_P is higher than C_B for C_{Total} from 0.2 wt ppm until approximately 10 wt ppm and then above 10 wt ppm, C_B becomes higher again. This is due to the fugacity effect as explained previously, which tends to increase significantly the amount of hydrogen in the bulk when the pressure becomes high. As it can be seen, the two EOS give the same distribution of concentrations between the bulk and the porosity until 1 wt ppm. Then, for C_{Total} above 1 wt ppm, C_B of the real gas becomes higher than C_B of the ideal gas and C_P of the real gas becomes lower than C_P of the ideal gas. This is a result of the co-volume and the fugacity. Another interesting result of the real gas behavior can be seen in the same figure. For instance, for a C_{Total} equals to 20 wt ppm, the pressure is about 371 MPa and 645 MPa for the ideal gas and the real gas respectively which represents an increase of 74%. However, C_P is equal to 18.4 wt ppm and 7.8 wt ppm for the ideal gas and the real gas, respectively. This represents a 58% decrease in the hydrogen concentration in the porosity. To sum up, the pressure of hydrogen inside the porosity was higher for the real gas compared to the ideal gas even though the hydrogen amount in the porosity was lower in the case of the real gas. Finally, it is important to recall that these results of course vary with the input parameters used in these calculations such as the porosity fraction and temperature.

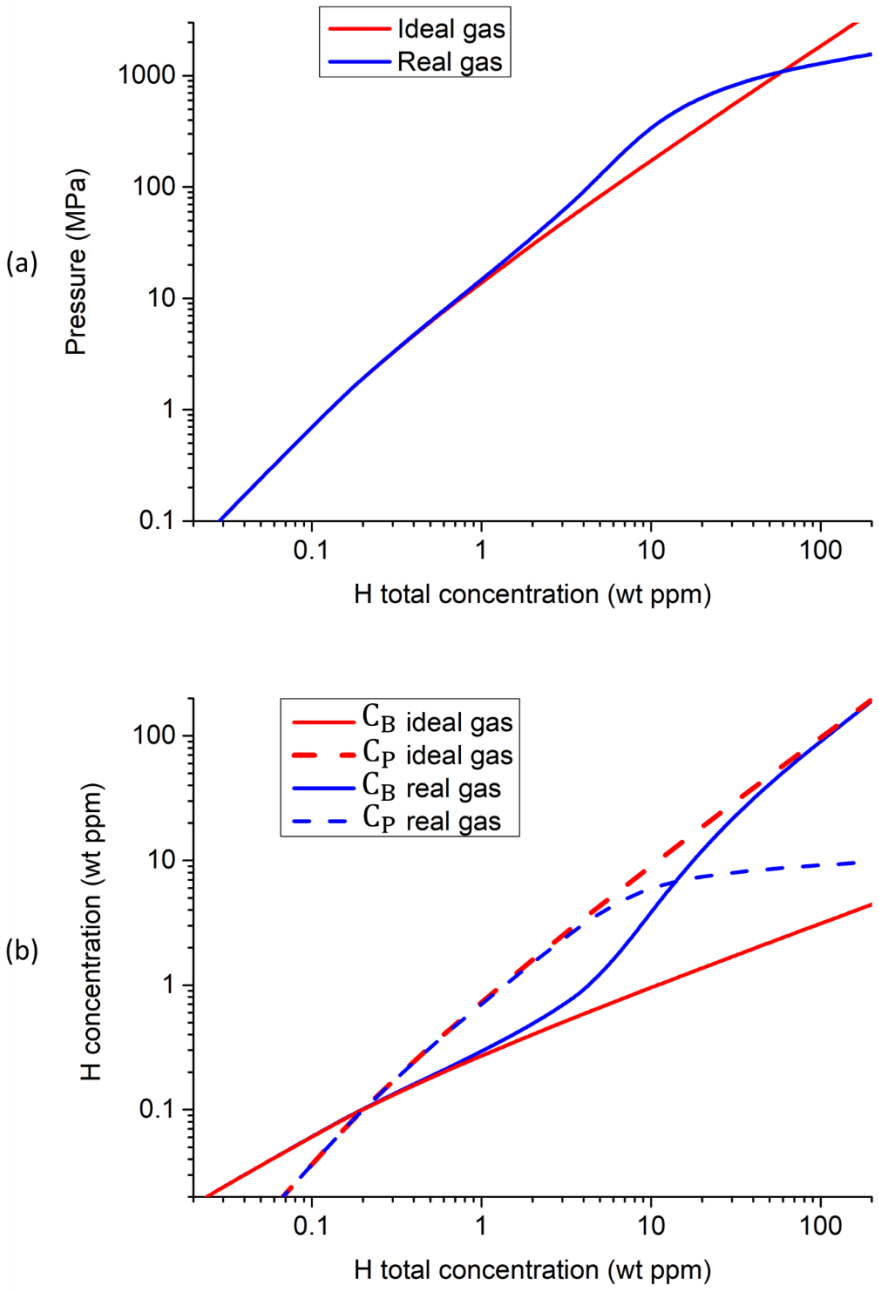

Figure 11: Comparison between the ideal gas EOS and the real gas EOS. (a) The pressure evolution in porosities as a function of the total hydrogen concentration. (b) Hydrogen distribution between the bulk and the porosity as a function of the total concentration. Porosity fraction: 0.1%. Solubility coefficient: 0.18 mol/(m^3×$bar^{0.5}$).

At high temperatures

In this section, the effect of temperature on the amount of hydrogen in the porosity and in the bulk is discussed. As mentioned in the first chapter, hydrogen solubility increases with

temperature (see Figure 4). Thus, for the same total hydrogen concentration, the amount of hydrogen in the porosity and in the bulk vary with temperature. Figure 12 represents the results of calculations based on the values of hydrogen solubility taken from the work of Sezgin [63] (presented in Figure 5). The calculations were performed considering a steel sample containing 1 wt ppm of total hydrogen and a porosity fraction of 0.1%. The results are obtained by the resolution of a system of equations composed of Eq.(3), (4), (15) and (16). It indicates that, for the same total hydrogen concentration, the amount of hydrogen in the bulk increases with increasing the temperature, which leads automatically to decrease the amount of hydrogen in the porosity. This is a direct consequence of the increase of hydrogen solubility with temperature. As it can be seen, at low temperatures the majority of hydrogen is located in the porosity while, at high temperatures, it is the opposite. As a consequence, it is expected that the trapping of hydrogen by porosities becomes negligible above a certain temperature.

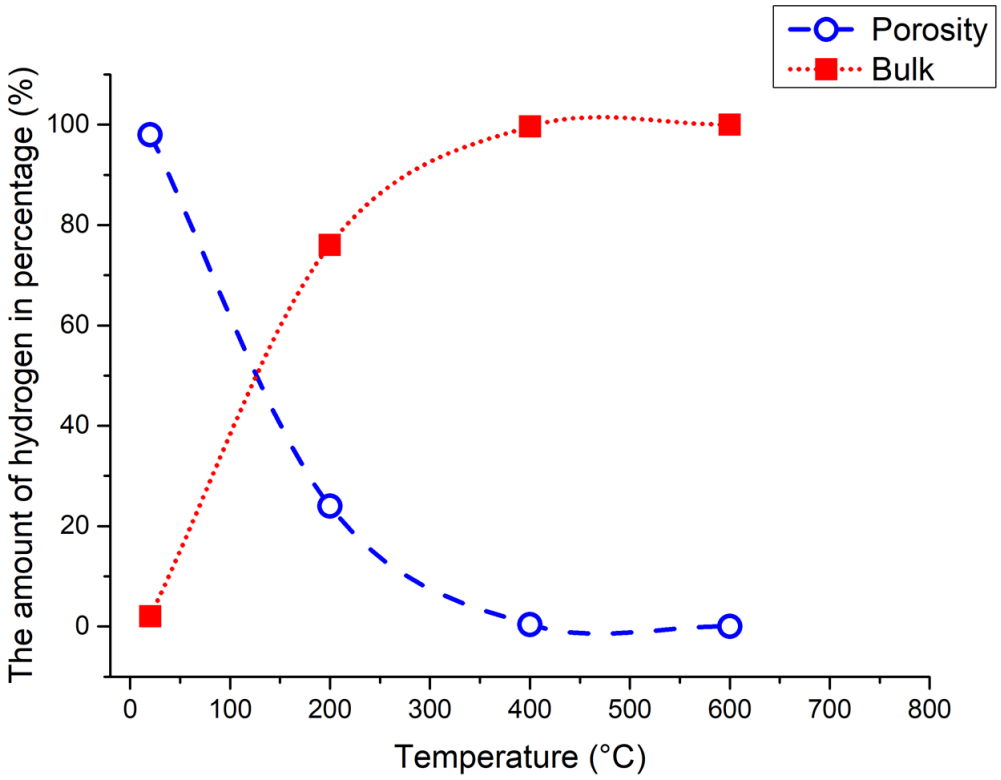

Figure 12: Hydrogen distribution between the porosity and the bulk as a function of the temperature. Hydrogen solubility values used in these calculations are extracted from Sezgin work [63]. Total hydrogen concentration: 1wt ppm. Porosity volume fraction: 0.1%.

I.2.5.4 Hydrogen diffusion coefficient in steel containing porosity

Chew has proposed a model for hydrogen diffusion in a steel containing voids [69][74]. The model was developed first for ideal gas and then he extended his work for high hydrogen pressures in the voids (up to 1000 atm) and for temperatures below 200°C. The model was built on the assumption of a constant local equilibrium between the molecular hydrogen trapped in the voids and the surrounding hydrogen in the bulk. Finally, under the assumption of ideal gas, Chew obtained the following expression of the apparent diffusion coefficient at low hydrogen pressures in the voids:

$$D_{app} = \frac{D_L}{\left(1 + \frac{2X_P}{RTK_H}\sqrt{P}\right)} \quad (17)$$

where D_{app} is the apparent hydrogen diffusion coefficient, D_L is the lattice hydrogen diffusion coefficient, X_P represents the volume fraction of porosity, R is the universal gas constant, T is the temperature, K_H corresponds to the hydrogen solubility and P is the hydrogen pressure in the voids. As it can seen from Eq.(17), D_{app} decreases with increasing the porosity fraction and the pressure. In the other hand, the D_{app} increases with increasing the solubility coefficient. In order to give a visual description of these effects, the curves of D_{app} as a function of these three parameters are presented in Figure 13. The lattice diffusion coefficient (D_L) used in these calculations is equal to 7×10^{-9} m²/s which represents the hydrogen diffusion coefficient in pure iron determined at 298 K [75]. Figure 13 (a) corresponds to the influence of the porosity fraction on the apparent diffusion coefficient for three different values of solubility. The same behavior was found in the three cases. The D_{app} decreases with increasing the porosity fraction, which means that the trapping effect of voids increases with increasing the porosity fraction. In the other hand, the D_{app} tends to D_L, when the porosity fraction becomes low. For high values of the porosity fraction, the slope is equal to one, which means that D_{app} varies linearly with X_P. Figure 13 (b) shows the effect of hydrogen pressure on the D_{app}. As it can be seen, the D_{app} decreases with increasing the pressure. In addition, D_{app} tends also to D_L when the pressure is very low. For high values of pressures, the slope is equal to ½, which means that D_{app} varies as $\sqrt{P}$. Finally, Figure 13 (c) presents the influence of the solubility coefficient on D_{app}. D_{app} increases with increasing the solubility. This can be interpreted as reducing the trapping effect of the voids because when the solubility is high, the voids tends to trap a

smaller fraction of hydrogen. For low values of solubility, the slope is equal to one, which means that D_{app} varies linearly with K_H. As it can be understood, the D_{app} expression is a useful tool to interpret hydrogen diffusion under different configurations. In addition, it could be used in the diffusion equation to simulate permeation tests for example. However, several limitations have to be considered:

- In a permeation experiment, the hydrogen pressure in the voids is space-and-time-dependent, so D_{app} is not a constant. Numerical solving of the diffusion equation is thus needed.
- Eq.(17) is valid only for ideal gas, i.e. in a limited range of pressure.

The modelling approaches developed in this work are not based on the concept of the apparent diffusion coefficient, as shown later.

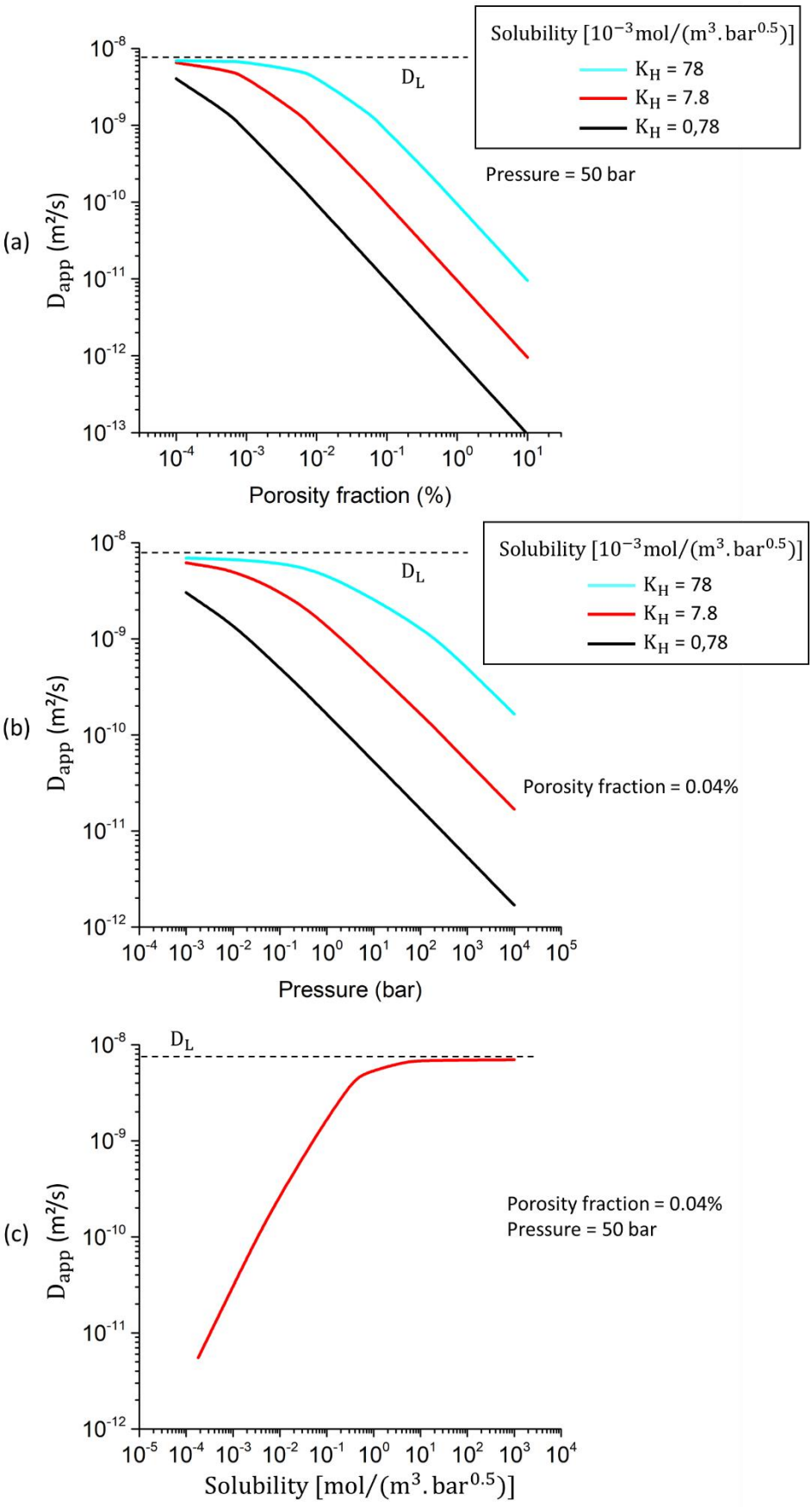

Figure 13: The apparent hydrogen diffusion coefficient proposed by Chew calculated using Eq.(17) as a function of (a) the porosity fraction (b) the hydrogen pressure and (c) the solubility coefficient.

I.3 Hydrogen embrittlement

I.3.1 Hydrogen embrittlement mechanisms

In the literature, several mechanisms have been proposed in order to explain HE in metals. In general, it is possible to classify these mechanisms in three main groups: hydride-induced embrittlement, Hydrogen Enhanced DEcohesion mechanism (HEDE) and plasticity localization failure (Hydrogen Enhanced Local Plasticity: HELP, and Adsorption-Induced Dislocation Emission: AIDE).

- The hydride formation associated to an oversaturation of hydrogen can lead to the degradation and the failure of metals [76][77][78]. This mechanism was first introduced by Westlake [76] who argued that the cracking can be initiated near the crack tips by the formation of hydride precipitations. He indicated that the formation of hydrides could be enhanced by the hydrostatic stress in the crack tip region.
- The HEDE mechanism was first discussed by Troiano [79] and then was improved by Oriani [80][81]. This mechanism is based on the following assumption: the dissolved hydrogen lowers the cohesion forces between the atoms of the alloy. In this case, the interatomic bond breaks when the local stress exceeds the hydrogen-lowered forces. It was reported that the HEDE mechanism can occur along cleavage planes, interfaces and grain boundaries [81].
- The third group is composed of two mechanisms based on the hydrogen-dislocation interactions. The HELP mechanism was first proposed by Beachem [82][83] who suggested that the presence of a sufficient amount of dissolved hydrogen facilitates the mobility of dislocations. This leads to the increase of the local plastic deformation and as a result reduces the local stress needed to initiate cracks. The other mechanism (AIDE) is based on the decrease of the energy required to create dislocations at the crack surfaces caused by the adsorbed hydrogen [84][85]. Once the cracks are created, the dislocations move away from the crack tip. In this mechanism, the cracking is a result of a combination of a localized plastic deformation due to the dislocations and the nucleation and growth of micro-voids at the crack tip.

I.3.2 Hydrogen embrittlement in ferritic-pearlitic steels

Several researchers have studied the HE of low-alloy steels. In particular, the HE of ferritic-pearlitic steels [41][86-90]. In terms of mechanical behavior, it was found that hydrogen did not affect greatly the yield strength and the ultimate tensile strength of the steel, while it influenced significantly its ductility (total elongation) [41][86][87] as illustrated in Figure 14. However, Zhang et al. [91] found that there is a difference in the yield strength between uncharged and H-charged specimens. They mentioned that the yield strength could decrease with increasing hydrogen concentration. Moro et al.[86] have also performed tensile tests on a X80 steel under hydrogen gaseous charging. Their results indicated that the HE increases with increasing the hydrogen pressure (until 10 MPa) and with decreasing the strain rate.

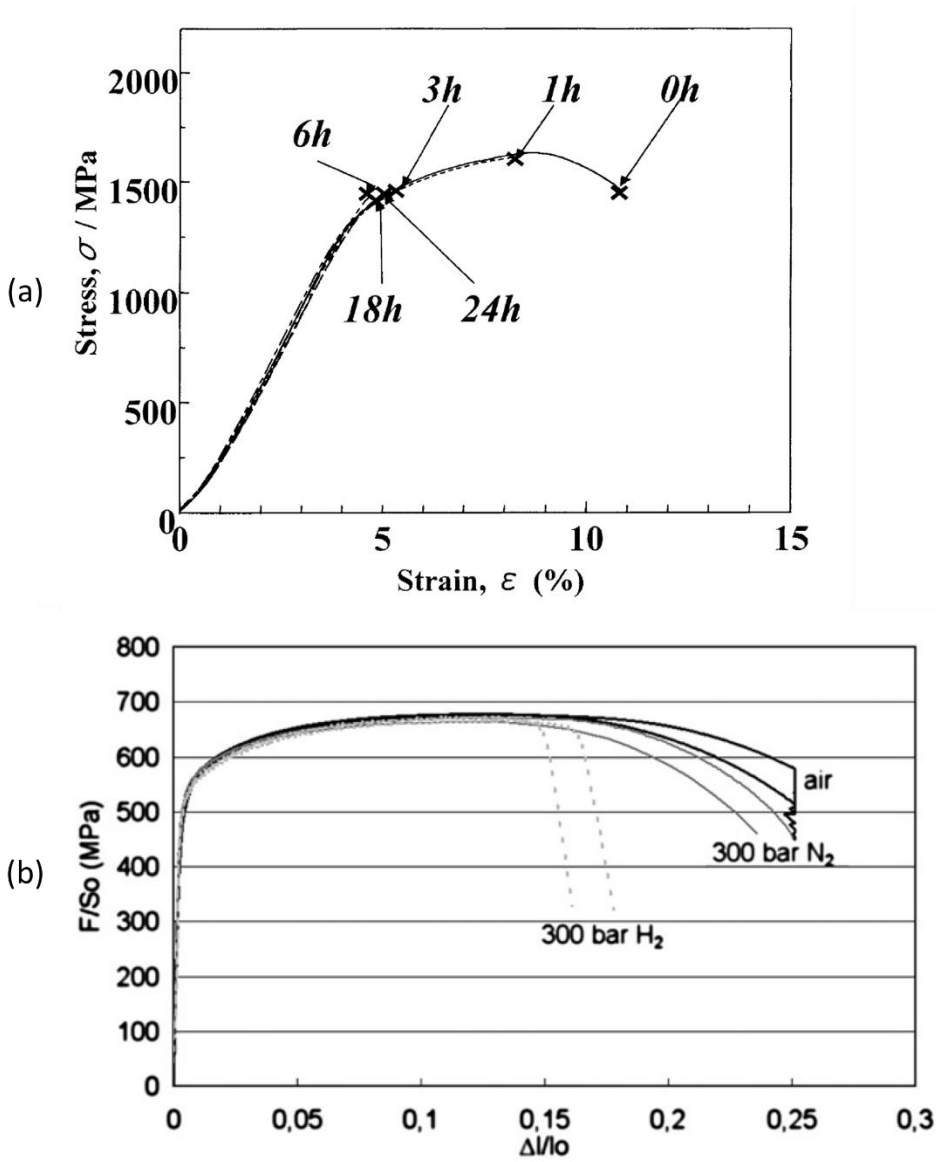

Figure 14: Stress-strain curves for uncharged and H-charged specimens. (a) High-strength steel charged in 20 wt% NH_4SCN solution heated at 50°C for different times (strain rate = 5×10^{-7} s^{-1}) [42]. (b) X80 steel charged by applying a 300 bar hydrogen pressure (strain rate = 5×10^{-5} s^{-1}) [86].

It was reported, especially in the case of ferrite-pearlite banded structures, that the ferrite-pearlite interfaces represent HE crack nucleation sites [86][88-90] because hydrogen can accumulate at the interfaces and promotes the weakening of cohesion (HEDE) of the steel along these interfaces [86][89]. In these works, the study of the fracture surfaces of the hydrogen charged specimens showed, in general, the presence of a mix of ductile and brittle areas. However, no occurrence of brittle areas was found on the fracture surface of hydrogen charged tensile specimens in several works [42][92-94]. For instance, T.Neeraj et al. [93][94] conducted tensile tests on hydrogen pre-charged specimens of a ferritic-pearlitic steel (X65) and found a general reduction in the total elongation by 30%. They reported that the fracture

surface did not show any brittle area, as illustrated in Figure 15, and that there was evidence for hydrogen-enhanced plastic flow localization. Consequently, it can be understood that the fracture mode does not depend only on the presence of hydrogen inside the specimens.

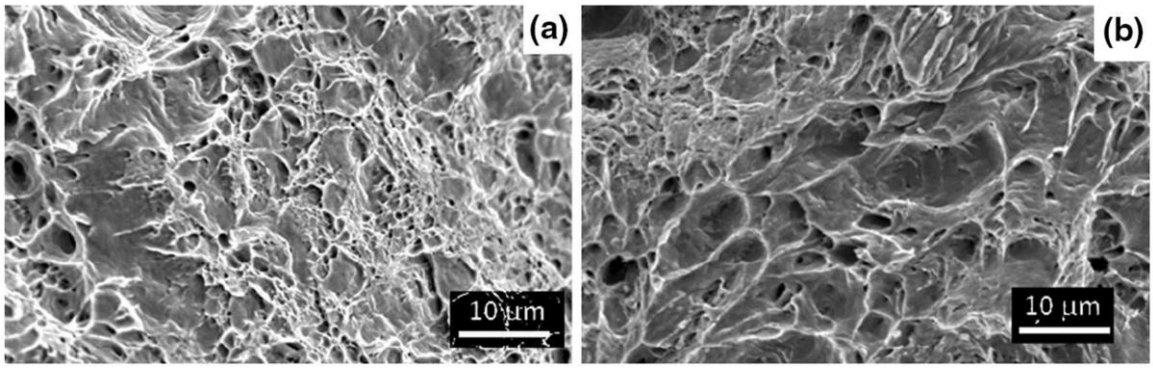

Figure 15: Fracture surfaces of the X65 steel after tensile testing showing a ductile failure. (a) Uncharged specimen. (b) H-charged specimen (total hydrogen content = 4 wt ppm) [93].

I.3.3 Fish eyes

As mentioned earlier in the introduction, the industrial partner encountered in some cases fish-eyes defects on the fracture surfaces of tensile test specimens. These fish-eyes present a round shape brittle area centered on a defect as presented in Figure 16, which is usually a non-metallic inclusion or a void. Several studies [95-101] were performed in order to highlight the nature and the formation mechanism of fish-eyes. For instance, Möser and Schmidt [95] assumed that the fish-eye defect is a result of the high pressure of hydrogen inside a void or at the matrix-inclusion interface as explained by the pressure theory presented by Zapffe et al. [57]. They mentioned that the fish-eye formation could occur with or without external load. In the other hand, Cialone and Asaro found that the internal pressure mechanism was unlikely to occur in their case because of the low pressure inside the voids. Instead, they explained the fish-eye formation by the loss of cohesion due to hydrogen during tensile testing [96]. Vibrans [97] also found the same defect with the same features as the authors mentioned previously (Möser and Schmidt). He produced hydrogen-induced fractures by performing tensile tests on hydrogen pre-charged specimens. The fracture surfaces showed the presence of fish-eyes which are centered on inclusions. Finally, he suggested that the brittleness of the material does not depend only on its strength but also on the additions of alloying elements and voids because they modify hydrogen solubility and diffusivity. Sojka et al. [98] studied the formation conditions of fish-eyes in two different low-alloy steels (A508.3 and 18MND5). They

performed tensile tests on hydrogen charged specimens (the hydrogen concentration was between 4.8 and 7.2 wt ppm). They concluded that a high hydrogen concentration and large non-metallic inclusions are necessary to form fish-eyes. In addition, they mentioned that fish-eyes grow predominantly in the necking region. Merson et al. [100][101] found fish-eyes on the fracture surfaces of tensile test specimens after hydrogen charging (2 wt ppm) for a low-carbon steel. The same morphology was observed as the previous authors. It appears also that the fish-eyes are centered on the non-metallic inclusions.

(a)

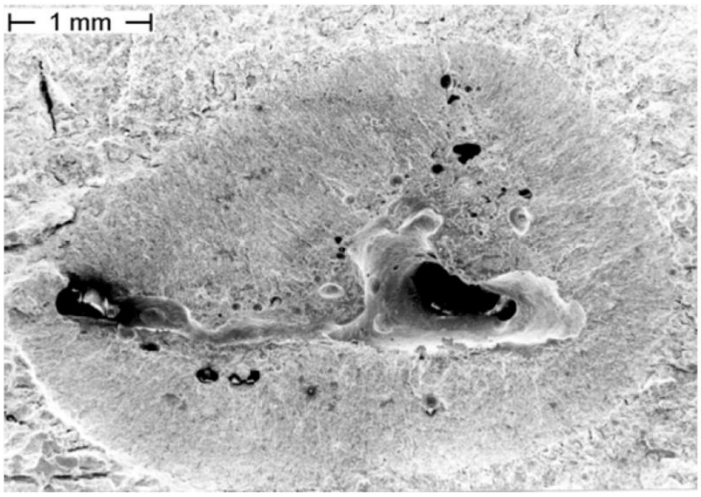

(b)

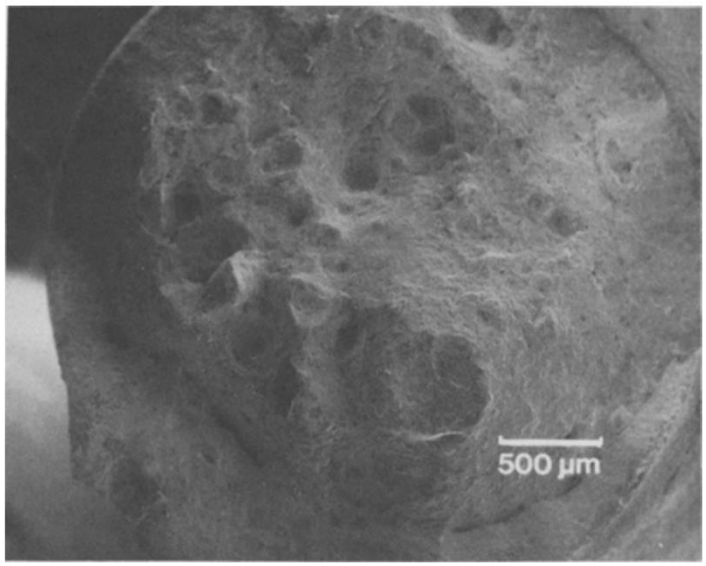

(c)

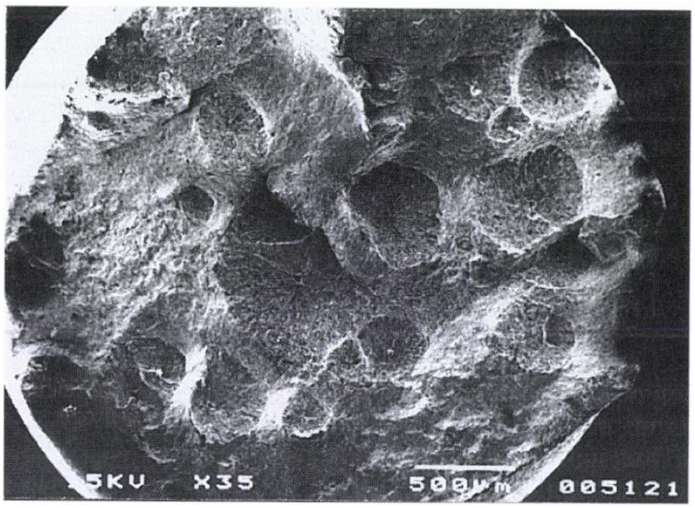

Figure 16: A compilation of fish-eye defects obtained from different studies. (a) Möser and Schmidt [95]. (b) Cialone and Asaro [102]. (c) Sojka et al. [98].

Chapter 2: Material and Methods

II.1 Material and heat treatments

The raw material provided for this study was an ingot of low-alloy cast steel G20MN5 (presented in Figure 17). The alloy had been elaborated in an electric arc furnace and then the molten steel was poured in a sand mold. After slowly cooling to room temperature, the ingot was removed from the mold. The dimensions were approximately 300x120x100 mm. The chemical composition of this steel is provided in Table 1. Finally, it is worth noting that no heat treatments were performed on this material until this point.

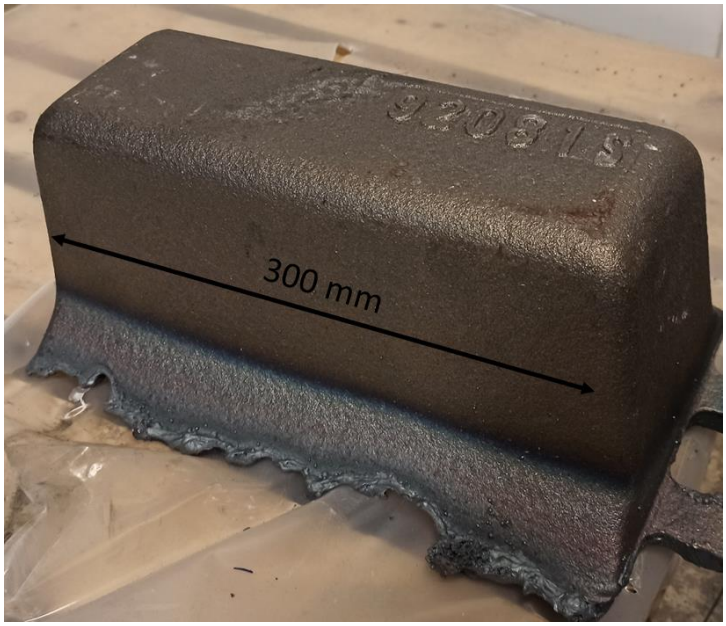

Figure 17: The low alloy cast-steel ingot used for this study.

Table 1: Chemical composition of the material used in this study.

Element	C	Mn	Si	S	P	Ni	Cr	Mo	V
% mass	0.187	1.120	0.410	0.009	0.008	0.230	0.150	0.020	0.001

The ingot was sectioned along the length axis into two halves and then, each half was cut into parts of 250x52x45 mm. The bars from the first half were forged at 1000°C and their final dimensions were 300x26x26 mm. The forging ratio was around 3.5. This ratio is defined as the initial cross section divided by the cross section after forging. The aim of the forging step was to close cavities in order to get a non-porous material. The other bars were machined to obtain the same dimensions as the forged bars. In this way, the heat transfer behavior during subsequent heat treatments and quenching will be the same for the raw bars and the forged

bars. Finally, in an attempt to have the same microstructure, all bars were normalized at 880°C for 60 minutes and then air cooled to room temperature. Forging and heat treatment parameters are shown in Figure 18.

In the following sections, for convenience purposes, the term ‘’forged’’ is used for the material “forged and normalized”, and the term “cast” is used for the “cast and normalized” material.

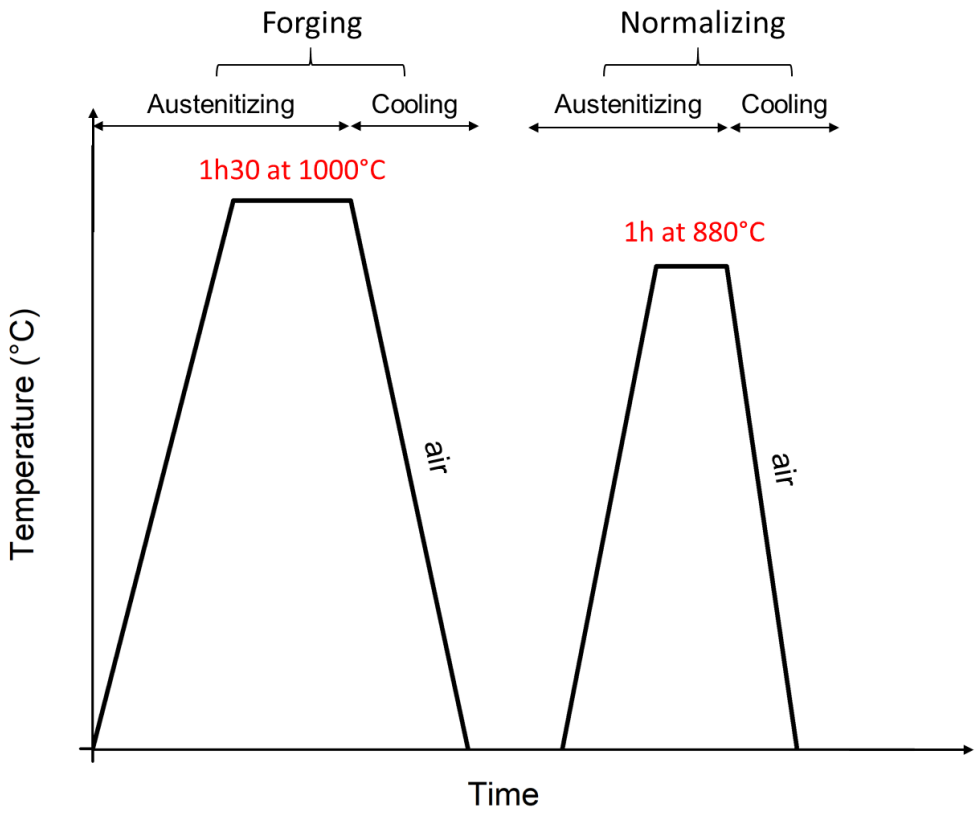

Figure 18: Forging and normalizing treatments. The normalizing treatment is the same for the forged and the cast bars in order to obtain the same microstructure.

II.2 Hydrostatic weighing technique

Hydrostatic weighing is a technique that has been widely used for the determination of the density of different solid materials [103]. This technique is based on Archimedes’ principle. Figure 19 shows a schematic representation of the equipment.

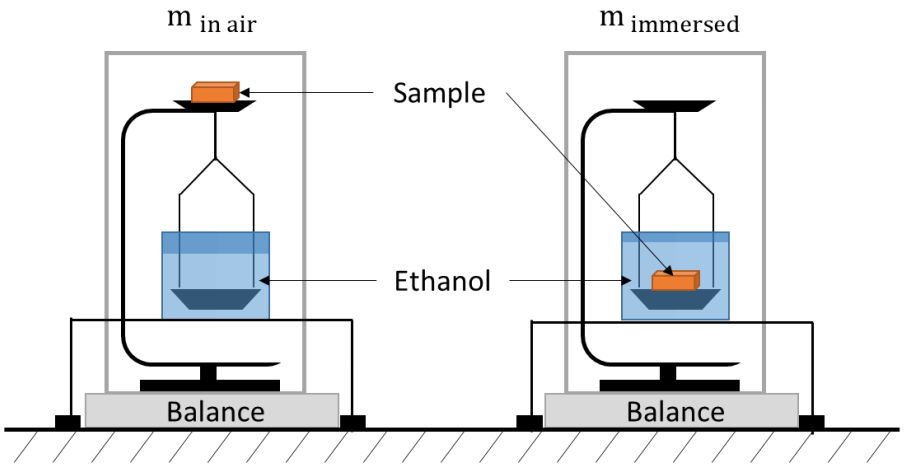

Figure 19: Schematic setup of the hydrostatic weighing equipment.

The procedure consists in weighing a sample in air and then in a liquid of well-known density. The weight in air represents the true weight of the sample and the weight in the liquid permits to determine the volume of the sample V_{sample} (see Eq.(18)). Then, the sample density can be obtained from $\rho_{sample} = m_{in\ air} / V_{sample}$.

$$V_{sample} = \frac{m_{in\ air} - m_{immersed}}{\rho_{liquid}} \tag{18}$$

where V_{sample} is the volume of the sample, $m_{in\ air}$ is the weight of the sample measured in air, $m_{immersed}$ represents the weight of the sample after immersion and ρ_{liquid} is the density of the liquid.

In our study, the density of the forged sample is considered as the real density of the material because the forged material does not contain voids in contrast of the cast sample. Therefore, the volume fraction of porosity X_p in a cast sample can be determined from:

$$X_p = \frac{V_P}{V_{cast}} = \frac{V_{cast} - \frac{m_{cast}}{\rho_{forged}}}{V_{cast}} \tag{19}$$

where V_P is the volume of porosity, V_{cast} is the volume of the cast sample (calculated using Eq.(18)), m_{cast} is the weight of the cast sample measured in air and ρ_{forged} is the density of the forged material.

In this study, the liquid used was pure ethanol (99.5%) and the resolution of the digital balance was 0.1 mg. Each measurement was performed 3 times. The temperature of the ethanol was determined in order to obtain its true density. Considering the average mass of the specimens used in this study (4 g), the measurement uncertainty on the porosity fraction was estimated at ± 0.02%.

II.3 X-ray tomography

X-ray tomography is a non-destructive technique used to reveal the internal features of materials. It is widely used in several fields especially in medical and material sciences [104]. It is based on the absorption of X-rays that pass through a specimen. The specimen is rotated during the scanning in order to collect 2-D images at different angles. Using a reconstruction algorithm, this technique permits to generate a virtual volume of the scanned object, which allows to obtain certain useful characteristics (porosity, defects size, distribution, identification of different phases such as corrosion layers [105]…). However, like all techniques, X-ray tomography has its own limitations. Actually, samples that have high density or large thickness are difficult to scan, because of high X-ray absorption. Furthermore, some features like voids can be overlooked due to their small size compared to the scanning resolution. In addition, it is recommended to perform the scan on cylindrical samples (rather than samples with rectangular cross sections) in order to establish a uniform transmissivity of X-rays across all projections and avoid severe change in contrast [106][107][108].

In this study, a Nanotom Phoenix X-ray tomograph was used in order to verify the presence of cavities in the cast samples and the absence of cavities in the forged samples. The samples were small cylinders of 2 mm in diameter and 6 mm in height as presented in Figure 20. The X-ray source was a tungsten target. Incident X-rays having an energy of 60 keV were obtained by applying a 160 kV voltage and a 30 µA current. A 0.5 mm copper filter resulting in a pixel size of 1.5 µm was used. 1600 projections were recorded for each scan and the collected data were then analyzed and visualized using Avizo software.

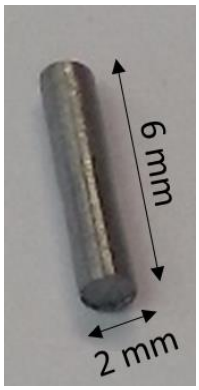

Figure 20: Photograph of the sample used in the X-ray tomography analysis.

In order to remove artefacts and especially to reduce the “salt and pepper” noise, a pre-treatment was performed on the collected data by applying different filters. The first step was to set a threshold, based on a scan of a cast sample, which permits to identify the voids, which appear as dark particles. Figure 21 (a) shows a cross section from the cast sample as captured with X-ray tomography. The voids (dark grey areas) are easily recognizable due to the difference in contrast. Figure 21 (b) presents the same cross-section but after applying the chosen threshold. As it can be seen, the voids are now colored in blue. Then, the same threshold was applied on a forged sample as shown in Figure 21 (c). The forged sample is considered as a material without porosities because of the forging operation at high temperature as explained earlier. Therefore, the tomography of the forged sample should not show any porosities. However, a closer look showed that several particles with an equivalent diameter inferior to 4 µm were detected as illustrated in Figure 21 (d). We assume that these particles do not correspond to voids but are most probably a result of the salt and pepper noise.

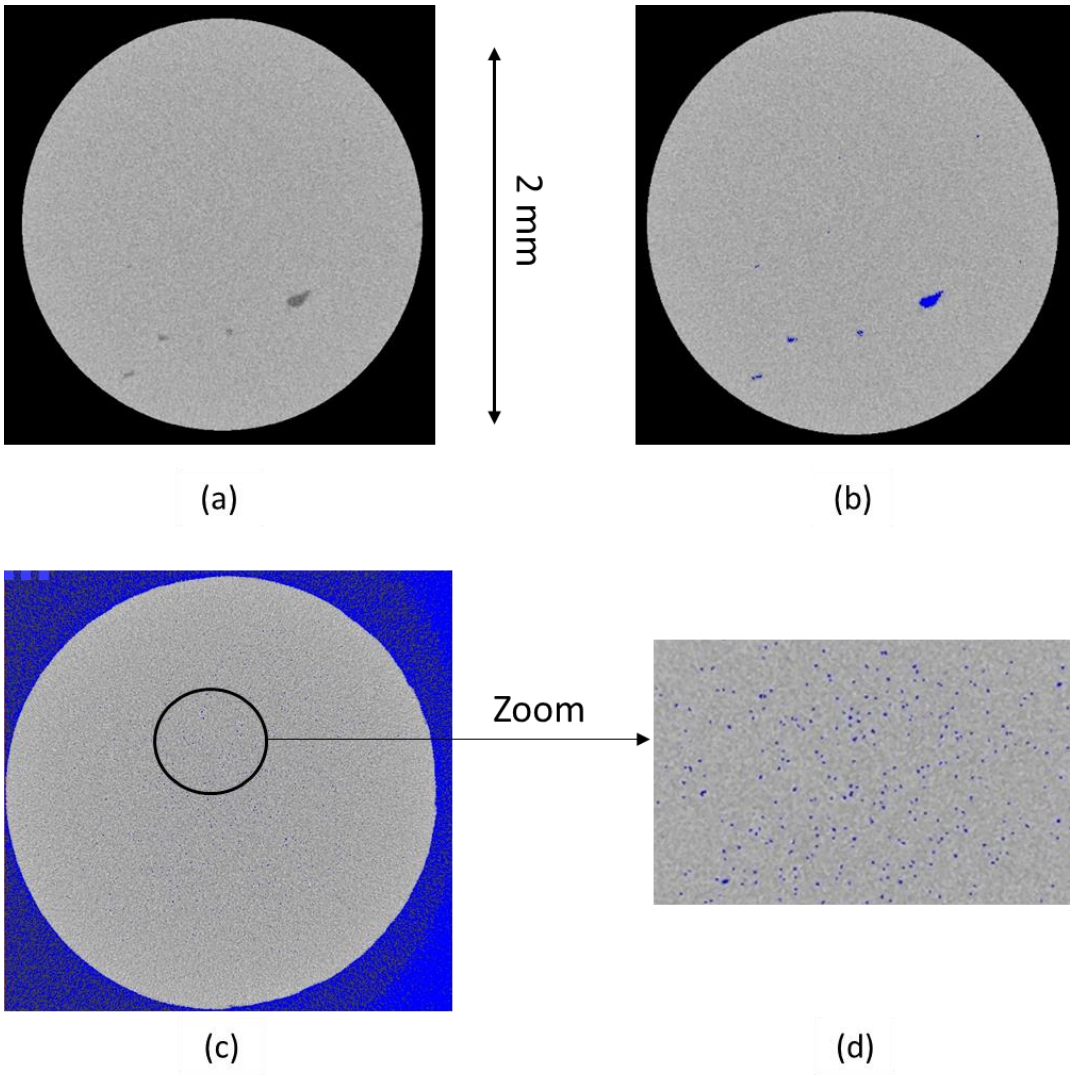

Figure 21: Cross sectional view obtained by X-ray tomography of (a) a cast sample as captured showing the presence of voids and (b) the same cast sample after the thresholding. The blue area represent the detected voids by Avizo software. (c) A cross section of a forged sample after applying the same threshold as for the cast sample. (d) A zoom into an area of the forged cross section showing the presence of small particles (blue dots) because of the salt and pepper noise.

In order to confirm this assumption, another material was investigated using X-ray tomography. It was a 25CrMo4 commercial steel (0.22% C, 0.6%Mn,0.9% Cr,0.3% Mo) elaborated and forged industrially. Figure 22 (a) shows the result of the X-ray scanning of the 25CrMo4 material. Once again, particles with an equivalent diameter inferior to 4 µm were found in this material in which no void should exist.

It is clear then that these particles are not voids but are a result of the noise. To resolve this problem, different filters were applied on the 25CrMo4 sample until most of the particles were removed. The first filter was a median filter used for smoothing noisy images. It is very

effective on salt and pepper noise as described in Avizo user's guide [109]. Unfortunately, this filter was not enough to reduce completely the noise effect, thus a further filtering was performed. A second filter called "Remove small spots" was used which consists in removing particles that are composed of a number of pixels inferior to a certain value defined by the user. In our case, the value was set at 12 pixels because it permitted to reduce significantly the number of detected particles (6000 particles for the as captured data and only three particles after applying the two filters). Figure 22 (b) shows the scanning result after the filtering process for the 25CrMo4 sample.

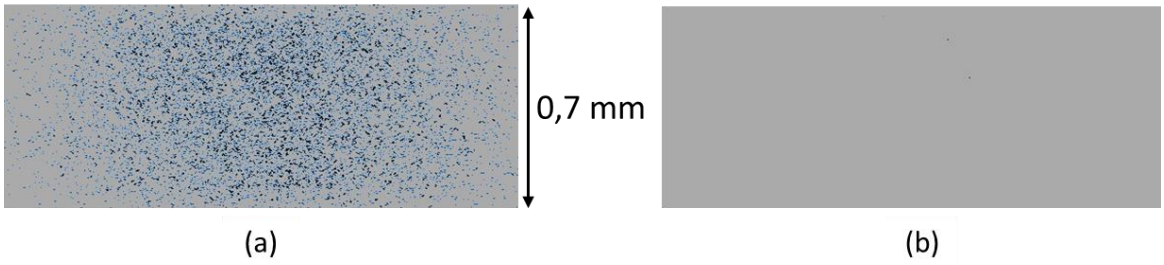

Figure 22: Visualization of the "voids" in the 25CrMo4 sample based on X-ray tomography analysis (a) As captured and without any filters. It shows a large number of particles due to the noise effect. (b) The same sample after applying the two filters. The number of particles is very low (only 3 particles were detected).

In summary, based on X ray-tomography scans, the particles detected in the forged sample and the 25CrMo4 sample do not correspond to porosity. They are a result of the salt and pepper noise and in order to avoid this problem, tomography data need to be filtered before studying them. In our work, the filtering procedure consisted of two filtering steps as explained earlier. This procedure was applied automatically on all the samples to reduce the effect of the noise on the results. Finally, it is very important to take into consideration the possibility of losing some information because of the limited resolution and the filtering procedure. For a sample that contains voids, it is possible that the very small voids will be not detected due to the limited resolution of the scanning (1.5 µm). Additionally, a part of these small voids, even if they were detected, still can be deleted from the final data because of the filtering procedure. For instance, in our case, the total volume of voids measured in the cast specimens decreased on average by 12% after filtering.

II.4 Electrochemical permeation (EP)

This method was presented by Devanathan and Stachurski [110] to investigate hydrogen permeation behavior in metals [111]. In this study, electrochemical permeation tests were performed in order to study hydrogen diffusion and hydrogen trapping in cast and forged samples.

The permeation experiment consists in introducing hydrogen into a sample from one side (charging cell) and detecting hydrogen atoms (hydrogen flux) that desorb from the other side (detection cell). The permeation experiment is composed of two steps, the charging phase and the discharging phase. Figure 23 shows the typical hydrogen flux curve measured at the detection side in a permeation test. The hydrogen flux (current density) on the exit side is constantly recorded. During the first step, hydrogen is continuously introduced from the charging side. At the beginning, there is no flux at the exit side and then, when hydrogen reaches the detection side, the flux rises until reaching a steady state. At this point, the hydrogen charging is stopped and the discharging step starts. The hydrogen flux continues to decrease until there is no more diffusible hydrogen inside the sample (flux equals to zero).

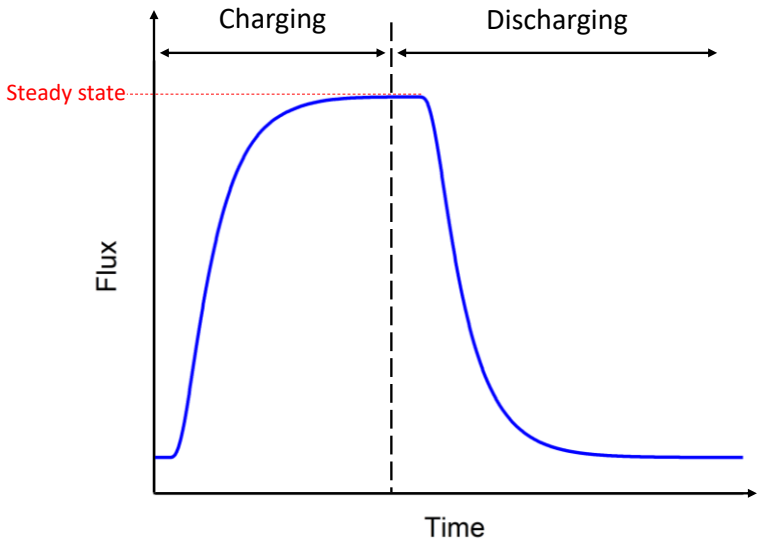

Figure 23: Typical flux curve obtained during a permeation experiment.

The experimental setup used in this study is presented in Figure 24. It is composed of two compartments: the charging cell and the detection cell. In order to describe in details these two compartments, a scheme is also presented in Figure 25. Each compartment was equipped with a saturated calomel reference electrode (SCE), a platinum auxiliary electrode and a

common working electrode which was the studied sample. The working electrode was placed between the two cells and the contact surface was a circular area of 0.785 cm^2. Each compartment was filled with a 0.1 M NaOH aqueous solution which was constantly deoxygenated by nitrogen bubbling (oxygen content is around 8 ppb). The solution was in constant circulation for the entire duration of the test. Without any dissolved oxygen in the solution, hydrogen reaction is the only electrochemical process happening during the experiment [112].

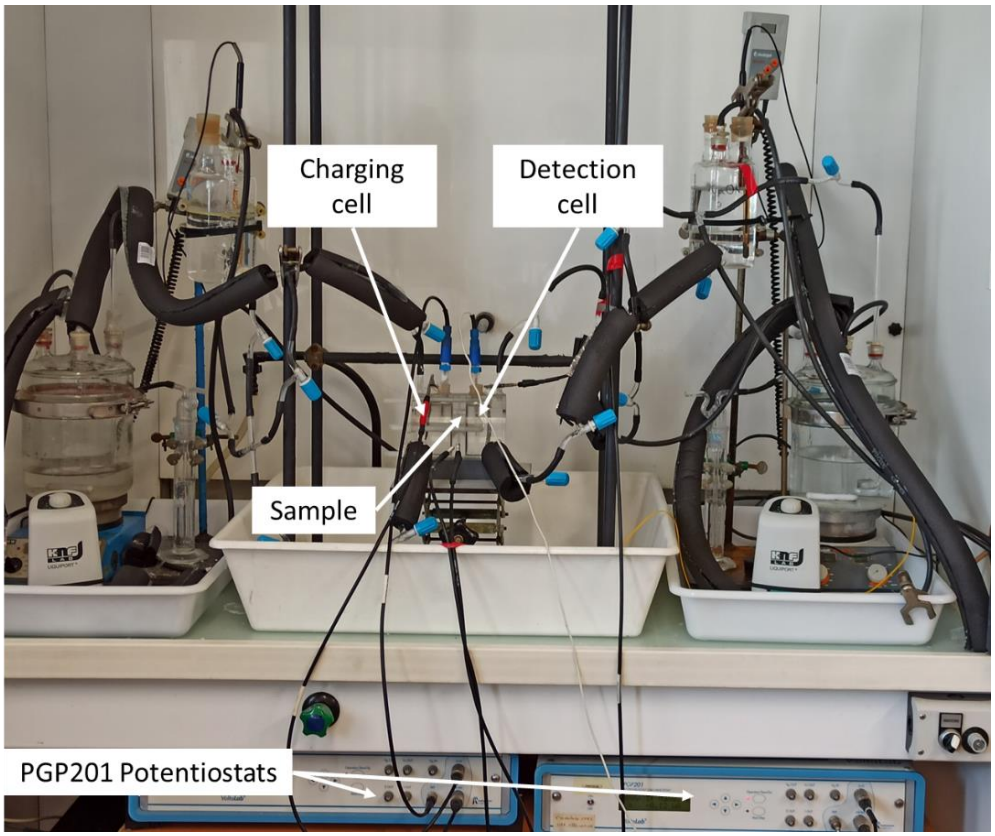

Figure 24: The hydrogen permeation experimental setup used in this study.

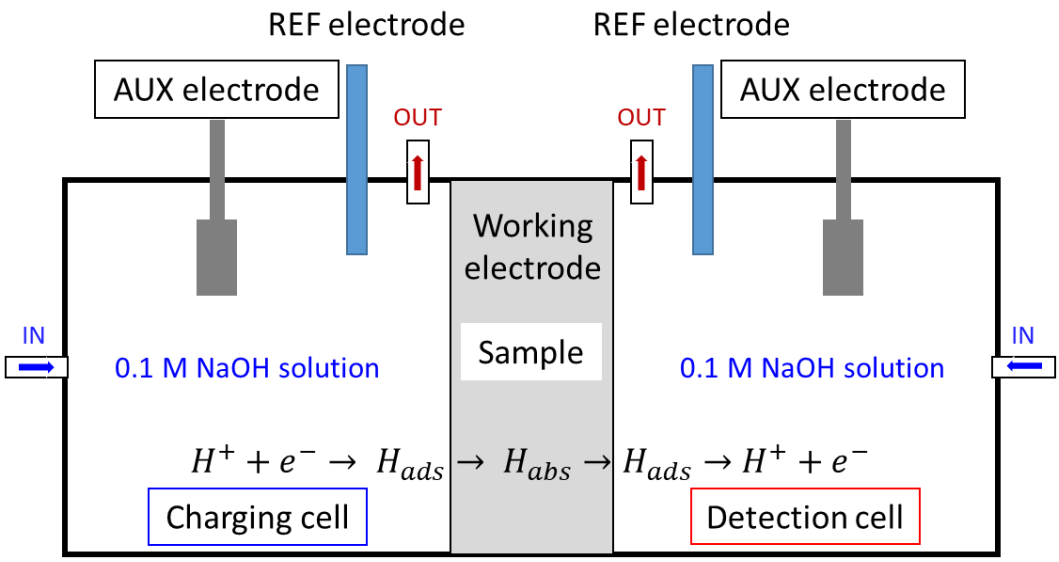

Figure 25: Schematic representation of the electrochemical permeation set-up used in this study.

All permeation specimens were obtained from the normalized bars. They were ground on the two sides using emery paper up to 2500 grits followed by polishing with a 3 µm and then 1 µm diamond paste. Just before mounting the specimen in the setup, they were cleaned in acetone and ethanol. The final thickness of the specimen ranges from 1 .80 mm to 1.96 mm.

All permeation tests were performed at room temperature and PGP201 potentiostats were used. At first, a polarization test was done on a cast and a forged sample in a 0.1 M NaOH solution with a scan rate of 1 mV/s from -100 mV/SCE to -1700 mV/SCE. Figure 26 shows the polarization curves for the forged and the cast samples. It shows that the two samples have approximately the same behavior. Based on these findings, the entry side was galvanostatically polarized at -800 µA/cm² corresponding approximately to a cathodic potential of -1200 mV/SCE to introduce hydrogen. An anodic potential of – 300 mV/SCE, corresponding to +50 mV/OCP (Open Circuit Potential) was applied on the exit side to oxidize hydrogen atoms reaching the exit surface. The oxidation of hydrogen atoms on the exit side is registered as the evolution of the current density as a function of time. However, not all the diffused hydrogen will be oxidized because some hydrogen will recombine into molecular hydrogen [113]. Before starting permeation experiments, the detection side was maintained at -300mV/SCE in order to determine the background current. It was stabilized at ~ -120 nA/cm² after 2 hours. This operation is called the passivation step used to produce a stable iron-oxide layer. Then, when the charging step is over, i.e. when the steady state is reached, the current density that was applied on the entry side is set to zero in order to start

the desorption step. The apparent diffusion coefficient, D_{app} (m^2/s) calculated in this work are determined using the time lag method from the permeation rise transient [114]:

$$D_{app} = \frac{e^2}{6t_l} \quad (20)$$

where e is the sample thickness (m) and t_l (s) represents the time when the current density at the exit side is equal to 0.63 of the steady-state current density.

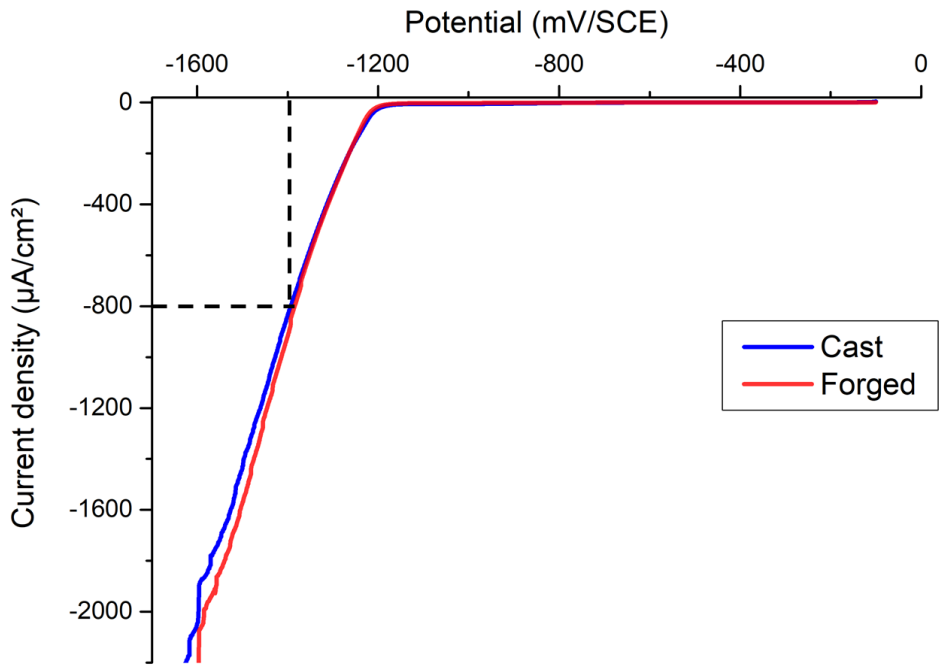

Figure 26: Polarization curves of the cast and the forged materials performed in a deoxygenated 0.1 M NaOH solution at room temperature. The scan rate was 1 mV/s. The two samples present the same behavior.

II.5 Chemical charging technique

Hydrogen can be introduced into samples by using a chemical charging method. It consists in immersing samples in an ammonium thiocyanate (NH_4SCN) aqueous solution heated at 50°C. This method is largely used to evaluate HE susceptibility of prestressed concrete steels [115]. The amount of absorbed hydrogen can be modified by varying the NH_4SCN concentration of the solution.

In this study, rectangular plate samples (11x26x1.9 mm) were used for chemical charging and subsequent TDS measurements. These samples were first cut from the forged and the

cast bars and were then ground with SiC paper up to 1200 grit. Finally, they were cleaned with acetone just before the immersion in the NH_4SCN aqueous solution. It should be mentioned that only one sample at a time was immersed in the NH_4SCN aqueous solution (80 ml of volume) and that the solution was used only one time. After charging, the samples were ground once again with 1200 SiC paper and cleaned with acetone. In fact, during the immersion, there is formation of a corrosion film. Consequently, it is very important to remove this layer before starting the TDS measurement in order to have trustworthy results because this layer can be a source of contamination. Finally, since the oxide layer was manually removed using SiC paper, the final thickness of the samples was not always the same. It ranged between 1.70 mm and 1.85 mm.

Figure 27 presents the weight loss due to corrosion during chemical hydrogen charging for a cast sample as a function of the immersion time in two NH_4SCN aqueous solutions with different NH_4SCN concentrations (5 wt% and 20 wt%). An increase of weight loss with immersion time is observed, especially after 24 h of immersion where the rate of weight loss is higher. It also could be noticed that the 20 wt% solution is more corrosive than the 5 wt% solution. For 24 h of immersion, the weight loss in the 20 wt% solution is three times higher than in the 5 wt% solution. In addition, after immersion, the sample has to be polished in order to remove the corrosion film, as mentioned earlier. This grinding step implies an additional reduction of weight by 0.2% for the 5 wt% solution and 0.8% for the 20 wt% solution. This difference is due to the thickness of the corrosion film. However, the total weight loss does not exceed 4% in any case, which is acceptable.

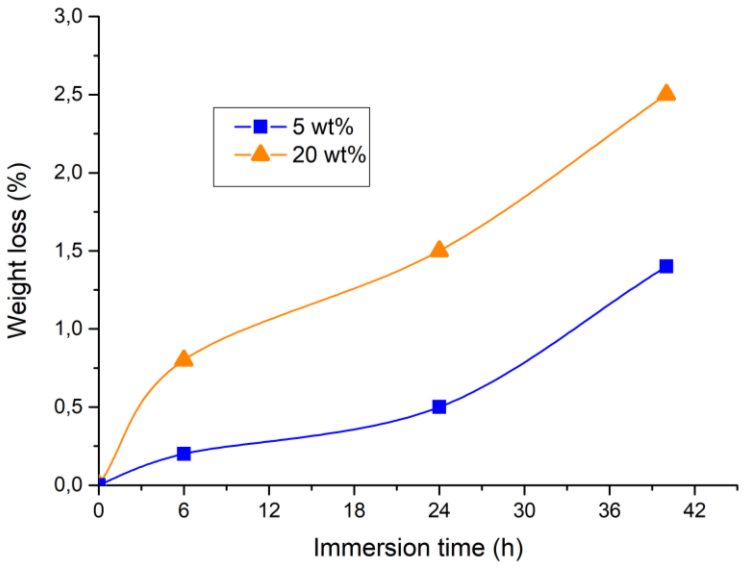

Figure 27: Weight loss of a steel specimen as a function of the immersion time in two different NH_4SCN solutions (5 wt% and 20 wt% concentrations) at 50°C.

II.6 Thermal desorption spectroscopy (TDS)

TDS is commonly used to study gas desorption from metals [116][117]. It permits to determine the hydrogen trapping energies for different traps (grain boundaries, interfaces, dislocations…) as well as the hydrogen concentration in the analyzed samples [118][119]. In this work, all the TDS measurements were performed using a Pfeiffer QMG 220 PrismaPlus quadrupole mass spectrometer. The experimental setup used in this study is presented in Figure 28. The experiment consists in measuring the amount of desorbed hydrogen from a charged steel sample while a continuous heating is applied by means of a tubular furnace. The furnace used in this work can reach a heating rate of 100°C/min and a maximum temperature of 1000°C. The TDS measurement output is a spectrum in which the intensity (number of ions) is plotted as a function of time (or temperature). The quantity of the desorbed hydrogen can be estimated after calibrating the mass spectrometer signal. This point will be discussed in details later. It should be mentioned that for hydrogen spectra, the mass 2 was monitored here. Figure 29 gives a schematic illustration of the TDS apparatus. First, it should be mentioned that the measurement stage is kept constantly under high vacuum (10^{-8} mbar) by means of a rotary pump first and then a turbo pump. For this reason, the valve A must be kept close all the time except when the measurement starts. At the beginning of the experiment, the sample is loaded inside the quartz tube and then the pumping down from atmospheric pressure in the preparation stage starts (rotary pump first and then the turbo pump). The

duration of the pumping is discussed later. At this point, the user ascends the furnace until the sample is completely covered. When the pumping step is finished, the user closes valve B and opens valve A. Now, it is possible to start the measurement. In this case, the user launches the measurement using the computer (by means of Quadera software). Once the measurement is finished, the user closes valve A first and then opens valve B. He must wait until the furnace has cooled down to room temperature before starting a second measurement. In order to extract the sample and insert a new one, the user opens valve C to introduce an inert gas (Argon) inside the preparation stage to break the vacuum. It should be mentioned that the valves next to the turbo pump and the rotary pump must be closed to avoid degradation. Finally, the user is able to remove the sample from the quartz tube.

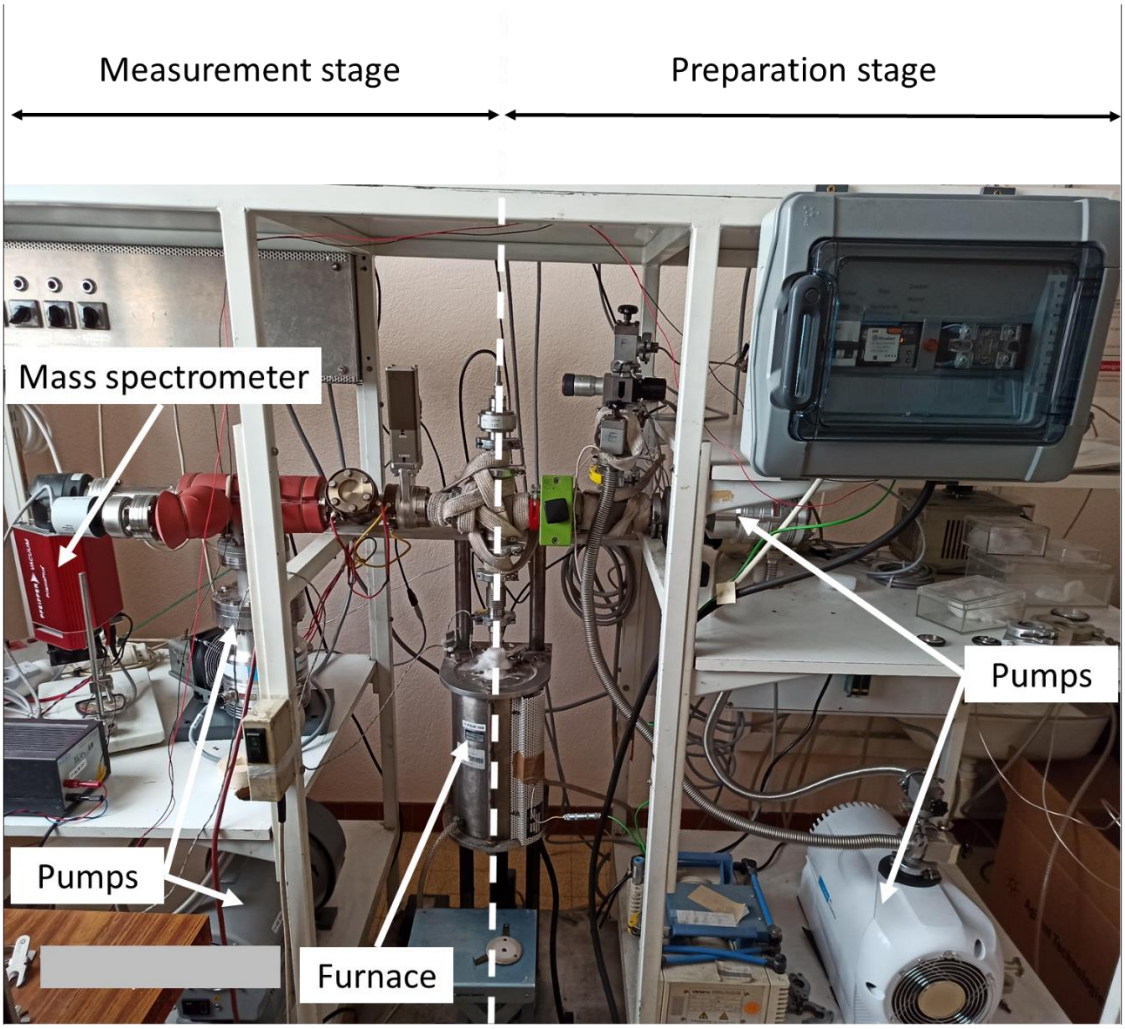

Figure 28: TDS experimental setup used in this study.

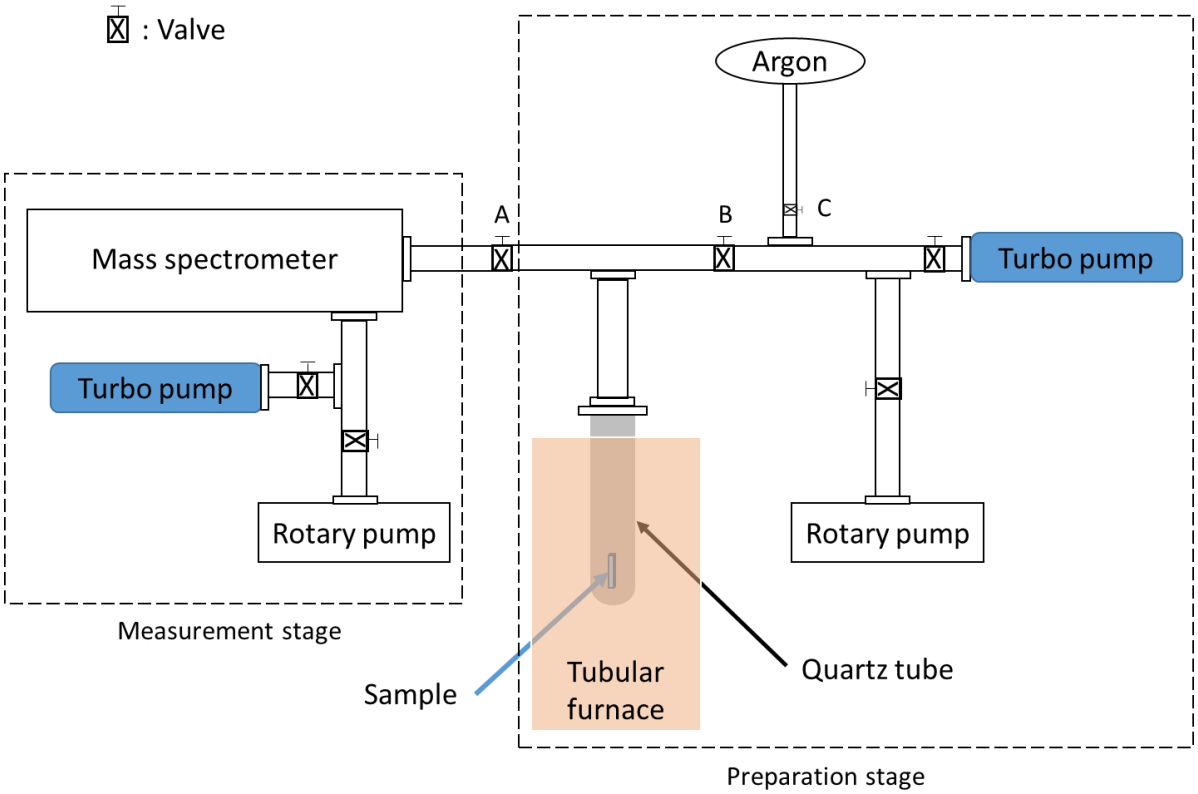

Figure 29: Schematic illustration of the TDS equipment used in this study.

An important point in TDS measurements is the effect of the adsorbed water on the sample surfaces and the quartz tube. This problem has been reported in several studies [120][121][122] and authors concluded that peaks of hydrogen, related to the dissociation of adsorbed water on the sample surfaces, can appear after exposing the sample to the atmosphere even for a short period [121][122]. For this reason and before interpreting the results, the interfering effect of the adsorbed water was thoroughly investigated in order to separate the hydrogen coming from inside the sample and the hydrogen related to the adsorbed water. Figure 30 shows the results of TDS measurements performed on five different samples without any hydrogen charging. The pumping time was 15 minutes (time between the sample introduction and the beginning of the heating) and the samples were heated up to 900°C with a heating rate of 10°C/min. First, by comparing the different spectra, approximately the same profile is observed with several peaks above 500°C. No peak was detected below 500°C. The samples used in this experiment were not charged with hydrogen, thus it is most likely that these high temperature peaks are due mainly to the adsorbed water on the sample surfaces as mentioned in the literature [120][121][122]. However, even if it is less probable, these peaks could be related to the hydrogen that could be irreversibly trapped

during the manufacturing process of the material. Therefore, in order to clarify this issue, one sample was analyzed four times under different situations. Figure 31 summarizes the four measurements that were performed on this sample without hydrogen charging and with a heating rate of 10°C/min. The first measurement (dark blue curve) was performed directly after 15 minutes of pumping. The result shows a profile similar to the profiles obtained from the measurements of the previous samples (see Figure 30). It shows several peaks located above 550°C. In addition, no peak was detected below 500°C as before. After this first measurement, all hydrogen (if any) and water should be entirely desorbed from the sample. In order to verify this assumption, the same sample was kept inside the TDS equipment during cooling back to room temperature, before launching a second measurement (i.e. the sample was not exposed to the atmosphere). This second measurement (curve in sky blue), in contrast to the first one, does not show any peaks below or beyond 500°C. This confirms that the sample does not contain any hydrogen nor adsorbed water. However, it should be mentioned that the obtained signal rises slowly at high temperatures (from 600°C). We assume that this increase is due to the hydrogen (or water) that is still adsorbed on the quartz tube and the other parts of the equipment that connect the quartz tube to the mass spectrometer. After that, the sample was unloaded from the TDS, exposed to the atmosphere for two minutes (to allow re-adsorption of water) and then reanalyzed. As it can be seen from Figure 31, a similar profile to the first experiment was found, which contains high temperatures peaks. Therefore, this measurement proves that the peaks detected at high temperatures do not correspond to hydrogen coming from inside the sample because all hydrogen (if any) was desorbed during the two first measurements. Instead, it is associated to the decomposition of the water on the sample surfaces. More precisely, it is a result of the catalytic decomposition that took place at the sample surfaces as described in Venezuela's work [121]. Furthermore, it should be mentioned that the height of the peaks in this case was smaller than the first measurement. This difference could be associated to the exposure time to the atmosphere, because for the first measurement, the sample was exposed for days, whereas for the second measurement, the sample was exposed to the atmosphere for two minutes only. Finally, the last experiment consisted in keeping the sample inside the TDS equipment without unloading for an additional 24 h (under high vacuum) before starting the measurement. The result of this measurement (red curve) shows no peak at all and no increase in the signal at high temperatures unlike the

increase that was found in the second measurement. In this case, we assume that the 24 h pumping was largely enough to remove all the adsorbed compounds from the instrument.

To summarize, the peaks that were detected at high temperatures for all the samples (without any hydrogen charging) are mainly associated with the decomposition of the water on the sample surfaces, which produces evidently hydrogen. This water can come from the specimen surface itself, or, more probably, from the setup (quartz tube, equipment parts…). As showed earlier, even a small exposure time to the atmosphere is capable to interfere considerably with the measurement. In our case, hydrogen peaks coming from adsorbed water start to appear only beyond 500°C for a heating rate of 10°C/min. In addition, no peak was detected for temperatures inferior to 500°C. Therefore, all TDS measurements presented in this work were limited to a temperature of 500°C in order to avoid the problem of the adsorbed water on the sample surfaces.

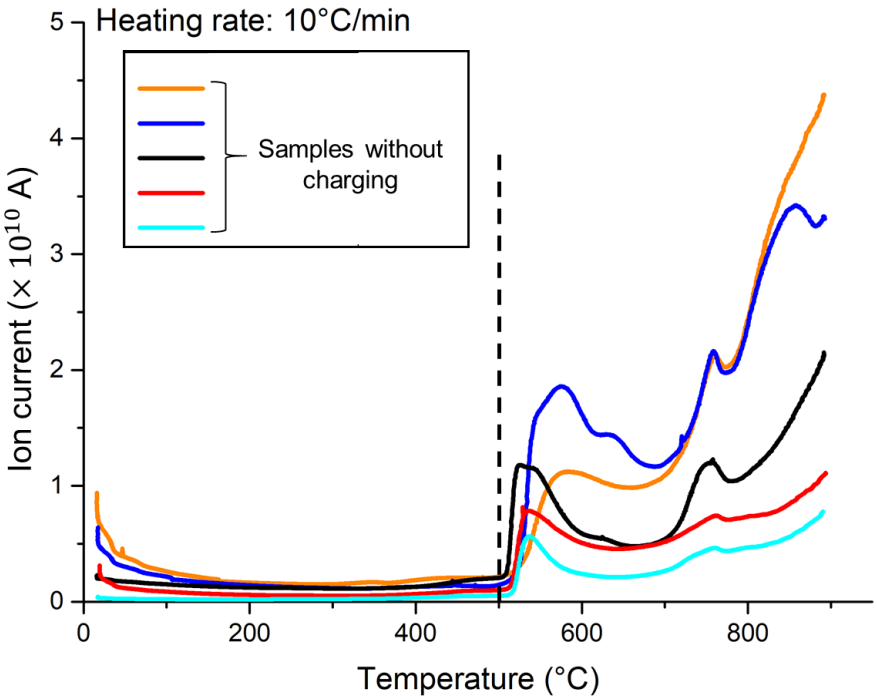

Figure 30: Hydrogen TDS spectra of five different samples without hydrogen charging. The samples were rectangular plates (11x26x1.9 mm). The heating rate is 10°C/min.

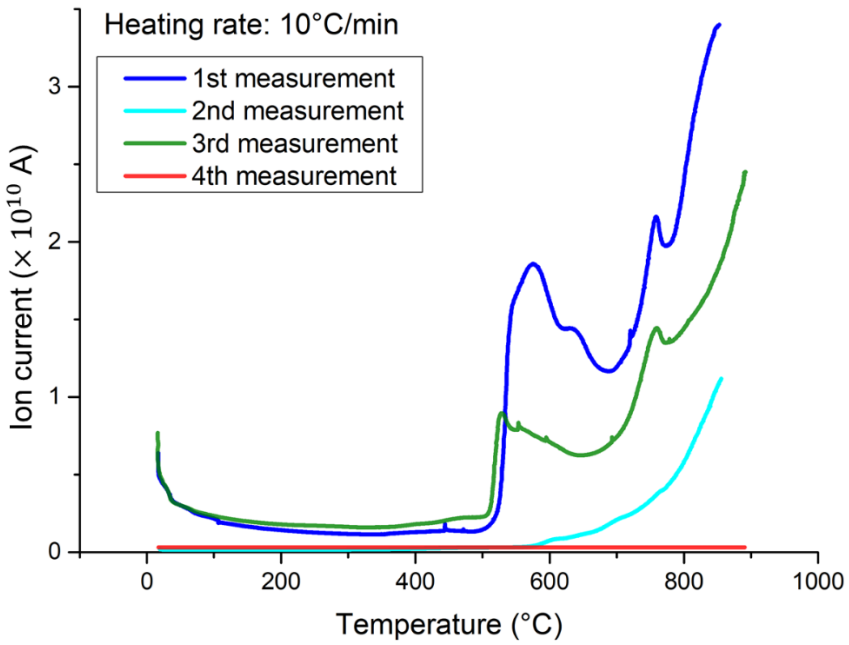

Figure 31: Hydrogen TDS spectra of the same sample (without hydrogen charging) performed under different situations. The 1st measurement was performed directly after 15 minutes of pumping. The sample was exposed to the atmosphere for days. The 2nd measurement was performed on the same sample without re-exposure to the atmosphere. The 3rd measurement was conducted after exposing the sample to the atmosphere for 2 minutes and the 4th measurement was done after 24 h under high vacuum without re-exposure to the atmosphere.

Interestingly, another artefact was found during TDS analysis. A sample was analyzed four times without any hydrogen charging. The measurements were performed under the same conditions: the pumping time was 15 minutes and the heating rate was 10°C/min up to 900°C. The first time (P1200*), the sample was ground up to P1200 using P240, P600 and P1200 abrasive paper. The second time (P1200), the sample was ground using only P1200 abrasive paper. The third time (P4000), the sample was ground up to P4000 using three different abrasive papers: P1200, P2500 and P4000. In these three cases, the measurements were performed directly after grinding. In the fourth time (P4000*), the sample was ground exactly as in the third time (P1200, P2500 and P4000) but the measurement was performed after 24 h. During this time, the sample was stored in a small plastic bag. It should be mentioned that the grinding step was performed using water and that the samples were cleaned with acetone and dried with hot air after grinding. The TDS results are presented in Figure 32. First, as it can be seen, the four TDS spectra have high temperature peaks. These peaks were discussed in the previous section. In the temperature range between 0 and 500°C, no peak was detected in the case of P1200 grinding (light blue curve) and the P4000* grinding where

the measurement was performed 24 h after grinding (blue curve). However, a peak was found in the other measurements and it is located around 250°C. Since the sample was not charged with hydrogen, this peak can only be explained by the surface contamination during grinding. Actually, the grinding operation was performed using water; therefore, it is possible that some hydrogen containing compounds (such as hydroxyls) were formed on the sample surface during the grinding. In addition, it looks like this peak is related to the grinding time (time in contact with water) because the peak was only found in the case of P1200* grinding and P4000 grinding where the grinding operation took a “long” time. In fact, the P1200* and the P4000 grindings took about 3 minutes while the grinding with P1200 only took 30 seconds. It can be seen also that this peak disappeared when the sample was stored for 24 h after the P4000 grinding. It is possible that the hydrogen containing compounds formed on the sample surface during grinding decomposed during the 24 h storage, thus no peak was found. As this is not one of the objectives of this study, no further investigations were made to fully understand the origin of this artefact. However, even though the peak height is low compared to those observed on H charged samples (see next chapter), all the samples were only ground with P1200 abrasive paper for approximately 30 s to avoid any contribution of this peak in the total hydrogen signal.

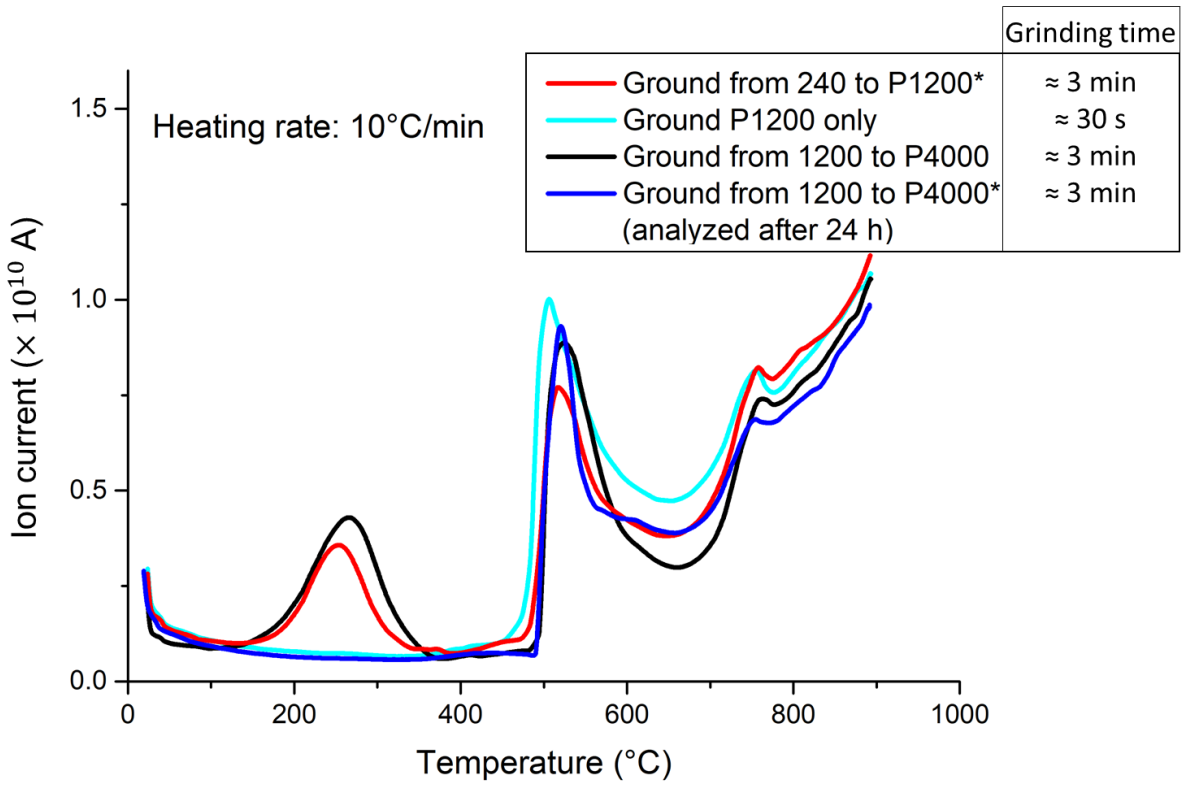

Figure 32: Hydrogen TDS spectra of the same sample after different grindings. The sample was rectangular plate (11x26x1.9 mm). The heating rate was 10°C/min and the pumping time was 15 minutes. The sample was cleaned with acetone and dried with hot air after each grinding. The first three measurements (red, light blue and black curves) were performed directly after grinding. The blue curve corresponds to a TDS measurement performed after a storage time of 24 h. The TDS spectra show a peak at 250°C which is attributed to the surface contamination during grinding. The high temperature peaks are related to the adsorbed water on the sample surface.

Before starting the TDS measurement, it is necessary to launch the pumping operation first in order to reach high vacuum (≈10^{-8} mbar) which is required for operating mass spectrometers. Once the sample is inserted in the instrument, it takes time to reach a good level of vacuum inside the equipment. It should be mentioned also that the pumping time can highly affect the quality of the measurement. Figure 33 shows the TDS spectra for two different pumping times. The two experiments were performed with a heating rate of 10°C/min and without inserting any sample (only the empty quartz tube was analyzed). The black and red curves represent the background TDS signal for the 15 minutes and 60 minutes pumping experiments, respectively. It is clear that the signal obtained with 15 minutes of pumping is much higher than that with 60 minutes of pumping. With increasing the pumping time, the background signal becomes lower. Therefore, the pumping operation is considered a very important step in TDS analysis. Meanwhile, during the pumping operation, a part of the hydrogen called

“diffusible hydrogen” can escape from the sample especially in the case of certain materials where hydrogen is very mobile [123]. This feature must be taken into consideration when interpreting TDS data. In this study, for all the TDS measurements presented later, a pumping time of 60 minutes was used because it presents a good compromise between a low background signal and a reasonable loss of hydrogen from the samples (around 10% of loss).

Finally, it should be noted that all TDS samples were charged chemically (the charging operation is explained in the previous section) and that the time between the end of the hydrogen charging operation and the beginning of the TDS measurement is about 75 minutes. This time includes the specimen preparation (the removal of the oxide layer that was formed during the charging step and the introduction of the specimen into the TDS instrument) and a pumping time (around 60 minutes) to reach a high vacuum in the TDS instrument.

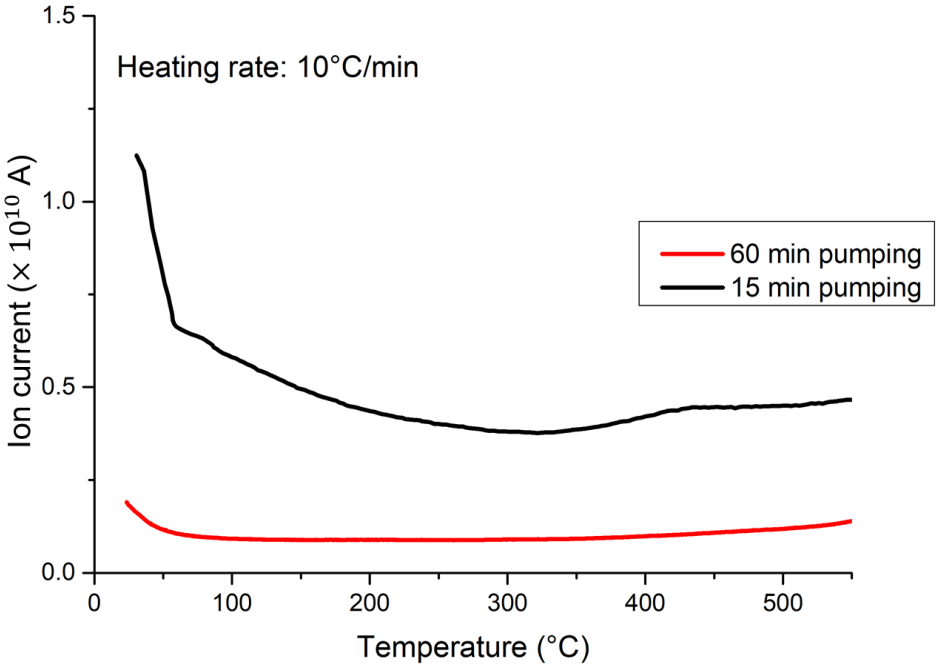

Figure 33: The influence of pumping time on the TDS background signal. Hydrogen TDS spectra obtained after 60 minutes (red curve) and after 15 minutes (black curve) of pumping. The measurements were performed on an empty quartz tube (without any sample).

The TDS instrument used in this study was calibrated using commercial hydrogen standards (titanium pins and steel pins) purchased from LECO France. Titanium standards have an average mass of 0.12 g and a certified hydrogen concentration of 103 ± 7 wt ppm, which represents a hydrogen mass of 12.4×10^{-6} g, whereas steel standards have a nominal mass of

1 g and a hydrogen concentration of 8.1 ± 0.8 wt ppm, which corresponds to a hydrogen mass of 8.1×10^{-6} g. In our calibration procedure, the standards were analyzed with a heating rate of 10°C/min up to 900°C with an additional holding at 900°C for 30 minutes in order to be sure that all the hydrogen desorbed from these standards. However, as proved earlier, there is a possible contribution of the adsorbed water on the specimen and/or the quartz tube to the TDS signal above 500°C. Consequently, it is important to subtract the possible signal associated to the adsorbed water from the total TDS signal. Figure 34 presents the TDS spectra for a steel standard analyzed in the as-received state (dark blue curve), analyzed again without re-exposure to atmosphere after 24 h in high vacuum (light blue curve). The same standard was also analyzed again after re-exposure to atmosphere (red curve). It can be seen that there is a slight contribution from the instrument background (light blue curve) at high temperatures and also a slight contribution from the adsorbed water too although much smaller than that observed on the G20MN5 steel specimens in Figure 31. The red curve in Figure 34 is a combination of the instrument background and the adsorbed water on the sample. Thus, this combined contribution should be deducted from the measurement of the standard in the as-received state. As mentioned earlier, the TDS measurements on steel specimens presented in this study are limited to 500°C, thus there is no contribution from the adsorbed water on the sample surface nor from the instrument background.

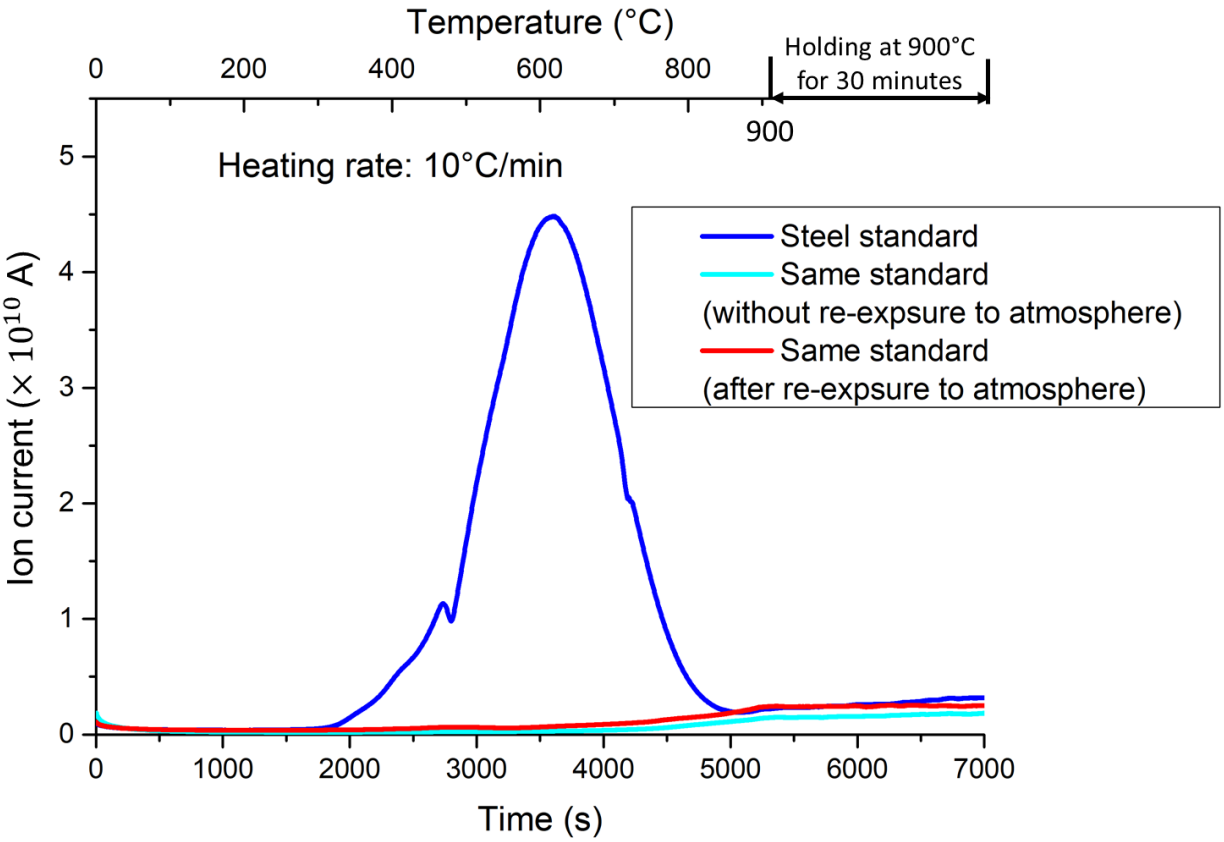

Figure 34: TDS spectra for a steel calibration standard analyzed as-received (blue curve), re-analyzed without exposure to atmosphere (light blue curve) and then re-analyzed after re-exposure to the atmosphere (red curve). Heating to 900°C at 10°C/min and then holding at 900°C for 30 minutes. It shows a slight contribution of the adsorbed water in TDS measurements at high temperatures.

Figure 35 summarizes the TDS measurements performed on several titanium and steel standards. These standards were heated with a heating rate of 10°C/min up to 900°C and with an additional holding at 900°C for 30 minutes. The spectra were obtained after deduction of the contribution of the adsorbed water obtained from a TDS measurement conducted on the same standard specimen after re-exposure to atmoshpere. The area under the titanium standard curve represents a hydrogen mass of 12.4×10^{-6} g and the area under the steel standard curve represents 8.1×10^{-6} g of hydrogen. This data permitted to plot the calibration curve presented in Figure 36. It represents the relationship between the integrated area and hydrogen concentration. The error bars represent the statistical error of the hydrogen concentration in the standards (103 ± 7 wt ppm for the titanium standards and 8.1 ± 0.8 wt ppm for the steel standards). The linear relation of Figure 36 was used to determine hydrogen concentration values in all the TDS analysis presented later in this study. It should be mentioned that the hydrogen mass of the H charged samples used in this work was between

0.5×10^{-6} g and 7×10^{-6} g. Finally, as it can be seen in Figure 36, the linear relation did not fit the experimental points perfectly. Therefore, in order to give more accurate results in the future, we should use other standards with a hydrogen mass below 8×10^{-6} g.

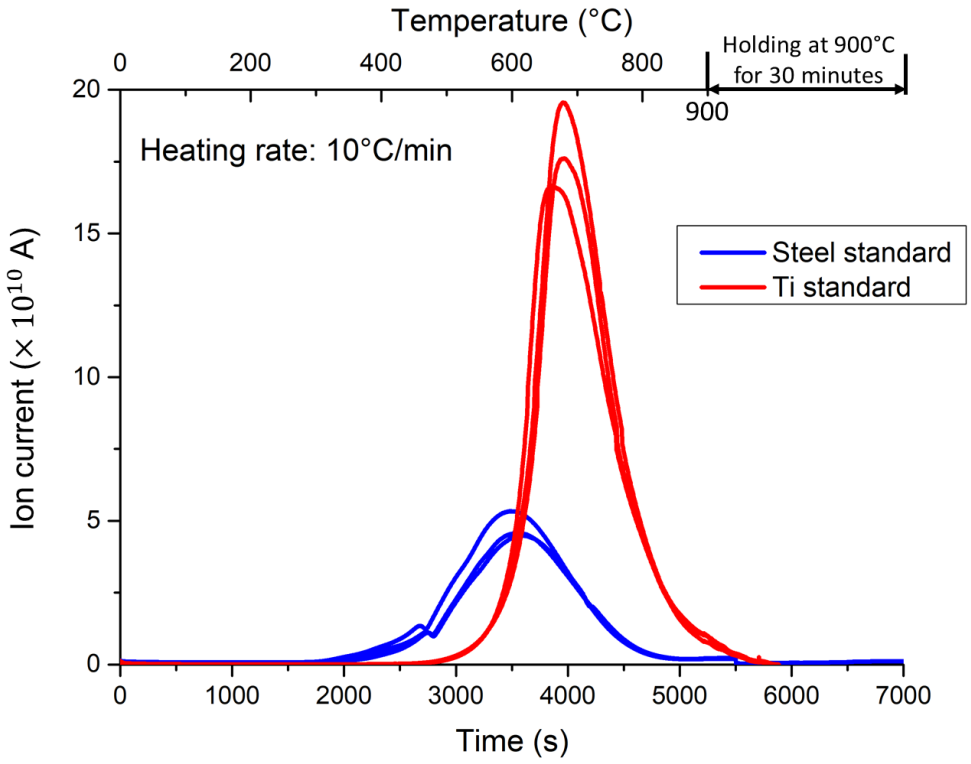

Figure 35: TDS spectra of the hydrogen calibration standards after deduction of the contribution of the adsorbed water. Heating rate = 10°C/min up to 900°C + 30 minutes holding at 900°C. The steel standards are presented in blue (nominal mass of the standard = 1 g, hydrogen content = 8.1 ± 0.8 wt ppm, hydrogen mass = 8.1×10^{-6} g) and the titanium standards are presented in red (nominal mass of the standard = 0.12 g, hydrogen content = 103 ± 7 wt ppm, hydrogen mass = 12.4×10^{-6} g).

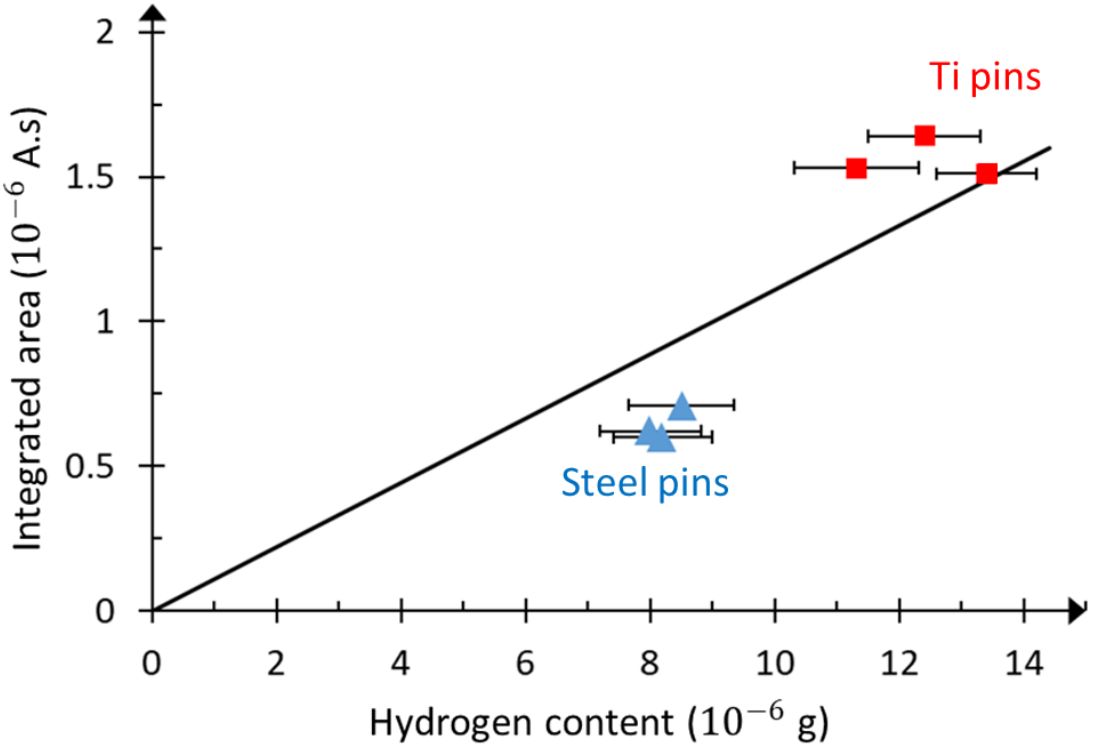

Figure 36: The relationship between the TDS peak integrated area and the hydrogen content in the calibration standards.

II.7 Specimens and tensile tests configuration

Tensile test specimens used in this study were obtained from the forged and the cast bars. It is important to recall that the forged and the cast bars were obtained from the same material and they have the same microstructure. The only difference lies in the porosity. The specimen shape and dimensions are presented in Figure 37 (a). The initial thickness was 2.1 mm but after grinding and polishing up to 1 µm using diamond paste (see Figure 37 (b)), the final thickness was between 1.9 and 2 mm. It should be mentioned that the specimens were chemically charged in a NH_4SCN aqueous solution heated at 50°C as explained previously. Before hydrogen charging, the volume fraction of porosity of each specimen was determined by hydrostatic weighing technique as explained earlier.

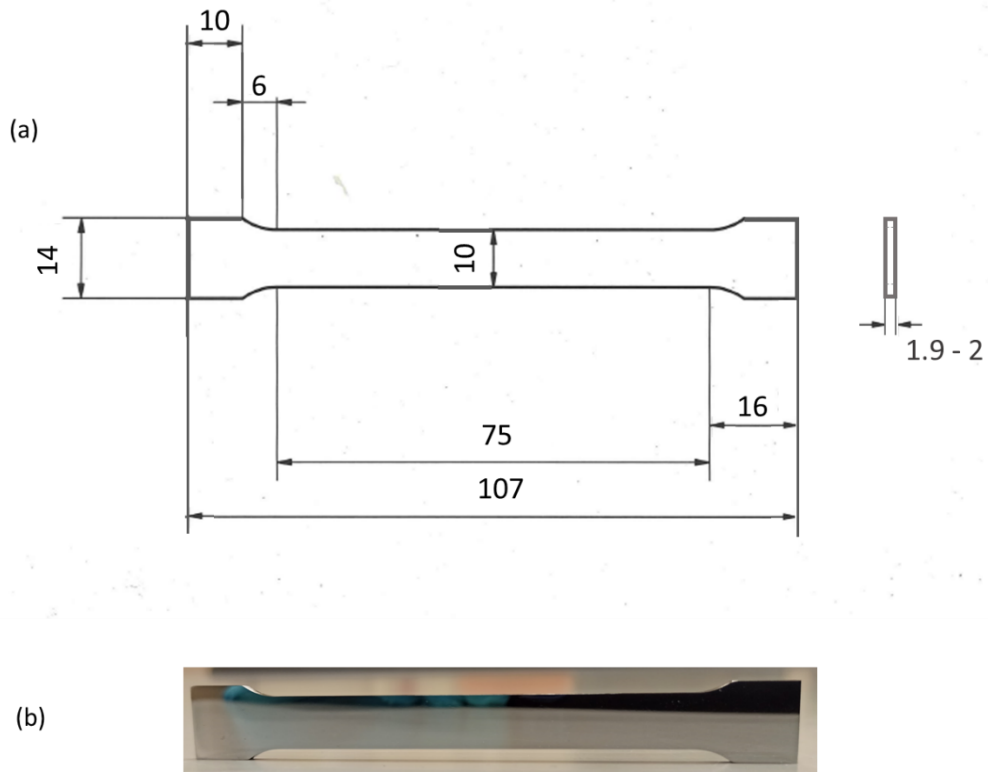

Figure 37**:** (a) The geometry of the tensile test specimen used in this study in mm. (b) The specimen after polishing up to 1 µm. The final thickness is between 1.9 mm and 2 mm.

The tensile testing machine used in this study was of type SCHENCK coupled with Wavematrix software. The recorded parameters are the load, the specimen displacement (using an extensometer) and the crosshead displacement. The stress was calculated by dividing the load by the minimum initial cross-section perpendicular to the load axis. All the tests were conducted at room temperature and the applied strain rate was 3×10^{-4} s^{-1}. The tests were performed on uncharged and on H-pre-charged specimens. After hydrogen charging, the specimen was dried and then installed on the tensile testing machine. The time needed to install the specimen was 7 minutes and the time to run the tensile test was around 18 minutes. This total time of 25 minutes is not long enough to offer the possibility to hydrogen to quit the specimen in significant amount. Usually, the specimen deformation is obtained by the extensometer displacement but unfortunately, in this case, the extensometer could not cover the entire length of the specimen as presented in Figure 38. Therefore, a correction of the displacement data (measured by the extensometer) was needed in order to obtain the correct deformation especially in the case when the failure occurred outside the lower and the upper arms of the extensometer.

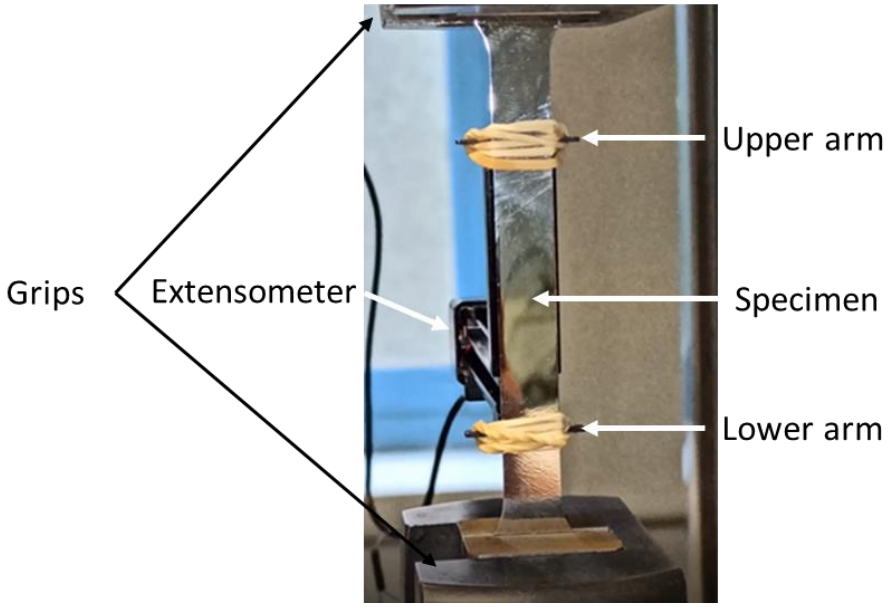

Figure 38: The specimen was placed in the tensile machine first and then the extensometer was installed on the specimen. The extensometer does not cover the whole length of the specimen.

The correction procedure is composed of two steps. The first step consists in considering the elongation values that were measured by the extensometer from the start of the test until the point where the stress is equal to 95% of the ultimate tensile strength (UTS). Then, the second step consists in replacing the elongation values measured using the extensometer by elongation values deduced from the crosshead movement from 95% of UTS until failure occurs. Figure 39 (a) shows the stress-strain curves plotted based on the extensometer measurement (red curve) and the crosshead movement (black curve). The corrected curve is a combination of the elongation measured by the extensometer (until 95% UTS) and the elongation deduced from the crosshead movement as illustrated in Figure 39 (b). Actually, the deformation spreads uniformly across the length of the specimen until UTS and then the deformation becomes non-uniform. When necking starts to occur at UTS, the deformation is concentrated in the necking region. Then, when this region is outside the extensometer arms, the deformation is underestimated by the extensometer measurement. Thus, in this case, the elongation beyond UTS was deduced from the crosshead movement. It is important to note that the crosshead displacement includes the specimen elongation and the device elastic deformation (fixing systems, grips). After the UTS, the load decreases which leads to the decrease of the elastic deformation of the device. This results in slightly underestimating the specimen deformation. However, the final elongation values given by the corrected curve are

close to the real specimen elongation measured manually after fracture, as shown Figure 39 (b).

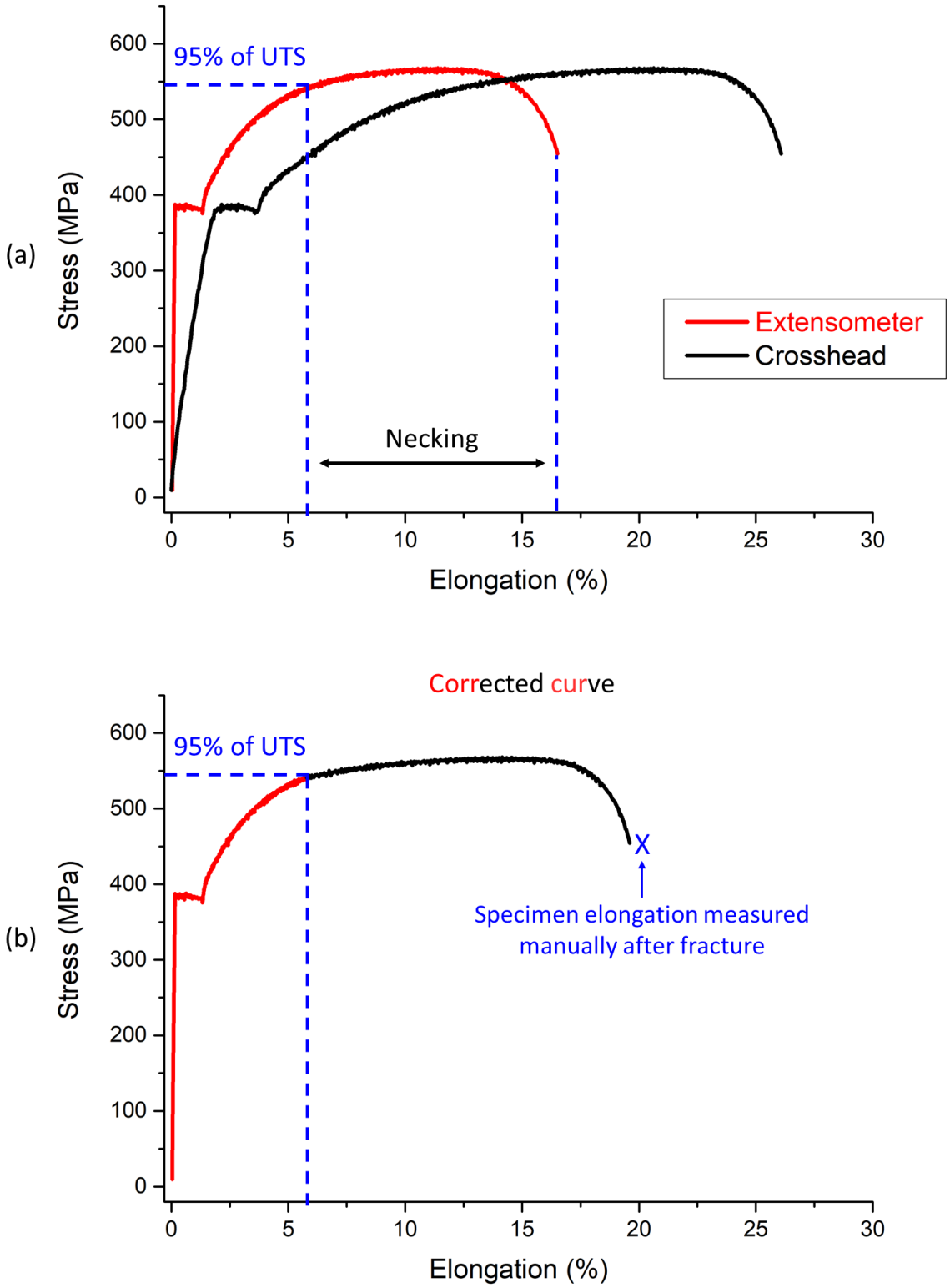

Figure 39: The correction operation used to plot the stress-strain curve (a) the stress-strain curves based on the extensometer data (blue curve) and the crosshead movement (black curve). (b) the stress-strain curve after correction using a combination of the extensometer data and the crosshead movement.

Chapter 3: Hydrogen trapping and diffusion

III.1 Introduction

As already mentioned in the first chapter, it has been well proved that hydrogen represents a harmful element for steels because it leads to a serious decrease in mechanical properties, especially loss of ductility [3][4][62]. Thus, in order to increase HE resistance and prevent brutal failures, it is crucial to investigate hydrogen behavior in steels and more precisely in cast steels for our case. The particularity of these cast steels lies in the porosity as explained previously. Therefore, it is important to study the effect of porosities on hydrogen diffusion and trapping. In this chapter, a comparative study between forged and cast samples is made based on EP and TDS experiments. This comparison will help us to understand better the interaction between hydrogen and porosity and will provide some answers about the contradictory conclusions found in the literature such as the reversible or irreversible nature of hydrogen trapping in porosity.

First, the microstructure of the forged and the cast materials are characterized in order to verify if there are major differences. In addition, the porosity is investigated for both material using X-ray tomography. Then, a series of EP tests are performed on several samples with different porosity fraction. Both charging and discharging phases are studied. After that, TDS measurements are conducted on forged and cast samples after hydrogen charging. Different aspects are explored such as the effect of the porosity fraction on the amount of trapped hydrogen and the physical state of this trapped hydrogen (atomic adsorbed on the internal surfaces of the porosities or gaseous hydrogen H_2). These two techniques are complementary and the results are used to highlight the influence of porosity on the hydrogen diffusion and trapping processes. Finally, from the TDS data a method is proposed in order to calculate hydrogen fugacity of the charging solution used, as well as the hydrogen solubility (Sieverts constant) of the studied material.

III.2 Results and discussions

III.2.1 Material characterization

III.2.1.1 Porosity characterization

A forged sample and a cast sample were scanned using X-ray tomography in order to characterize the porosity. The same procedure that was explained in details in the previous chapter was used. In addition, the same thresholding was applied on all the samples in order to identify the voids inside the material. Figure 40 (a) and (b) present cross section images of a cast sample and a forged sample, respectively. The absence of porosity has been established for the forged sample studied here, whereas, the presence of cavities in the cast sample is clearly evidenced.

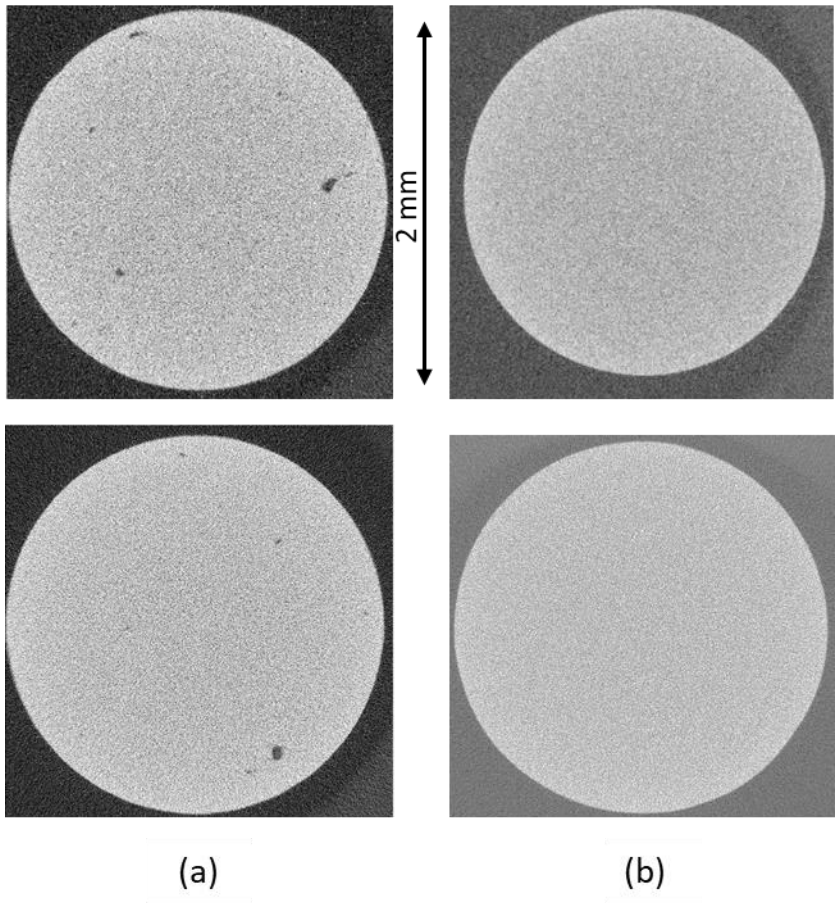

Figure 40: Cross sectional views of (a) a cast sample (b) a forged sample based on X-ray tomography data, showing a few cavities in the cast sample and the absence of porosity in the forged sample.

The X-ray reconstructed volume for the cast sample is presented in Figure 41. It shows clearly the presence of cavities (blue particles). In general, it appears that the cavities are

evenly distributed over the sample. However, the size and the shape are different from one pore to another. This 3D volume reconstruction is a very useful tool to obtain relevant statistical information on the porosity inside the sample.

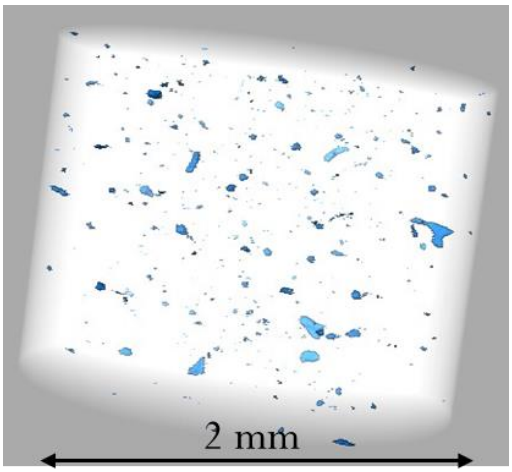

Figure 41: 3D volume rendering of a cast sample based on X-ray tomography, showing the distribution of the cavities.

This 3D volume was investigated in order to quantify and to characterize the porosity in the cast material. Figure 42 shows the distribution of porosities based on their equivalent diameter. The equivalent diameter of a particle is defined as the diameter of a sphere that has the same volume as the measured particle. The histogram shows that the majority of cavities (nearly 96%) have an equivalent diameter inferior to 20 µm and that the maximum equivalent diameter is equal to 68 µm. Table 2 gives additional information on the porosity features. In this specimen, the average equivalent diameter of cavities is 7.6 µm and the volume of voids represents 0.05 % of the total volume of the sample.

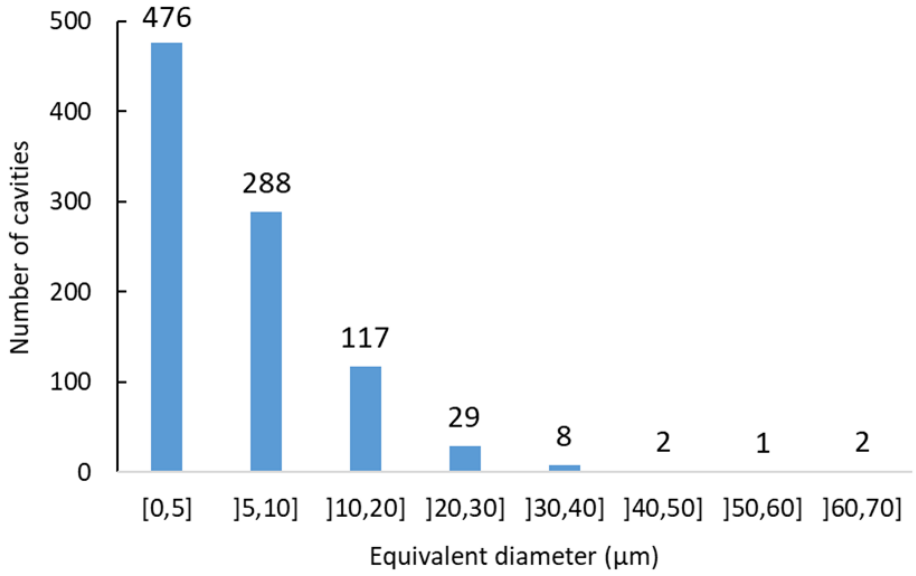

Figure 42: The distribution of the cavities based on their equivalent diameter obtained from X-ray tomography. Most of cavities have an equivalent diameter inferior to 20 µm.

Table 2: Porosity features in a cast sample obtained using X-ray tomography.

Total number of cavities	Average equivalent diameter (µm)	Cavity density (mm^{-3})	Inter-cavity distance (µm)	Porosity fraction (%)
923	7.6	380	138	0.05

In this work, it was not possible to obtain the porosity fraction of EP samples (26x20x1.9 mm) and TDS samples (11x26x1.9 mm) by X-tomography scans because of constraints on the specimens' size and shape. Therefore, the hydrostatic weighing technique was used to determine the porosity volume fraction for EP and TDS specimens.

The reference density was that of the forged material as it was shown earlier that this material has no porosity. The cast samples were taken from different zones in the ingot in order to have different porosity fraction from one sample to another. Table 3 summarizes the results of the hydrostatic weighing technique performed on the cast samples. The uncertainty of these results is around 0.02%.

Table 3: The volume fraction of porosity for different cast samples determined by the hydrostatic weighing technique.

	EP samples		TDS samples				
	1	2	1	2	3	4	5
Volume fraction of porosity (%)	0.04	0.07	0.13	0.18	0.20	0.25	0.27

Finally, we should mention that the terms: porosity, cavity, microvoid and void are used interchangeably in this work and they all refer to microporosity.

III.2.1.2 Microstructural characterization

As in the previous chapter, the cast and forged bars were normalized at 880°C for 60 minutes. Forged and cast samples were ground and polished to 1 µm, then they were etched using a 5% Nital solution (ethanol + nitric acid). Figure 43 (a) and (b) present optical micrographs of the cast and forged materials, respectively. A typical ferrite–pearlite microstructure is observed in both cases. The fraction of pearlite was determined using ImageJ software. This fraction is equal to 29 ± 2% and 32 ± 3% for the cast material and the forged material, respectively. The ferrite grain size is about 12.6 ± 1.2 µm for the cast sample and 11.6 ± 1.0 µm for the forged sample.

Several metallographic observations, at different places of the samples, showed a similar microstructure in both materials. Thus, if a significant difference in hydrogen behavior is found between a forged sample and a cast sample, it should be related to a difference in porosity, not in microstructure.

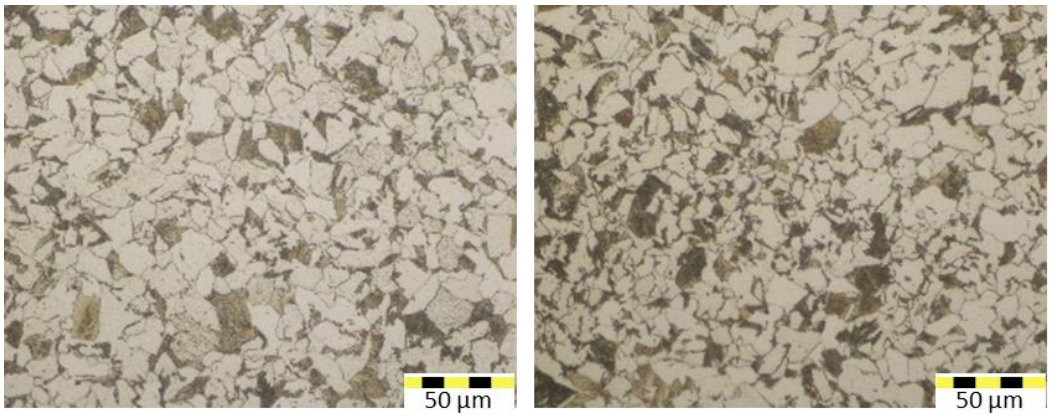

Figure 43: Optical micrographs of etched (a) cast sample and (b) forged sample showing a ferritic-pearlitic microstructure.

III.2.2 Hydrogen electrochemical permeation

The permeation experiments were performed at room temperature. Three samples (1 forged sample + 2 cast samples) have been tested under the same conditions. Hydrogen permeation results are expressed in normalized current density (J/J_{max}, with J_{max} the steady state-current), as a function of the normalized time (t/e^2, with t the time in seconds and e the specimen thickness in meter). This normalization was made to remove the dependence of results on sample thickness. The values of the current density at the steady state (J_{max}) are displayed in Table 4.

Table 4: Samples characteristics and hydrogen permeation results. J_{max} is the hydrogen flux at the steady state, D_{app} is the apparent diffusion coefficient calculated using the time-lag method based on the flux of the final steady state and D_1 is the apparent diffusion coefficient calculated using the time-lag method based on the flux of the pseudo-steady state.

Sample	Porosity fraction(%)	Thickness (mm)	J_{max} (nA/cm²)	D_{app} (m²/s)	D_1 (m²/s)
Forged	0	1.96	1220	7.8×10^{-12}	2.4×10^{-10}
Cast 1	0.07 ± 0.02	1.96	1180	3.3×10^{-12}	2.5×10^{-10}
Cast 2	0.04 ± 0.02	1.83	1375	3.8×10^{-12}	2.4×10^{-10}

Liu et al. studied the influence of the microstructure on hydrogen permeation and trapping in steels [124]. The materials used in their study were pure iron and two ferritic-pearlitic steels (AISI 1018 and AISI 4340) that have a similar chemical composition and a similar microstructure to our material. The results of their study revealed that there are mainly two types of trapping sites. The first type include ferrite grain boundaries and dislocations and the second type corresponds to the ferrite-cementite interfaces. Thus, we assume that our material should contain the same trapping sites due to the close similarity of the microstructures and the chemical compositions.

The aim of this section is to compare the hydrogen permeation results between the forged and the cast samples to reveal the role of porosity in the hydrogen trapping and diffusion phenomena. As explained earlier, the only difference between the samples was the porosity. Therefore, if any significant variation in the permeation behavior will occur, it is beyond all doubt due to the cavities.

Figure 44 (a) presents the permeation rising transients for the three samples. The results show that the forged sample reaches the steady state faster than the two cast samples. The apparent diffusion coefficients were calculated using the time-lag method (Eq.(20)). The diffusion coefficient is equal to 7.8×10^{-12} m²/s for the forged sample, 3.7×10^{-12} m²/s for the cast sample with a porosity fraction of 0.04% and 3.3×10^{-12} m²/s for the cast sample with a porosity fraction of 0.07%. In general, the decrease in hydrogen mobility is linked to the trapping sites because they absorb hydrogen, which leads to the decrease of the diffusion rate. In our case, the only difference between the forged sample and the cast samples is the porosity thus, it is clear that cavities act as hydrogen traps. The equilibrium is described by Sieverts' law which indicates that the lattice hydrogen concentration at a given depth of the permeation specimen is proportional to the square root of the pressure inside the cavity, or more precisely proportional to the square root of the fugacity [30]. It is then expected that, at any time, the amount of hydrogen stored in the cavities is proportional to the porosity fraction, which implies that the time needed to reach steady state should increase with increasing porosity fraction.

The hydrogen apparent diffusion coefficient (obtained using the 63% time-lag method) of the two cast samples is practically the same (3.7×10^{-12} m²/s and 3.3×10^{-12} m²/s), although there is almost a factor of two between their respective porosity fraction. More surprisingly, the

first part of the rising transient is even faster for the specimen with the highest porosity fraction. However, it should be kept in mind that porosity is not the only microstructural feature affecting the rising transient, as discussed later. In addition, it is to be reminded that the uncertainty on the porosity fraction is relatively high (± 0.02%), so the actual difference between the two fractions measured may be less than a factor of two.

Figure 44 (b) shows the same permeation results presented using a logarithmic time scale and Figure 45 shows a closer view of the beginning of the permeation curves. It is remarkable that the permeation curves obtained in this study show a double regime rising transient. At the beginning, there is no hydrogen flux (current density) at the exit side, then, when hydrogen atoms reach the detection side, a first rise is observed. It is noticeable that for the three samples, the hydrogen flux starts to rise approximately at the same moment ($t/e^2 \approx 3x10^8$ s/m^2). Then, well before reaching the final steady state, a pseudo-steady state is reached for the three samples at about $t/e^2 \approx 1.5x10^9$ s/m^2. Then, for $t/e^2 > 10^{10}$ s/m^2, the hydrogen flux starts to rise again until reaching the final steady-state. It is remarkable that the existence of this pseudo steady-state is not related to porosity as it exists in the forged specimen. It is thus inferred that it is related to the microstructure of the material, not to porosity.

The apparent diffusion coefficients were calculated for the first transient using the time-lag method. We found approximately the same value in the three experiments ($D_1 = 2.4x10^{-10}$ m^2/s), which is higher by about two orders of magnitude than the diffusion coefficients determined previously, ranging from 3.3 to $7.8x10^{-12}$ m^2/s. This shows that part of the hydrogen was able to diffuse across the specimen by following fast diffusion paths. Most probably, hydrogen diffused through the percolated ferrite corridors, without interacting too much with the porosities and/or the pearlite where hydrogen mobility can be affected [41] (because of the high trapping energy of the interfaces in pearlite, which is about 65 kJ/mol [42][43]). However, a detailed description of this mechanism would require more research and it is beyond the scope of this work that focuses on the effect of porosities.

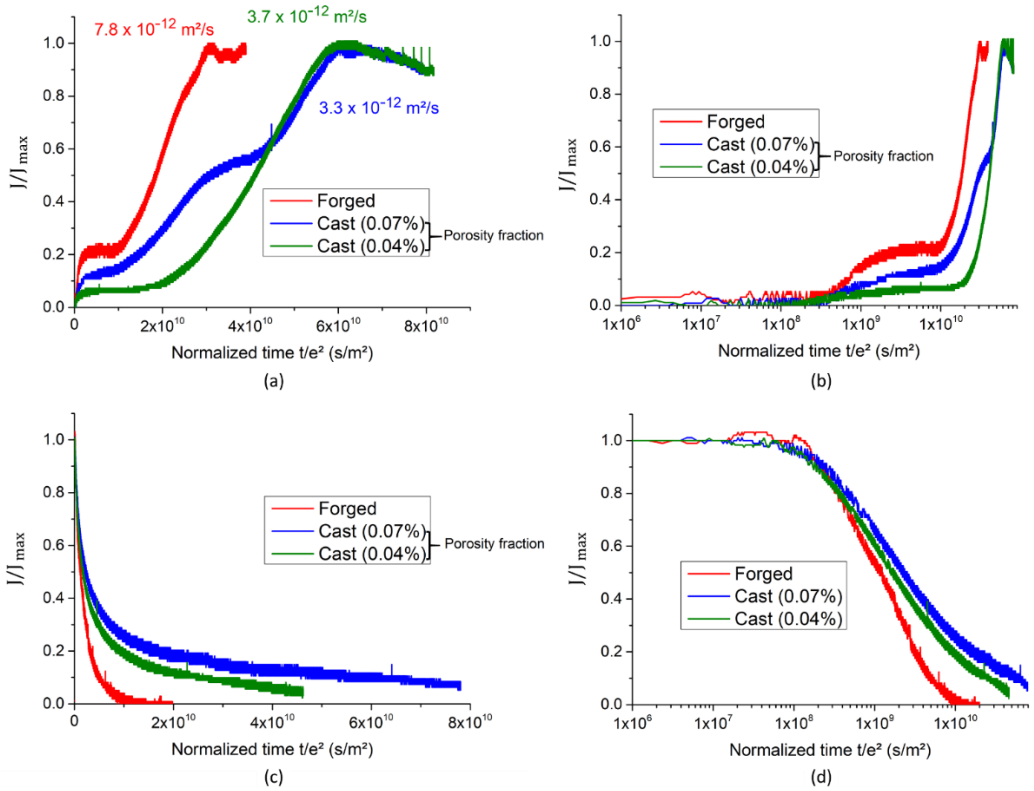

Figure 44: Electrochemical hydrogen permeation results for a forged sample (red curve), a cast sample with a porosity fraction of 0.07% (blue curve) and a cast sample with a porosity fraction of 0.04% (green curve). Permeation experiments were performed under the same conditions in a 0.1M NaOH aqueous solution at room temperature. (a) and (b) normalized rising transients, (c) and (d) normalized decaying transients.

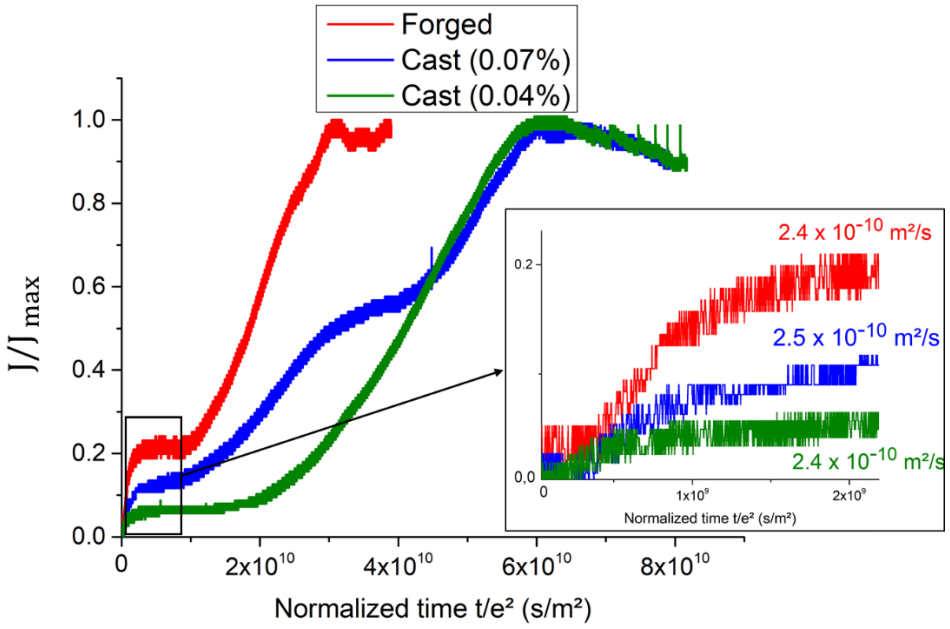

Figure 45: Normalized permeation rising transients for the three samples with a zoom on the beginning of the curves showing a plateau.

The effect of the porosity is also very clear during the decaying transient as illustrated in Figure 44 (c) and (d). The area under each curve reflects the quantity of hydrogen that desorbed through the detection side. Comparing the decaying transients, a significant difference in the amount of desorbed hydrogen can be noticed between the forged sample and the cast samples. Since the main distinction between the samples is the porosity, this difference in the desorbed hydrogen can only correspond to the hydrogen stored in the porosity. In addition, the comparison between the two cast samples shows that the amount of the desorbed hydrogen from the sample with a porosity fraction of 0.07% is almost twice the amount of the desorbed hydrogen from the cast sample with a porosity fraction of 0.04%. This suggests that the amount of absorbed hydrogen increases proportionally with increasing porosity fraction.

The hydrogen that desorbs at room temperature during the permeation decaying transient is a combination of lattice hydrogen and reversibly trapped hydrogen. The irreversibly trapped hydrogen, if any, could not desorb at room temperature. Consequently, it is safe to conclude that the porosity acts as a reversible trap for hydrogen at room temperature.

Figure 46 shows the decay transients for the forged sample and the cast sample with a porosity fraction of 0.07%. The hatched area (area between the two curves) represents the difference in the amount of desorbed hydrogen between the cast sample and the forged sample, which is the hydrogen trapped in the porosity. This hydrogen is about 85% of the total amount of the desorbed hydrogen from the cast sample. It should be noted that this percentage is probably underestimated, as the decaying transient of the cast specimen had not reached zero yet when the experiment was stopped.

To sum up, EP results showed that porosity plays an important role in hydrogen trapping and diffusion. The rising transients indicate that hydrogen diffusion rate is lower in the case of the cast samples compared to a sample without porosity. The decaying transients proved that the majority of hydrogen is located at the porosity and that this porosity acts as a reversible trap for hydrogen.

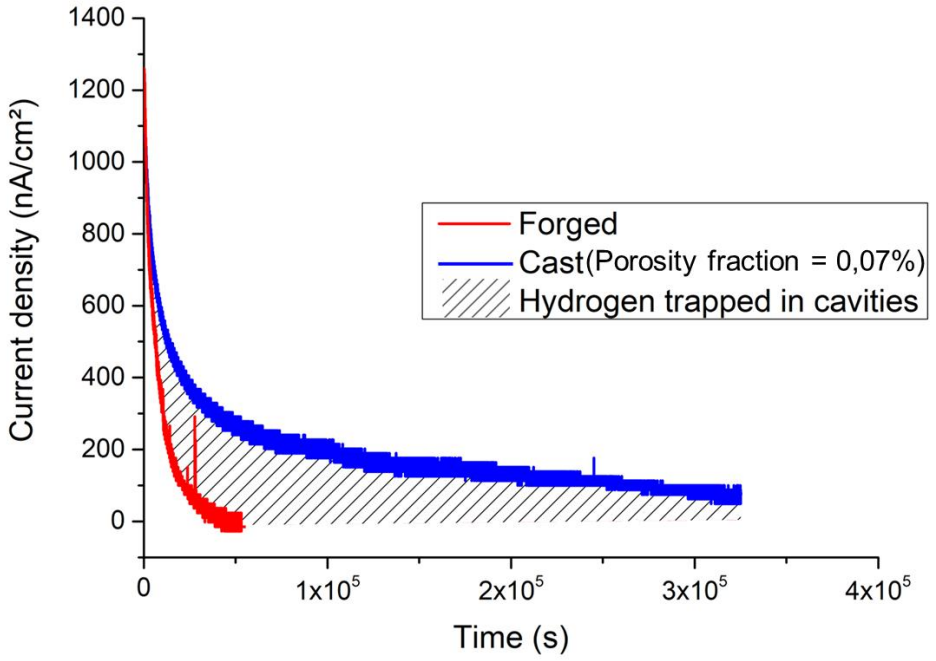

Figure 46: Decay transients for the forged sample (red curve) and the cast sample with a porosity fraction of 0.07% (blue curve).The area between the two curves represents the hydrogen trapped in the porosity. It corresponds to 85% of the total desorbed hydrogen.

III.2.3 Hydrogen thermal desorption spectroscopy

III.2.3.1 Hydrogen chemical charging

Before presenting the TDS results, a few points about the hydrogen chemical charging are discussed in this section. The charging temperature of 50°C was chosen to increase the hydrogen mobility and consequently decrease the charging time compared to charging at 20°C. In order to estimate the apparent diffusion coefficients at 50°C, we used the diffusion coefficients from our permeation tests (presented in the EP results section, these tests were performed at 20°C) and data from Sezgin et al. [63] and Husby at al. [125]. In their studies, they were able to obtain values of hydrogen diffusion coefficient at different temperatures for a material similar to ours. First, using the data from Sezgin et al., we calculated the ratio between the diffusion coefficients at 50°C and at 20°C ($D_{50°C}/D_{20°C}$). Similarly, using the data from Husby et al., we calculated the ratio between the diffusion coefficients at 45°C and at 15°C. We found that these ratios ranged between 1.9 and 2.6. Finally, we multiplied our diffusion coefficients, obtained from permeation at room temperature, by a factor of 2 in order to obtain an estimation of our apparent diffusion coefficients at 50°C. The results are

presented in Table 5. For the cast material, a diffusion coefficient of $3.3x10^{-12}$ m²/s at room temperature was considered here.

Table 5: The apparent diffusion coefficients obtained by the time-lag method based on electrochemical permeation tests and the estimated values of these coefficients at 50°C.

$D_{app}[m^2/s]$	Forged	Cast
at 20°C (permeation test)	7.8×10^{-12}	3.3×10^{-12}
at 50°C (estimation)	1.6×10^{-11}	6.6×10^{-12}

Numerical simulations of hydrogen charging were performed using the estimated apparent diffusion coefficients at 50°C. These simulations were obtained using a simple resolution of the diffusion equation (Eq.(12)). Figure 47 (a) and (b) present the time-dependence of the concentration profiles for a cast sample and a forged sample, respectively. For a forged sample, 24 h of charging should be enough to reach a homogenous concentration inside the sample, within 98%. However, for a cast sample, it appears that after 24 h the hydrogen distribution is not homogenous (the average concentration inside the sample is about 83% of the subsurface concentration after 24 h and it is 95% after 40 h). It should be mentioned however that the simulated concentration profile is only an approximation as the diffusion coefficient used in the simulation is not accurately known. Indeed this apparent diffusion coefficient is expected to depend on the porosity fraction, which can significantly vary from one specimen to another, as shown later.

Increasing the charging time would certainly ensure a more homogeneous hydrogen distribution inside the sample but for practical reasons we limited the charging time to 24 h. The effect of the charging time on hydrogen content will be discussed later. Another way to ensure a more homogenous hydrogen distribution is by decreasing the specimen thickness. Unfortunately, this solution is not recommended in our study because this decrease will lead to a much higher uncertainty in the determination of the volume fraction of porosity.

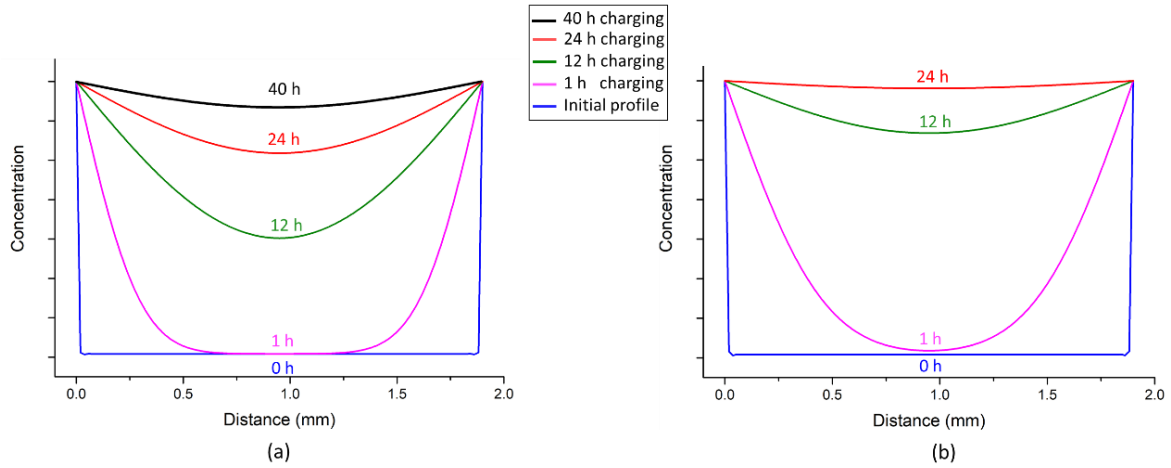

Figure 47: Concentration profiles of hydrogen at various times estimated by numerical simulation of the charging operation at 50°C. The thickness, in both simulations, is 1.9 mm. (a) cast sample with an apparent diffusion coefficient of 6.6 x 10^{-12} m²/s. (b) forged sample with an apparent diffusion coefficient of 1.6 x 10^{-11} m²/s.

III.2.3.2 Solution concentration and hydrogen content

In order to highlight the effect of the NH_4SCN concentration of the charging solution on the amount of hydrogen absorbed in the material, the same cast sample was analyzed by TDS several times. At each time, the sample was immersed in an aqueous solution with a specific mass concentration of NH_4SCN (0%, 1%, 2%, 5% and 20%) for 24 h. The solution was continuously heated at 50°C. Then, the TDS measurements were performed with a heating rate of 10°C/min up to 500°C. After the last measurement, the microstructure was investigated under optical microscope to ensure that the repetitive heating to 500°C had no impact on the microstructure.

The desorption spectra for the different NH_4SCN concentrations are shown in Figure 48 (a). The hydrogen concentrations indicated in the legend were obtained by integration of each curve. These results indicate that the amount of hydrogen absorbed in the material increases when the NH_4SCN solution concentration is increased. For instance, with the increase of the NH_4SCN mass fraction from 1% to 5%, the hydrogen content has doubled from 0.60 wt ppm to 1.22 wt ppm. A similar trend was found by Takagi et al.[126]. Figure 48 (b) presents the influence of the NH_4SCN concentration on the hydrogen content. The hydrogen content is plateauing for NH_4SCN concentrations above 5%: the increase in hydrogen content is of 0.24 wt ppm (19%) only when the NH_4SCN concentration is increased from 5 wt% to 20 wt%.

Finally, a hydrogen peak is clearly evidenced on the TDS spectrum after immersion in pure water, which corresponds to a hydrogen content of 0.07 wt ppm. It is assumed that corrosion reactions take place even in pure water at the specimen surface, which results in hydrogen absorption.

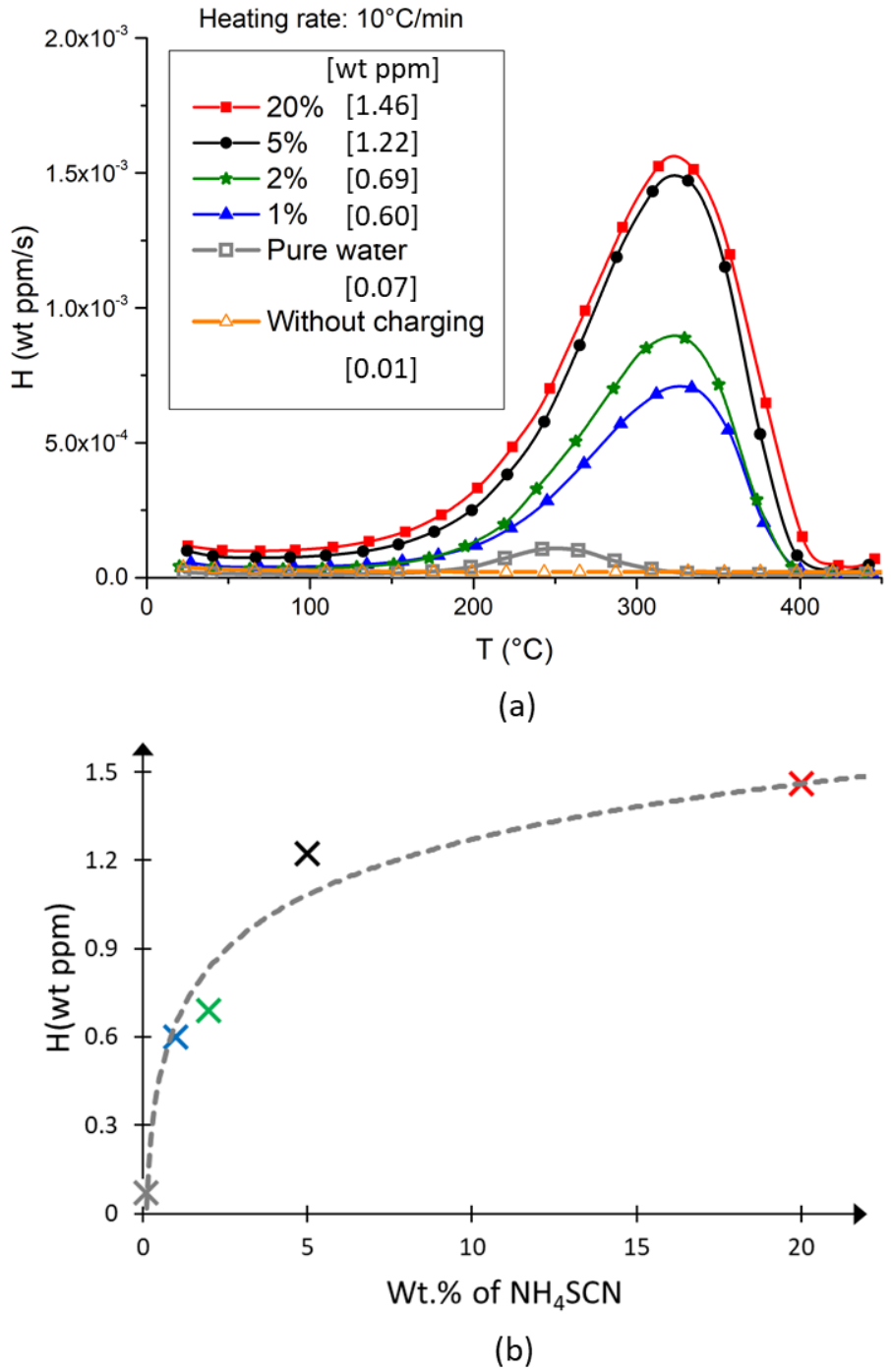

Figure 48: The effect of the NH_4SCN solution concentration on the hydrogen content for a cast sample after 24h of immersion (a) TDS spectra; heating rate = 10°C/min (b) Hydrogen content as a function of the charging solution concentration. The hydrogen content was evaluated from TDS peak integration. The same sample was used for all the experiments.

III.2.3.3 Charging time and hydrogen content

The aim of this section is to investigate the influence of the charging time on hydrogen content. Four charging operations were performed on the same cast sample and after each charging operation the hydrogen content was measured using TDS. Charging was conducted in a NH_4SCN aqueous solution heated at 50°C for two different durations and two NH_4SCN concentrations. Figure 49 (a) shows the TDS results (heating rate 10°C/min) for the four charging conditions. The hydrogen content increases with increasing the solution concentration as explained earlier for both charging times. Figure 49 (b) illustrates the evolution of the amount of absorbed hydrogen as a function of the charging time. For both concentrations, the increase of hydrogen content from 24 h to 40 h of charging is relatively small, especially for the 5 wt% solution where the difference is only 0.15 wt ppm, which represents 12% of increase. This increase is similar to what has been obtained earlier by numerical simulations (see Figure 47). The numerical results showed an increase of 14% between 24 h and 40 h of charging.

To sum up, since 40 h of charging, for both solution concentrations, do not increase significantly the final hydrogen content, 24 h of charging was considered more adequate.

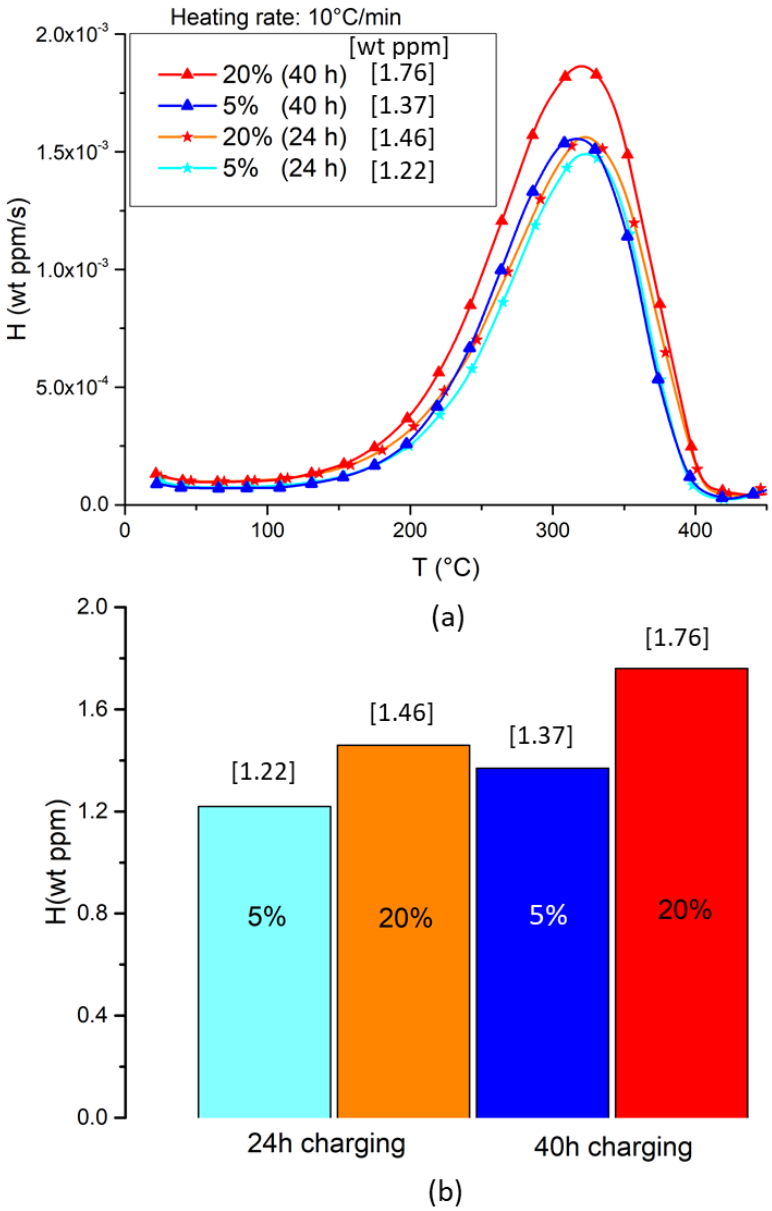

Figure 49: The influence of the immersion time on the amount of absorbed hydrogen for two different NH_4SCN concentrations (5 wt% solution and 20 wt% solution) (a) TDS spectra; heating rate = 10°C/min (b) Hydrogen content as a function of immersion time for two charging solution concentrations. The hydrogen content was evaluated from TDS peak integration. The same sample was used for all the experiments.

III.2.3.4 The role of porosity in the hydrogen trapping process

In order to investigate the role of porosity in the hydrogen trapping process, two samples were chemically charged for 24 h under the same conditions as described earlier. The first sample was a cast one (thickness = 1.82 mm) with a volume fraction of porosity of 0.27%. The second was a forged sample (thickness = 1.85 mm). After charging, TDS measurements were performed with a heating rate of 10°C/min up to 500°C. The results are presented in Figure 50. An additional non-charged cast specimen was studied as well to ensure the absence of

hydrogen in the initial state (grey curve in Figure 50). When comparing the TDS spectra, it can be observed from the area under the curve that there is a huge difference in the amount of desorbed hydrogen between the cast and the forged specimens. For the cast sample (blue curve), the desorption peak maximum is located at 340°C and the amount of the desorbed hydrogen is 1.50 wt ppm. For the forged sample (red curve), the peak maximum is at about 260°C and the amount of hydrogen is only 0.16 wt ppm, which is very low compared to the cast sample. This significant difference corresponds to the amount of hydrogen trapped in the cavities (hatched area) because, as explained earlier, the only difference between the two samples lies in the porosity. Therefore, it can be concluded that cavities are traps for hydrogen. Furthermore, another interesting conclusion can be made which is that the absorbed hydrogen is essentially located at cavities (90% in this case, calculated by dividing hydrogen content inside the cavities by the total hydrogen content of the cast sample). Finally, these findings confirm the conclusions made earlier based on the permeation tests that indicate that the porosity is a trap for hydrogen and that most of the absorbed hydrogen is in the cavities.

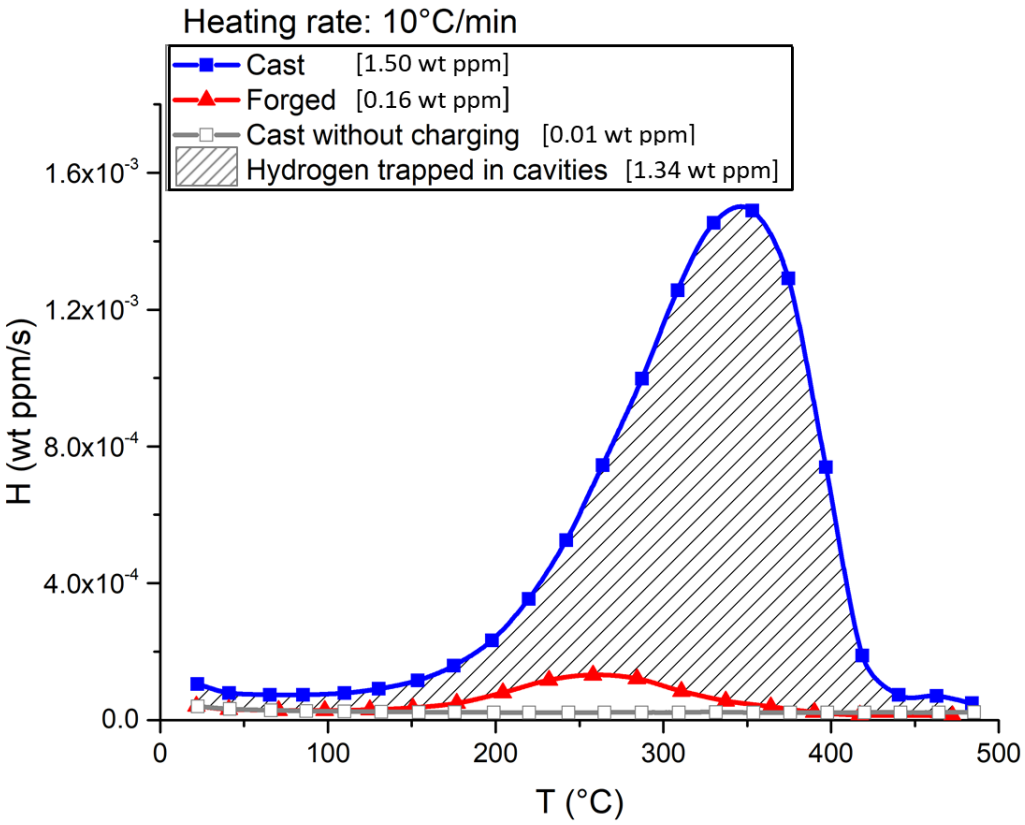

Figure 50: TDS spectra for a cast sample without charging, a charged cast sample and a charged forged sample. The charging was performed in a 5 wt% NH_4SCN aqueous solution for 24 h charging. The heating rate was 10°C/min. The cast sample has a volume fraction of porosity of 0.27%.

A comment is due here on the state of hydrogen present in cavities. Based on the results of Figure 50, 1.34 wt ppm of hydrogen, obtained by subtracting the concentrations measured in the cast and forged specimens respectively, was trapped in the cavities. Considering the mass of the specimen used (4.3 g), this corresponds to 5.8×10^{-6} moles of H atoms. It can be questioned whether this hydrogen is under the molecular form (gas) and/or under the atomic form adsorbed on the internal surfaces of the cavities. Assuming that the cavities are spherical and they have a diameter of 7.6 µm (based on the X-ray tomography results presented earlier in Table 2), we need 6.38×10^{6} cavities in order to achieve the volume fraction of porosity for this sample, which is 0.27%. This represents an internal surface area of 1.16×10^{-3} m². In order to estimate the amount of hydrogen than can be adsorbed on such an area, a hydrogen adsorption site density of 2.85×10^{-5} mol/m² will be considered, which corresponds to that of a (110) surface plane of iron [127]. If all the adsorption sites of the internal surfaces of cavities were occupied, the maximum amount of adsorbed hydrogen would be 3.3×10^{-8} moles. This is inferior to 1% of the total amount of trapped hydrogen in the cavities (5.8×10^{-6} moles). Consequently, this calculation, based on experimental data, demonstrates that the hydrogen is mainly under the gaseous form in this case. In a general way, for a given porosity fraction, the distribution of hydrogen between the adsorbed and gaseous states depends on the size of cavities and the pressure inside them. This point was discussed in the first chapter based on the work of Wong [71] (see Figure 9).

To sum up, these measurements permitted to identify the contribution of the porosity in the hydrogen trapping process. It indicates that the porosity acts as trap for hydrogen in which a large amount of hydrogen can be stored. In addition, in our case, this hydrogen is mostly under the molecular form. However, the question that remains is whether the porosity is a reversible or irreversible trap at room temperature. A more detailed discussion is presented in the next section.

III.2.3.5 Hydrogen desorption at room temperature

Figure 51 (a) summaries TDS measurements that were performed on the same charged cast sample after different times spent at room temperature. The same sample, with a porosity volume fraction of 0.13%, was charged five times under the same conditions (in a 5 wt% NH_4SCN solution at 50°C). After each charging operation, it was stored at room temperature for a certain period before starting the TDS measurement. The analyses were

done after 75 minutes, 6 h, 24 h, 3 days and 7 days. The corresponding amounts of hydrogen extracted from the TDS data are respectively: 1.01 wt ppm, 0.74 wt ppm, 0.42 wt ppm, 0.16 wt ppm and 0.02 wt ppm. The first value represents the hydrogen content 75 minutes after the end of charging, 75 minutes being the minimum time necessary for preparing the specimen and pumping the TDS instrument. The other values represent the amount of hydrogen remaining in the sample after a certain time spent at room temperature. After seven days, TDS data did not show any hydrogen peak up to 500°C. This indicates that the absorbed hydrogen that was measured immediately after charging (red curve) was able to desorb completely from the sample at room temperature. Figure 51 (b) presents the simulated concentration profiles after different times of desorption at room temperature using the apparent diffusion coefficient determined by EP for the cast sample ($3.3x10^{-12}$ m²/s). Figure 51 (c) shows the evolution of the remaining hydrogen content as a function of the desorption time at room temperature. The blue dashed curve represents the result of a simulation using the apparent diffusion coefficient determined by EP for the cast sample ($3.3x10^{-12}$ m²/s), the cross marks correspond to the TDS measurements. The red dotted curve is the result of a simulation using an adjusted diffusion coefficient ($2.7x10^{-12}$ m²/s) in order to fit best to the experimental data. This adjusted diffusion coefficient is slightly lower than the apparent diffusion coefficient obtained by EP, which is expected because the porosity fraction of the TDS sample (0.13 ± 0.02%) is relatively higher than that of the EP sample (0.07± 0.02%). These data indicate that the hydrogen concentration decreases with increasing the desorption time until reaching almost zero after seven days. In conclusion, this absorbed hydrogen was able to quit the sample at room temperature and at the same time, it corresponds mainly to the hydrogen trapped in the cavities as demonstrated in the previous section. Therefore, the porosity can be considered as a reversible trap for hydrogen at room temperature. This conclusion is the same as that found using EP.

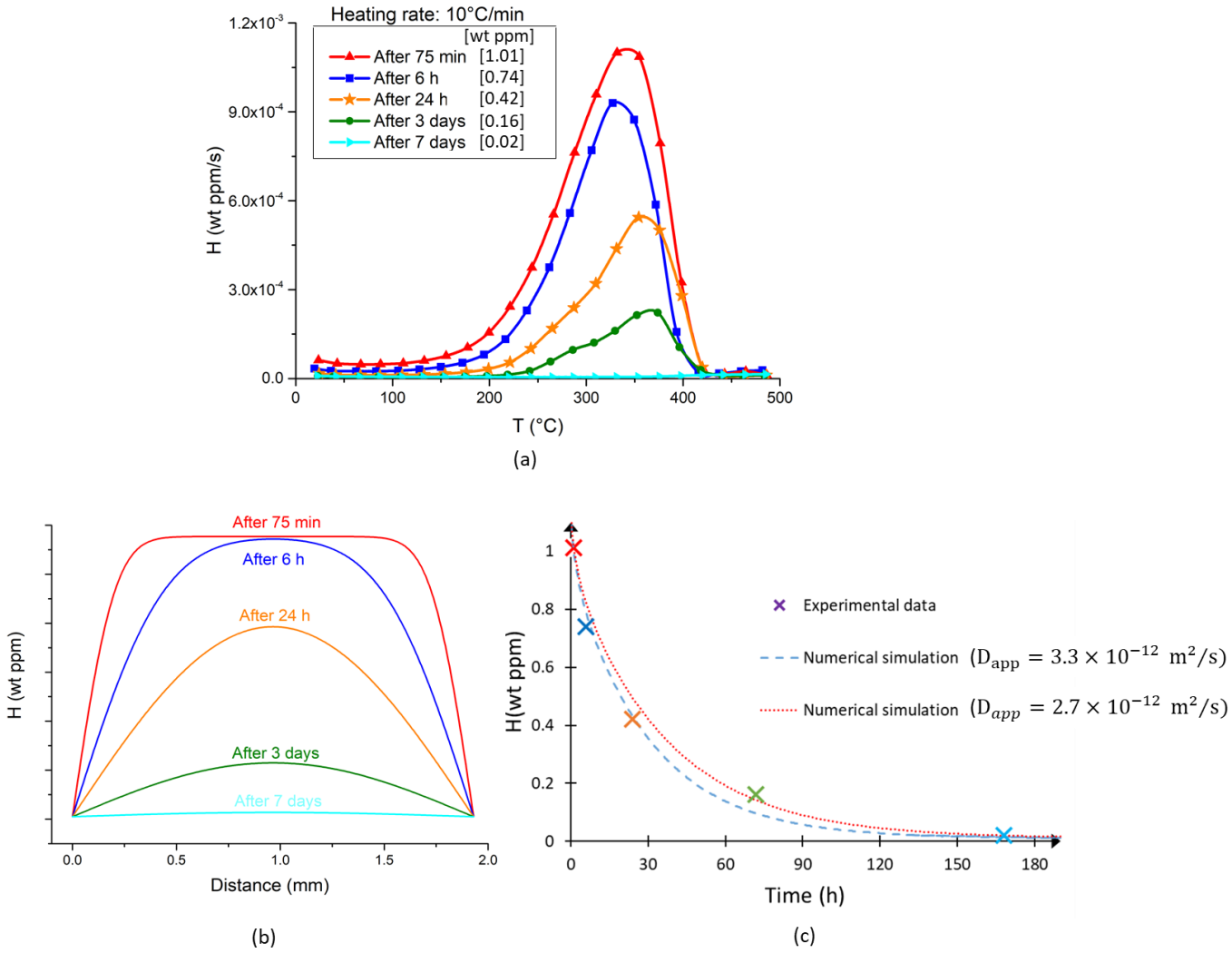

Figure 51: The effect of the desorption time at room temperature on the hydrogen content for a cast sample (a) TDS spectra after hydrogen charging followed by different times of desorption at room temperature; heating rate = 10°C/min. (b) The evolution of hydrogen concentration profile as a function of time at room temperature based on numerical simulations. (c) Hydrogen content evolution as a function of desorption time. The dashed curve corresponds to the numerical results. The points correspond to hydrogen contents determined from TDS peak integration. The same cast sample (volume fraction of porosity = 0.13%) was used for all the experiments. Charging was performed in a 5 wt% NH_4SCN aqueous solution for 24 h at 50°C.

III.2.3.6 Hydrogen content and porosity fraction

The aim of this section was to investigate the correlation between the amount of absorbed hydrogen and the volume fraction of porosity. Therefore, one forged sample and five cast samples were used. The cast samples were taken from different zones in the ingot in order to have different porosity fractions from one sample to another. The samples were charged for 24 h in a 5 wt% NH_4SCN solution heated at 50°C. Then, TDS measurements were performed with the same heating rate as the previous measurements (10°C/min). Figure 52 (a) shows hydrogen thermal desorption spectrum for each sample. The desorption peak

maximum is around 350°C for the five cast samples and around 230°C for the forged sample. As can be seen, the hydrogen content is different from one sample to another, especially between the forged sample and the cast samples. The amount of absorbed hydrogen increases linearly with increasing porosity fraction as illustrated in Figure 52 (b). This proves, as can be expected, that a higher volume fraction of porosity leads to a larger hydrogen uptake. In fact, if we charged different cast samples in the same conditions, cavities in all the samples should reach the same pressure at equilibrium and a linear relation between porosity fraction and hydrogen content is expected.

It should be mentioned that the hydrogen concentrations presented in Figure 52 include gaseous hydrogen in the cavities, as well as hydrogen “dissolved” in the metal, the latter being about 0.16 wt ppm as measured on the forged specimen. More precisely, this “dissolved” hydrogen most probably corresponds to hydrogen shallowly trapped in the microstructure.

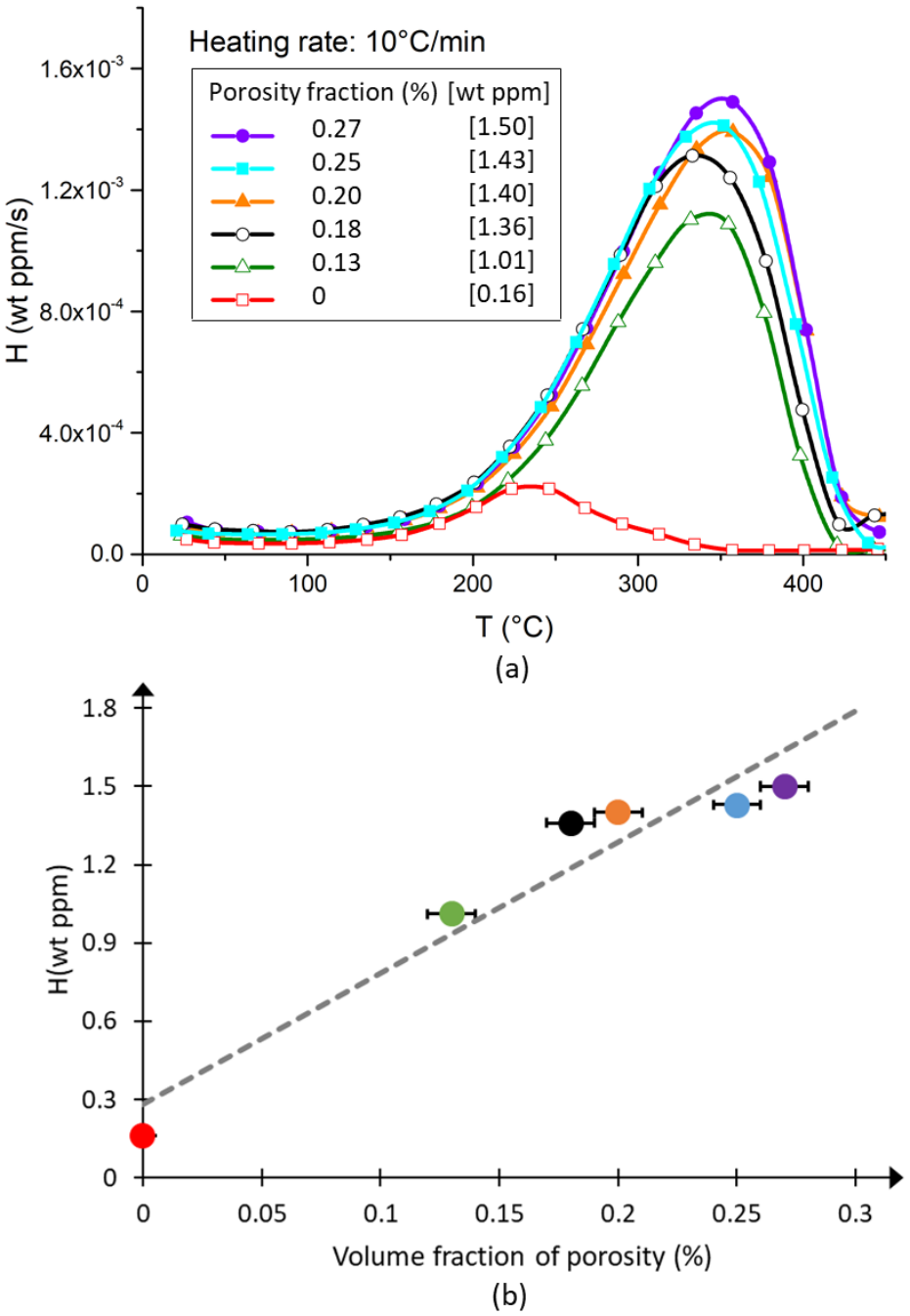

Figure 52: The relationship between the amount of absorbed hydrogen and the volume fraction of porosity (a) TDS spectra; heating rate = 10°C/min (b) The evolution of hydrogen content as a function of the volume fraction of porosity. The hydrogen content was determined from TDS peak integration. All samples were charged in a 5 wt% NH_4SCN aqueous solution for 24 h. The error bars represent an uncertainty of 0.02% for the volume fraction of porosity.

III.2.3.7 Determination of hydrogen fugacity and solubility

In the following, a method is proposed to determine hydrogen fugacity and hydrogen solubility (Sieverts constant) in the studied material.

Table 6 shows the hydrogen concentration measured using TDS in five cast specimens with different porosity fractions. A correction factor of 1.16 was applied to take account of the hydrogen loss during the period between the end of charging and the beginning of the TDS measurement (approximatively 75 minutes). This correction factor was obtained using numerical simulation of hydrogen desorption at room temperature (with D_{app} = 3.3x10^{-12} m²/s) for 75 minutes. For each specimen, the concentration of hydrogen inside the cavities can be easily obtained from the difference between the total hydrogen concentration and the concentration of hydrogen dissolved in the metal, that is known from the TDS measurement conducted on the forged material containing no porosity (it is equal to 0.2 wt ppm after correction using a D_{app} = 7.8x10^{-12} m²/s for the numerical simulation of desorption at room temperature for 75 minutes).

Knowing the void volume and the hydrogen amount inside the cavities for each sample, the pressure can be calculated using Eq.(21). This expression is based on Abel-Noble equation of state (Eq.(14)).

$$P = \frac{n_c RT}{2(V - n_c b)} \tag{21}$$

with P is the pressure (Pa), n_c represents the amount of atomic hydrogen inside the cavities (mol), R is the universal gas constant (8.31477 J.mol^{-1} K^{-1}), T is the temperature (K), V is the void volume (m^3) and b is a constant (1.4598x10^{-5} m^3/mol [64]). The fugacity was then evaluated using Eq.(22) [29], which represents the relationship between the fugacity and the pressure for an Abel-Noble gas. The hydrogen pressure and fugacity obtained in the different specimens are shown in Table 6.

$$f = P \exp\left(\frac{Pb}{RT}\right) \tag{22}$$

Table 6: Hydrogen contents, hydrogen pressure and fugacity in the cavities calculated from Abel-Noble equations for five cast samples with different volume fractions of porosity.

Volume fraction of porosity (%)	0.13	0.18	0.20	0.25	0.27
Hydrogen content (wt ppm)	1.01	1.36	1.40	1.43	1.50
Hydrogen content after correction (wt ppm)	1.18	1.57	1.62	1.66	1.74
Pressure (bar)	83	84	78	64	62
Fugacity (bar)	87	88	82	66	65

Figure 53 shows the fugacity obtained in the five different samples as a function of the volume fraction of porosity. For the three specimens with a porosity fraction not higher than 0.2%, similar values of hydrogen fugacity are obtained (85 ± 3 bar). On the other hand, fugacities measured for the two specimens with the highest porosity fractions are significantly lower (65-66 bar). However, as the samples were all charged in the same conditions, hydrogen fugacity should be the same at equilibrium. This decrease in fugacity for the highest porosity fractions can be associated to the non-equilibrium state of the hydrogen inside the samples. It is clear that the samples with a higher void volume need more hydrogen to reach the same pressure (fugacity) as the samples with smaller void volume. Consequently, the charging time, for the samples with higher void volume, should be superior to the others in order to reach equilibrium. The charging time used in this study (24 h) was apparently not long enough for the specimens with the highest porosity fractions. On this basis, we will keep the fugacity value of 85 ± 3 bar obtained using only the three specimens with the lowest porosity fractions. This fugacity can also be considered as the equivalent hydrogen fugacity of the charging environment (5 wt % NH_4SCN aqueous solution at 50°C).

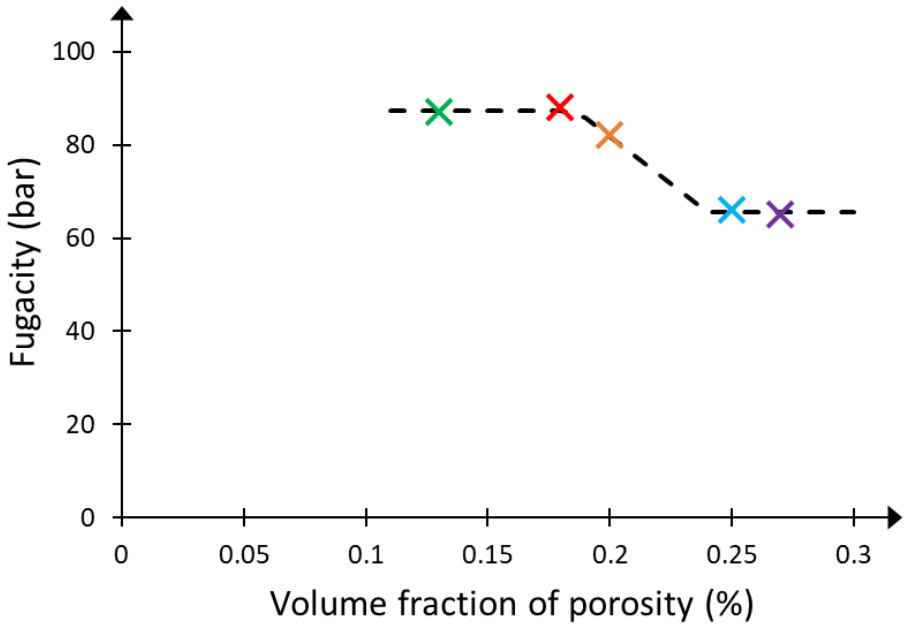

Figure 53: The plot of hydrogen fugacity as a function of the volume fraction of porosity. The fugacity values were calculated based on the equation of Abel-Noble.

The equilibrium between hydrogen dissolved in the metal and gaseous hydrogen in the cavities can be described by the Sieverts' law [128] as explained previously. The expression is reminded in Eq.(23).

$$C = K_H \sqrt{f_{H_2}} \tag{23}$$

where C represents the concentration of atomic hydrogen dissolved in the material, K_H is the Sieverts constant (hydrogen solubility) and f_{H_2} is the fugacity of gaseous hydrogen in cavities. The Sieverts' law can be obtained by equating the chemical potential of hydrogen dissolved in the metal and that of the gaseous hydrogen in cavities. As shown in Appendix, it is possible to include in C term, not only interstitial hydrogen, but also trapped hydrogen, provided that the trap occupancy is low. It is assumed here that this C term in Eq.(23) corresponds to the hydrogen concentration measured using TDS in the forged specimen (0.2 wt ppm after correction). As the hydrogen fugacity is known from the analysis shown previously (85 bar), the Sieverts constant of the steel can be determined from Eq.(23). It should be mentioned that this value applies at 50°C, which is the hydrogen charging temperature chosen in this study. The value obtained (Eq.(24)) is in good agreement with that obtained by Sezgin et al. on a similar material [63].

$$K_H = (2.2 \pm 0.6) \times 10^{-2} \times 10^{-2} \text{ wt ppm. bar}^{-1/2} = 0.180 \pm 0.045 \text{ mol. m}^{-3}\text{. bar}^{-1/2} \quad (24)$$

III.3 Conclusions

In this work, the influence of porosity in the hydrogen diffusion and trapping processes has been studied for a low-alloy cast steel by means of electrochemical permeation and thermal desorption spectroscopy. Material characterization showed that the only difference between the forged material and the cast material lies in the porosity. The hydrogen was chemically introduced in thermal desorption spectrometry samples using a NH_4SCN aqueous solution heated at 50°C.

In summary, the most significant findings of this study are:

- Electrochemical permeation experiments showed that hydrogen diffusion in the cast samples was slower than in the forged sample. This is due to the porosity, which acts as trap sites that delay hydrogen diffusion.
- The comparison of the decay transients between the forged and the cast samples showed a significant effect of porosity in the trapping process: the majority of hydrogen (over 85% of the total desorbed hydrogen) was located in cavities. The same conclusion was found based on thermal desorption spectrometry results.
- Hydrogen in cavities was in the gaseous form. Hydrogen adsorbed on internal surfaces of cavities was shown negligible.
- Electrochemical permeation and thermal desorption spectrometry experiments have clearly shown that the hydrogen trapped in cavities desorbed spontaneously at room temperature, over some tens of hours for thicknesses of about two millimeters. This proves that the porosity acts as reversible traps for hydrogen at room temperature.
- Thermal desorption spectrometry measurements, performed on samples with different volume fraction of porosity, indicated that hydrogen concentration increased linearly with the increase of the volume fraction of porosity.
- A method was proposed to determine hydrogen fugacity and solubility (Sieverts' constant of the steel) from thermal desorption spectrometry data. In the hydrogen

charging conditions used before thermal desorption spectrometry, the hydrogen fugacity and solubility were estimated to 85 bar and 2.2×10^{-2} wt ppm.$bar^{-1/2}$, respectively.

Chapter 4: Modelling of hydrogen diffusion in a steel containing porosities

IV.1 Introduction

In the previous chapter, experimental data showed that the porosity acts as a reversible trap for hydrogen and as a result, it reduces hydrogen diffusivity. This latter conclusion was made based on the comparison between the electrochemical permeation results of the forged and the cast samples. The aim in this chapter is to develop a numerical model for hydrogen diffusion in a steel containing porosity. Two numerical models have been developed based on two different approaches to take into account the trapping of gaseous hydrogen in porosity. The first model is a 3D finite element model based on a non-equilibrium approach and the second is a 1D model based on a local equilibrium approach. These two models are used in order to simulate hydrogen permeation transients. The gaseous hydrogen behavior inside the porosities is described using the NIST EOS (Eq.(15)) and the pressure-fugacity relationship (Eq.(3)) as presented in the first chapter. The use of such equations permits to cover wide range of pressure (up to 2000 MPa) in contrast to ideal gas or Abel-Noble equations where the pressure range is limited.

In the current chapter, a full description of the two models is given. For the non-equilibrium model, a hydrogen reaction flux at the bulk-cavity interface is defined first and then a detailed study based on a simulation with one cavity is performed. This study is very useful to highlight the role of porosity and to understand the evolution of several parameters such as hydrogen pressure and hydrogen concentration during the permeation test. After that, the effect of the number of cavities on the hydrogen permeation behavior is discussed. In addition, the simulations results of the non-equilibrium model are compared to that of the local equilibrium model. Afterwards, a parametric study is conducted using the local equilibrium model to explore the effect of various parameters such as hydrogen fugacity and porosity fraction on the hydrogen diffusion behavior. Then the results are compared to the permeation experimental data presented in the previous chapter. Finally, it should be mentioned that the mechanical effect of hydrogen pressure inside the cavity was not discussed in this study; the focus was only set on the diffusion and the trapping of hydrogen.

IV.2 Non-equilibrium model

In order to simulate hydrogen permeation tests through a cast steel membrane, the FEM (Finite Element Method) approach was used. The simulations were performed on a 3D geometry as presented in Figure 54 (a) where one of the simulation boxes used in this work is shown. It represents a steel specimen with one cavity placed in the center. Figure 54 (b) shows a cross-section view. The boundary conditions associated with this model are detailed as follows: on the right side of the box a zero concentration was imposed, which corresponds to the detection side. On the opposite side (i.e. the left side) a constant fugacity was imposed. This side corresponds to the charging side in the permeation test. Finally, a periodic boundary condition consisting of a zero hydrogen flux was imposed along the lateral sides.

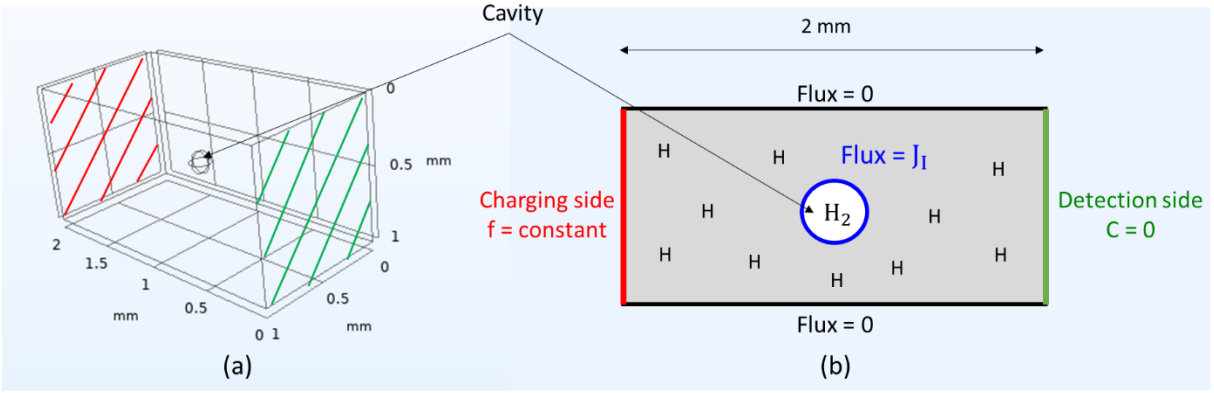

Figure 54: Simulation box containing one cavity in the center (a) in 3D and (b) cross-section view with the boundary conditions.

At the bulk-cavity interface atomic hydrogen can recombine into molecular hydrogen according to the following chemical reaction

$$2\mathrm{H} \leftrightarrow \mathrm{H}_2 \tag{25}$$

The key of this model lies in defining the hydrogen flux at the bulk-cavity interface. In our case, it is possible to define this flux using the expression given in Eq.(26). which was developed by Pekar [129]. It represents a general expression of the flux (reaction rate) of a chemical reaction between two components A and B based on a non-equilibrium thermodynamics approach:

$$\mathrm{J} = k_1 \times \exp\left(-\frac{\mu_\mathrm{A}^0}{\mathrm{RT}}\right) \times \left[\exp\left(\frac{\mu_\mathrm{A}}{\mathrm{RT}}\right) - \exp\left(\frac{\mu_\mathrm{B}}{\mathrm{RT}}\right)\right] \tag{26}$$

where J represents the reaction flux, k_1 is a kinetic factor, μ_A and μ_B are the chemical potential of component A and B respectively and μ_A^0 is the standard chemical potential of the component A. In order to use this expression, we must first calculate the chemical potentials of hydrogen in the system. In our case, the chemical potential of atomic hydrogen at the bulk-cavity interface can be expressed as follows:

$$\mu_H^{bulk} = \mu_H^0 + RT \ln\left(\frac{C_I}{C^0}\right) \tag{27}$$

where μ_H^0 is the standard chemical potential, C_I is the H concentration at the interface and C^0 is the H concentration in the standard state. In the same way, it possible to define the chemical potential of the molecular hydrogen inside the cavity

$$\mu_{H_2} = \mu_{H_2}^0 + RT \ln\left(\frac{f_{H_2}}{f_{H_2}^0}\right) \tag{28}$$

where $\mu_{H_2}^0$ is the standard chemical potential of molecular hydrogen, f_{H2} represents the hydrogen fugacity inside the cavity and $f_{H_2}^0$ is the hydrogen fugacity in the standard state. Since the chemical potential of the atomic hydrogen inside the cavity is equal to the half of the chemical potential of the molecular hydrogen ($\mu_H^{cavity} = \frac{1}{2}\mu_{H_2}$), we can express the chemical potential of atomic hydrogen inside the cavity as:

$$\mu_H^{cavity} = \frac{1}{2}\mu_{H_2}^0 + RT \ln \sqrt{\frac{f_{H_2}}{f_{H_2}^0}} \tag{29}$$

Now, in order to define the hydrogen flux at the bulk-cavity interface, we use Eq.(26) and we substitute μ_A by μ_H^{bulk} (Eq.(27)), and μ_B by μ_H^{cavity} (Eq.(29)). Consequently, the flux at the interface can be expressed as

$$J_I = k_1 \times \exp\left(\frac{\frac{1}{2}\mu_{H_2}^0 - \mu_H^0}{RT}\right) \times \left[\exp\left(\frac{\mu_H^0 - \frac{1}{2}\mu_{H_2}^0}{RT}\right) \times \frac{C_I}{C_0} - \sqrt{\frac{f_{H_2}}{f_{H_2}^0}}\right] \tag{30}$$

$$= k_1 \left[\frac{C_I}{C_0} - \exp\left(\frac{\frac{1}{2}\mu_{H_2}^0 - \mu_H^0}{RT}\right) \times \sqrt{\frac{f_{H_2}}{f_{H_2}^0}}\right]$$

The final expression can be written in the form

$$J_I = Q \times \left[C_I - K_H \times \sqrt{f_{H_2}}\right] \quad (31)$$

where K_H represents the hydrogen solubility as explained earlier with $K_H = \frac{C^0}{\sqrt{f^0_{H_2}}} \times \exp\left(\frac{\frac{1}{2}\mu^0_{H_2} - \mu^0_H}{RT}\right)$ and $Q = k_1/C_0$. In Eq.(31), the term in brackets is a concentration (mol/m^3) and Q is a speed (m/s). From the expression above, it can be understood that the orientation of the hydrogen flux at the bulk-cavity interface (inward or outward) depends on the hydrogen concentration at the interface and the hydrogen fugacity inside the cavity. If the chemical potential of the hydrogen at the interface is higher than the chemical potential inside the cavity (i.e. $C_I > K_H \times \sqrt{f_{H_2}}$), hydrogen from the bulk will enter the cavity and recombine into molecular hydrogen. In the opposite case ($C_I < K_H \times \sqrt{f_{H_2}}$), hydrogen will quit the cavity and diffuse to the bulk. Finally, at equilibrium ($C_I = K_H \times \sqrt{f_{H_2}}$), the flux is equal to zero. This expression assumes that the porosity act as a reversible trap, i.e. that hydrogen can quit without providing any additional energy from outside the system. This assumption is justified by the experimental data presented in the previous chapter.

Figure 55 shows the flowchart of the FEM calculations, conducted using Comsol software. It explains the working mechanism of this model. First, the module of transport of diluted species provided by Comsol was used to handle the process of hydrogen diffusion in the bulk. This module permits to study the mass transport phenomenon of the chemical species due to diffusion (our case) and/or due to a flow field or an electric field [130]. In our case, we just used the classical diffusion governed by Fick's law:

$$\frac{\partial C_B}{\partial t} = \nabla(D \nabla C_B) \quad (32)$$

where C_B is the bulk hydrogen concentration, t represents the time and D is the bulk hydrogen diffusion coefficient. This coefficient was considered equal to the apparent diffusion coefficient determined in the previous chapter from permeation experiments for the forged material, i.e. the material containing no porosity. Then, the amount of the molecular hydrogen inside the cavity (number of moles n) was calculated in two steps. First, we calculate the integral of the flux J_I over the time and then we calculate the spatial integral of the first

integration along the cavity surfaces (S) as illustrated in Eq.(33). The temporal integration was done by adding an Ordinary Differential Equation (of type $a\frac{\partial^2 y}{\partial t^2} + b\frac{\partial y}{\partial t} = J_I$, with a = 0 and b = 1) to the model. On the other hand, the spatial integral was evaluated by adding "a component coupling operator" of type integration to the numerical model provided by Comsol software. This feature permits to evaluate the space integral of a variable during the calculation. Finally, it should be mentioned that the ½ factor in Eq.(33) is a stoichiometric coefficient issued from the chemical reaction in Eq.(25).

$$n = \frac{1}{2}\int_S \int_t J_I \, dt \, dS \tag{33}$$

Once the amount of the molecular hydrogen inside the cavity is determined, it is possible now to calculate the pressure inside the cavity by using the expression presented in Eq.(34). This expression represents one of the two zeros of Eq.(15). Note that only this solution is accepted because the other one is negative.

$$P = \frac{(b^0 - v) + \sqrt{(b^0 - v)^2 + 7.82 \times 10^{-15}\, RT}}{3.91 \times 10^{-15}} \tag{34}$$

The next step in the calculations is to determine the hydrogen fugacity inside the cavity because it is necessary in order to calculate the new flux at the bulk-cavity interface. Therefore, the integral of Eq.(3) was evaluated after substituting the molar volume (v) by the expression of the molar volume from the EOS described earlier (see Eq.(15)). We obtained the following expression of fugacity, which is a simple function of the pressure when the temperature is constant:

$$f = P \times \exp\left(\frac{Pb^0 - 9.775 \times 10^{-16}\, P^2}{RT}\right) \tag{35}$$

Finally, the new hydrogen flux at the bulk-cavity interface can be calculated using Eq.(31). The simulation ends when the simulation time reaches the final time fixed by the user.

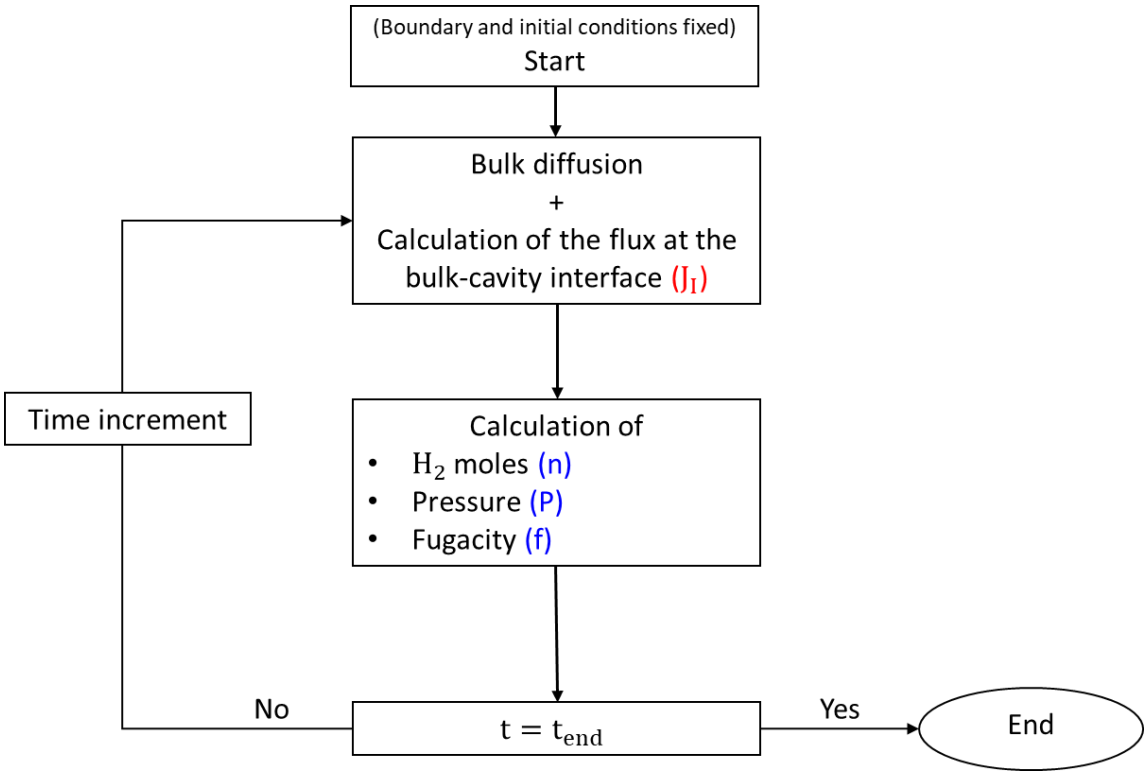

Figure 55: The flowchart of the simulation procedure used in the non-equilibrium model.

In this study, hydrogen permeation simulations were performed on 3D geometries. One of the simulation boxes is presented in Figure 56 (a). It was meshed by tetrahedral elements generated automatically by Comsol software. In order to verify the convergence of the numerical results, the hydrogen permeation flux is plotted as a function of the mesh size in Figure 56 (b). The elements size and the total number of elements are also presented in the same figure which shows that no effect of the mesh size is observed. Furthermore, other simulations were performed by varying the cavity radius (from 4 µm to 100 µm) and no significant effect was noticed either. Finally, it should be mentioned that we opted for a “Fine” mesh and that the numerical simulations were performed using a computing cluster in order to reduce the calculation time.

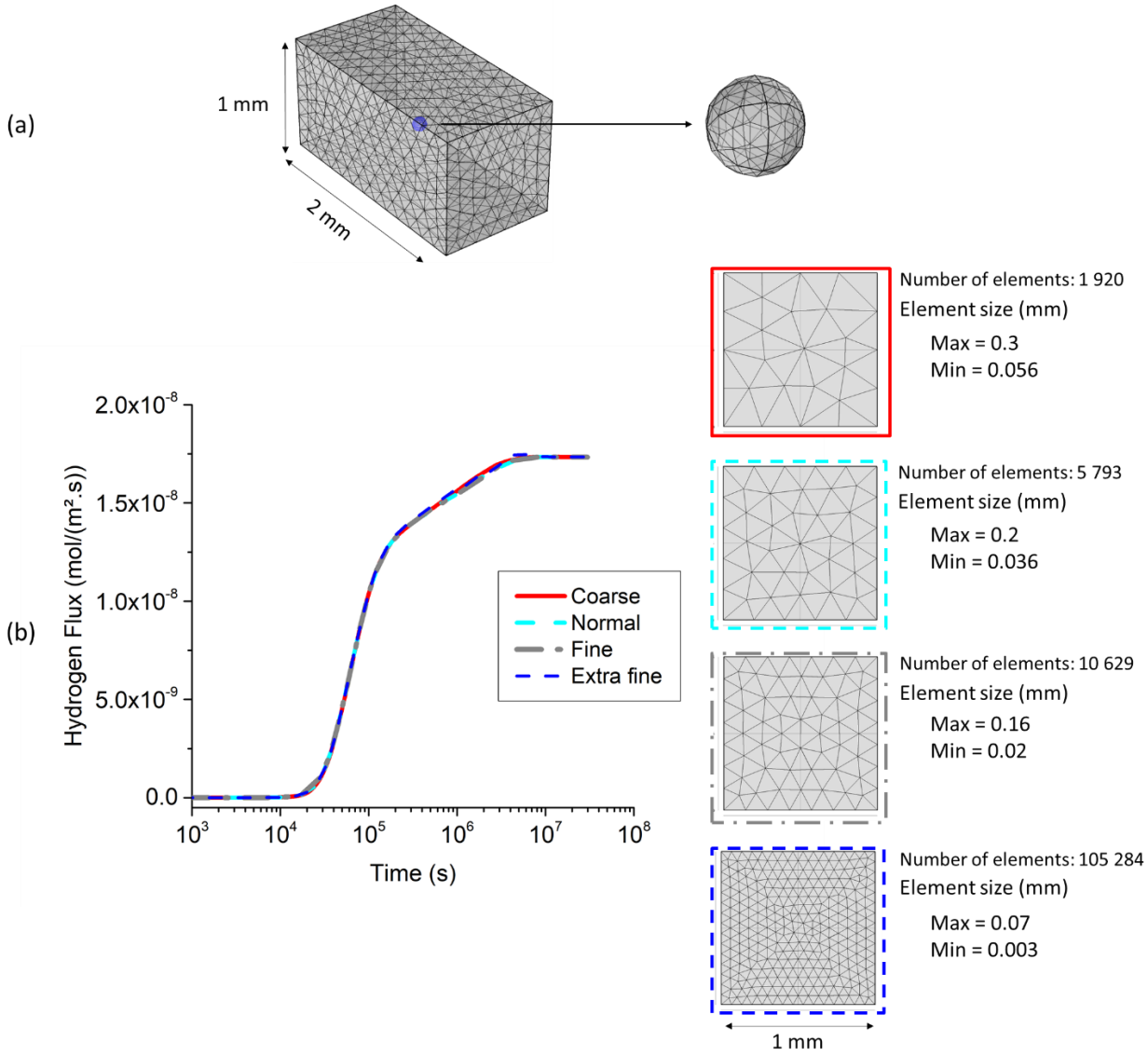

Figure 56: (a) Example of a simulation box used in this study. The sphere represents the cavity. (b) Comparison between the permeation curves obtained using different mesh sizes.

IV.3 Equilibrium model

A simpler 1D model based on an equilibrium hypothesis was developed in order to simulate permeation tests in shorter computation times. Figure 57 shows a schematic representation of the simulation box used in this work. The sample was split along the thickness into n equivalent elements. This model relies on the following assumptions. First, the porosity fraction in each element is the same and it is equal to the porosity fraction of the sample. Second, in each element, the bulk hydrogen concentration is constantly in equilibrium with the hydrogen fugacity trapped in the cavities as described by Sieverts' law. Third, this equilibrium is instantly established and finally only bulk hydrogen is able to diffuse from one

element to another. Note that the total hydrogen concentration (C_{Total}) in each element is the sum of bulk hydrogen concentration (C_B) and hydrogen concentration in the porosity (C_P) as expressed in Eq.(36). The boundary conditions are presented in Figure 57. The first element corresponds to the charging side where the fugacity inside the porosity is equal to the fugacity of the charging medium and the bulk concentration is deduced from Sieverts' law Eq.(4). The last element represents the detection side where the concentration was set to zero. These boundary conditions were maintained during the whole simulation. In addition, the initial hydrogen concentration was set to zero in elements 2 to n-1.

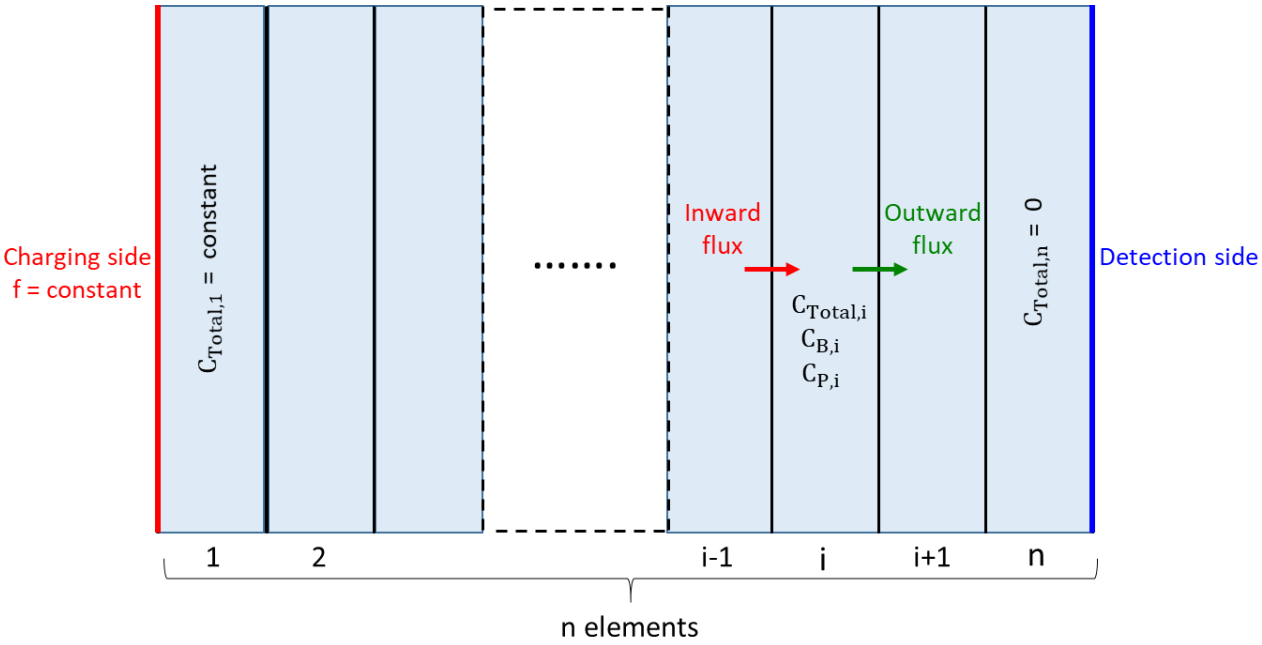

Figure 57: Schematic representation of the simulation box used in the equilibrium model.

$$C_{Total} = C_B + C_P \tag{36}$$

Figure 58 shows the flowchart of the calculations used in the simulations. It is composed mainly of two parts, the diffusion step and the re-equilibration step. For the first step, the hydrogen diffusion, in each element and at each time step, was calculated using Fick's law:

$$\frac{\partial C_{Total}}{\partial t} = D\frac{\partial^2 C_B}{\partial x^2} \tag{37}$$

where C_{total} represents the total hydrogen concentration, D is the bulk diffusion coefficient and C_B corresponds to the concentration of the hydrogen in the bulk. Notice that in the second term of the equation, it is written C_B instead of C_{Total}; this is because, as mentioned earlier, only bulk hydrogen (C_B) is able to diffuse.

Once the new C_{Total} at (t+Δt) was calculated, the re-equilibration step is then used to calculate the new C_B at (t+Δt) to ensure equilibrium between the bulk hydrogen and the hydrogen trapped in the cavities. This step is also necessary to avoid creating hydrogen and consequently ensure mass conservation in the system. In order to calculate the new C_B, one has to resolve a system of equations composed of Eq.(3), (4), (15) and (36). It appeared that numerical solving of that system of equations was very time consuming. In addition, multiple zeros were obtained and the zero selection process was not easy to automate. For these reasons, we have opted for a pre-calculated table of solutions which is composed of C_{Total} and the corresponding C_B and C_P for a given porosity fraction. In fact, at equilibrium there is only one possible value of C_B for a given C_P. This table was created by fixing a pressure first which permits to calculate at the same time C_P and hydrogen fugacity using Eq.(15) and Eq.(3), respectively. Then, the hydrogen fugacity was used to deduce C_B using Eq.(4) and finally, C_{Total} can be obtained by Eq.(36). The values of the total concentration (C_{Total}) inserted in the table before the simulation starts, are chosen by the user and they cover the range of concentrations needed for running the simulation from 0 to C_{Total} at the entry side. The values of C_B and C_P corresponding to a given total concentration are extracted from the table of solutions using linear interpolation.

It should be mentioned that the exit permeation flux corresponds to the flux calculated at the interface of the (n-1) element and the (n) element. All the simulations based on the equilibrium model were performed using Matlab software. Finally, it is may be useful to mention that the diffusion equation (Eq.(37)) was solved by using the function ode15s provided by Matlab.

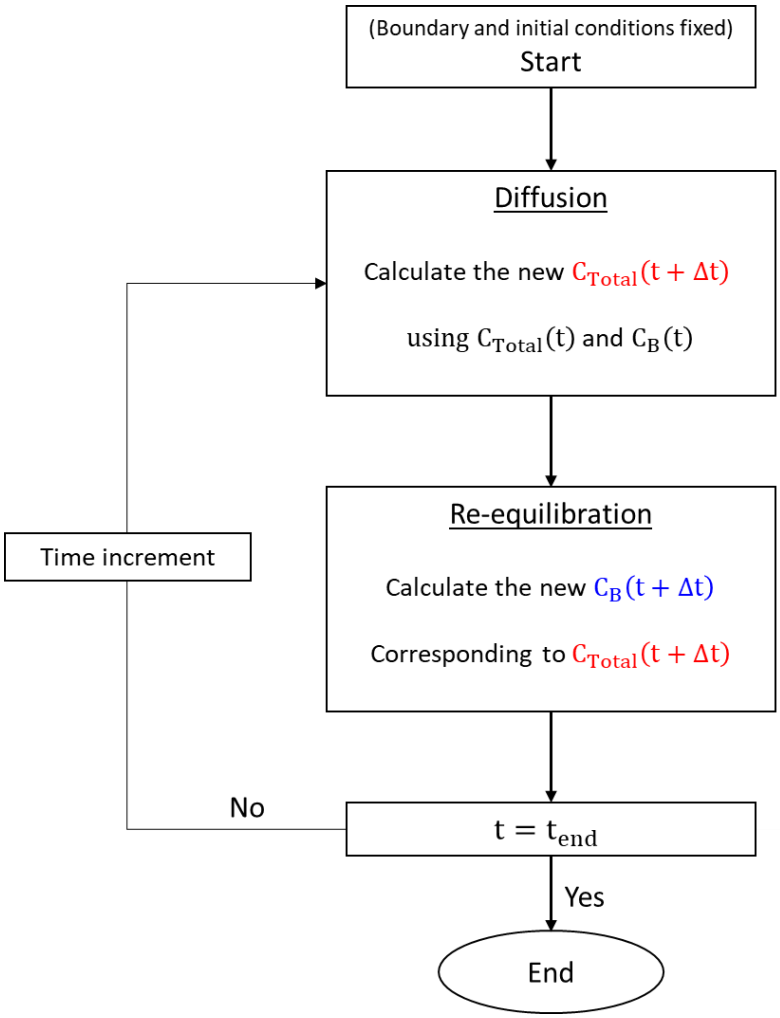

Figure 58: The flowchart of the simulation procedure used in the equilibrium model.

IV.4 Results and discussion

The input parameters used in the numerical simulations conducted using the two models are presented in table 1. It is important to mention that the value of the fugacity was estimated using the work of Venezuela [121], which gives a relationship between hydrogen fugacity and the electrochemical over-potential for a 3.5NiCrMoV steel charged in a 0.1 M NaOH aqueous solution. In our electrochemical permeation tests, presented in the previous chapter, the over-potential was equal to -1.1 V, which corresponds to a fugacity of 600 atm. Furthermore, the hydrogen diffusion coefficient used in the simulations is the apparent diffusion coefficient of the forged sample calculated using the time-lag method based on the electrochemical permeation results (see the previous chapter for more details). The solubility coefficients are also taken from the previous chapter and from literature as stated in Table 7. It should also be mentioned that for the non-equilibrium model it was

necessary to define a certain concentration in the bulk and a certain pressure inside the cavities in the initial state in order to avoid numerical problems. It is shown later that the values are very low and do not affect the simulation results.

Table 7: List of the parameters used in the numerical simulations.

Parameter	Values
Solubility (mol/(m^3 x $bar^{0.5}$) in the range of	[7.8×10^{-3} [63]- 0.225 [(1)]]
Hydrogen fugacity of the charging medium (bar)	600 atm
Bulk diffusion coefficient of hydrogen (m^2/s)	7.8×10^{-12} [(1)]
Initial bulk H concentration (mol/m^3)	0.01 [(2)]
Initial cavity pressure (MPa)	0.1 [(2)]
Membrane thickness (mm)	2
Temperature (°C)	20
Porosity volume fraction (%)	0.02 - 0.4

IV.4.1 Non-equilibrium model

IV.4.1.1 Effect of the kinetic factor

The aim of the first simulations was to understand the effect of the kinetic factor Q on the permeation behavior. This factor affects directly the flux of the hydrogen at the bulk-cavity interface. Physically, it affects the reaction rate of the recombination of atomic hydrogen into molecular hydrogen. Figure 59 (a) summarizes five different simulations performed under the same conditions as described before. The same simulation box was used in all the simulations (see Figure 54). The porosity fraction represents 0.04% (cavity radius is equal to 78 µm) and the solubility coefficient is 0.18 mol/(m^3×$bar^{0.5}$). Each simulation was performed with a different value of Q. As it can be seen, all hydrogen fluxes start to rise at the same moment (≈ 2×10^4 s) and have the same behavior until ≈ 7×10^4 s. After 7×10^4 s, the flux obtained using Q = 10^{-7} m/s increases slightly faster than the others but finally they all reach the same steady state. Figure 59 (b) shows the time evolution of the pressure inside the cavity. All the simulations show almost the same behavior except for the simulation with Q = 10^{-7} m/s.

[1] Value from the previous chapter
[2] Used only in the non-equilibrium model simulations

Actually, increasing Q tends to increase the hydrogen flux at the interface of the cavity-bulk and as a result, increases the amount of hydrogen entering the cavity (i.e. the pressure) quicker compared to a situation with a lower value of Q. In these cases ($Q \geq 10^{-6}$ m/s), the permeation behavior is being governed by the hydrogen diffusion and not the interface reaction. This means that all hydrogen atoms reaching the cavity are "instantly" recombined into molecular hydrogen. In this study, we have chosen to conduct the simulations in the regime where hydrogen diffusion is the limiting step. As a result, all the simulations presented later were performed with $Q = 10^{-4}$ m/s.

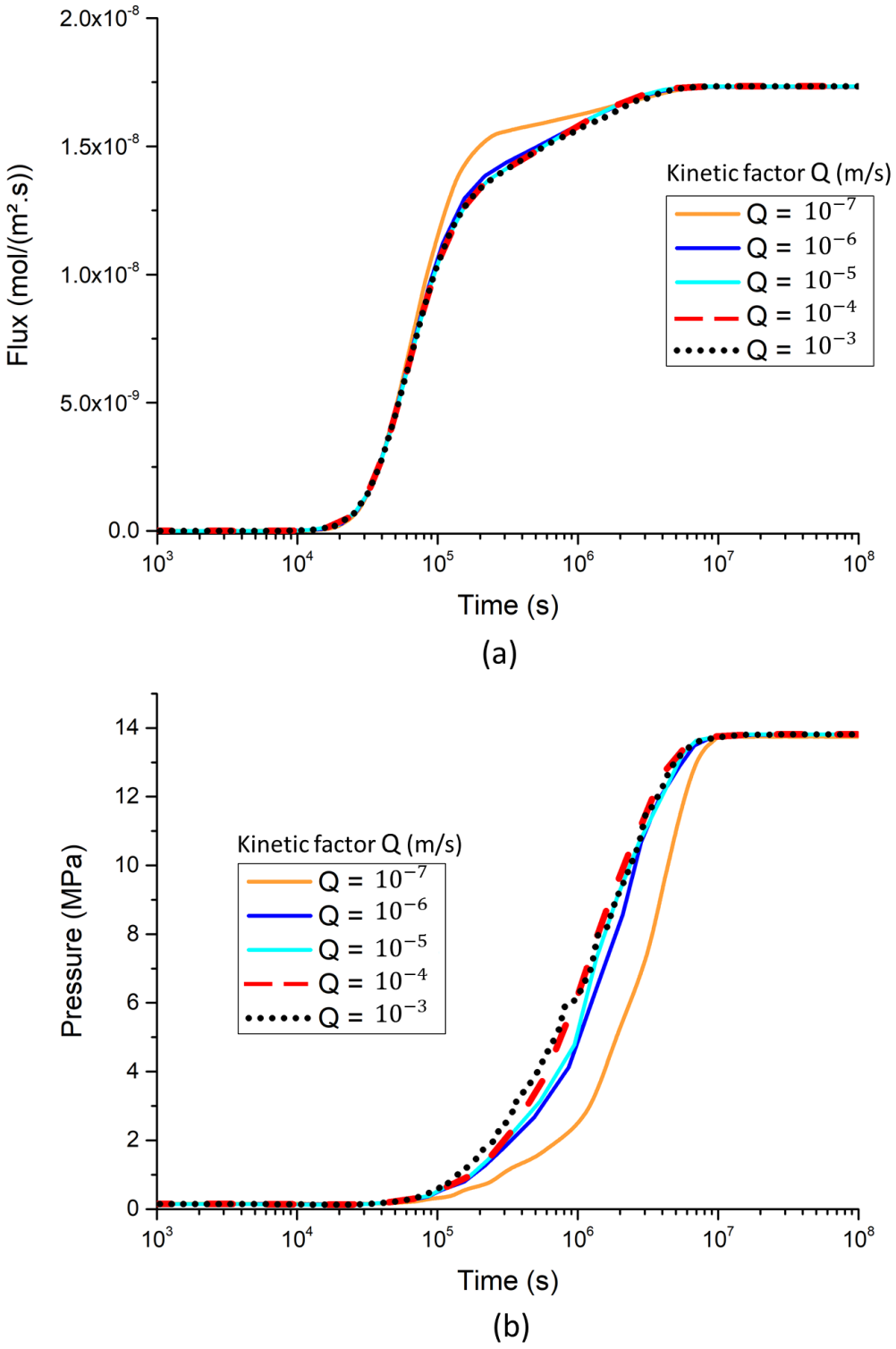

Figure 59: The influence of the kinetic factor Q on (a) the permeation flux and (b) the evolution in time of the pressure inside the cavity. All the simulations were performed under the same conditions. The simulation box contained one cavity placed in the center. Solubility coefficient: 0.18 mol/(m^3×bar$^{0.5}$). Porosity fraction: 0.04%. Simulations with Q ≥ 10^{-6} m/s provide similar fluxes and similar hydrogen pressures inside the cavity as well.

IV.4.1.2 Mass balance

Before going any further in the simulations, it is important first to verify that the mass balance is respected. For this reason, the amount of hydrogen in the simulation with $Q = 10^{-4}$ m/s was monitored during the whole simulation. Figure 60 presents the time evolution of the amount of hydrogen of the system. It shows that the hydrogen entering the system from the charging side (red curve) is equal to the sum of the hydrogen in the bulk, in the cavity and the hydrogen reaching the detection side (blue dashed curve). Consequently, it is safe to conclude that the mass balance is verified during the simulation.

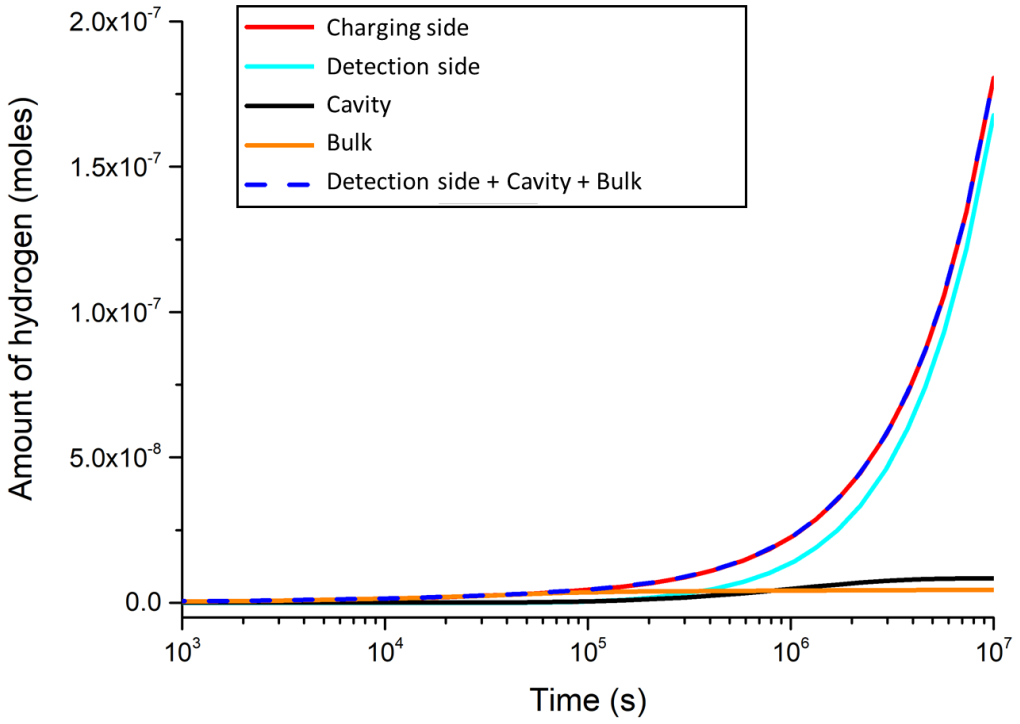

Figure 60: The distribution of hydrogen amount in the simulation box as a function of time for a simulation with one cavity and a kinetic factor $Q = 10^{-4}$ m/s. Solubility coefficient: 0.18 mol/(m^3×$bar^{0.5}$). Porosity fraction: 0.04%. At every instant, the amount of hydrogen that entered the system (red curve) is equal to the sum of the hydrogen in the cavity, in the bulk and the hydrogen that reached the detection side. The mass balance was respected during the whole simulation.

IV.4.1.3 One cavity case

Figure 61 (a) presents the simulation results of a permeation test for a sample without cavities (black curve) and a sample with one cavity (red curve). The cavity has a diameter of 156 µm (porosity fraction of 0.04%) and the solubility used in this simulation was equal to 0.18 mol/(m^3×$bar^{0.5}$). The initial and boundary conditions are identical in both cases. The

simulation box has a thickness of 2 mm as mentioned earlier. The fluxes of the two simulations started to rise at the same time (≈ 2×10^4 s) and they reach the same steady state. However, the 1 cavity simulation reaches the steady state later. Actually, the simulation with no cavities reaches the steady state approximately at 2.5×10^5 s whereas the 1 cavity simulation reaches it at 5.5×10^6 s. This difference is obviously related to the hydrogen-cavity interaction because the only difference between the two simulations lies in the presence of the cavity. In order to understand the root of this difference, a third simulation was performed. It is identical to the 1 cavity simulation except for the condition applied at the bulk-cavity interface. In this simulation (1 Cavity*), the hydrogen concentration at the bulk-cavity interface was set to zero through the whole simulation. The obtained result (blue dashed curve) is presented in the same figure (Figure 61 (a)) that contains the two previous results. The two simulations (1 cavity and 1 Cavity*) are identical until 1×10^5 s then, the 1 Cavity* simulation is plateauing at a low steady state flux, while the other continues to rise until reaching a higher steady state (the same steady state of the simulation with no cavities). In fact, the 1 cavity* flux, at the steady state, was smaller because hydrogen atoms that pass near the cavity are being constantly absorbed by the cavity. This is due to the zero concentration applied at the bulk-cavity interface. In contrast, the concentration at the interface for the 1 Cavity simulation increases with time until reaching the equilibrium concentration as presented in Figure 61 (b). At this point, no additional hydrogen can be trapped by the cavity and consequently, hydrogen continues to diffuse to the detection side. Actually, the increase of hydrogen concentration at the interface leads to reduce the concentration gradient at the interface and as a result decreases the hydrogen flux J_I entering the cavity. The temporal evolution of the pressure during the simulation is plotted in Figure 61 (c) on a logarithmic scale. The pressure (i.e. the amount of hydrogen) inside the cavity stays very low until 3×10^4 s and then, when hydrogen atoms reach the cavity the pressure starts to rise. The pressure continues to increase with time as more hydrogen is being trapped by the cavity. Finally, the pressure reaches a constant value of 13.8 MPa. This pressure represents the local equilibrium pressure, as described by Sieverts' law, reached when the steady state is established.

Figure 62 (a) shows the concentration profiles of the 1 cavity sample at different times. The discontinuity in the profiles corresponds to the cavity where the hydrogen concentration cannot be defined. As it can be seen, the concentration increases with permeation time until

reaching a linear profile. The first two profiles show that hydrogen concentration increases in the region close to the charging side whereas the concentration is very low at the bulk-cavity interface because hydrogen did not yet reach the cavity. Then, when hydrogen reaches the cavity, the concentration starts to rise at the interface until reaching a constant concentration (light blue curve). This concentration corresponds to the local equilibrium concentration as described by Sieverts' law (Eq.(4)), which indicates that the chemical potential of the hydrogen at the interface is in equilibrium with the chemical potential of the hydrogen inside the cavity. It is important also to underline that the hydrogen concentration is linearly distributed along the sample thickness at the steady state. Figure 62 (b) represents the maps of hydrogen concentration at different times. It shows clearly the increase of hydrogen concentration during the simulation. The plotted lines represent the hydrogen fluxes inside the sample. A part of the hydrogen (near the upper and the lower sides) diffuses without being trapped by the cavity whereas the other part (close to the cavity) is being trapped.

The numerical permeation curve of the 1 cavity sample in Figure 61 (a) can be divided into 3 main domains. First, a classical (domain 1) transient regime where hydrogen diffuses through the sample until reaching the detection side and, as a result, the exit hydrogen flux starts to rise. The hydrogen flux in the 1 cavity case at 6×10^4 s is the same flux as for the simulation without cavities. This flux represents the maximum of hydrogen that was able to diffuse without being trapped in the cavity. Second, from 6×10^4 s, the hydrogen flux continues to increase slower than before as the slope decreases significantly compared to the simulation without cavities. This decrease in the slope is due to the trapping of hydrogen inside the cavity. In fact, a part of the hydrogen is being absorbed by the cavity instead of continuing to diffuse and reaching the detection side. As more hydrogen is being trapped inside the cavity, the cavity pressure (domain 2) and interface concentration increase. This increase in the hydrogen concentration at the bulk-cavity interface reduces the flux entering the cavity, which results in the cavity trapping less hydrogen. As a result, more hydrogen is available to diffuse and to reach the detection side without being trapped. Thus, the hydrogen flux continues to rise. Finally, domain 3 is the steady state. This occurs when hydrogen fugacity in the cavity is in equilibrium with the local bulk concentration.

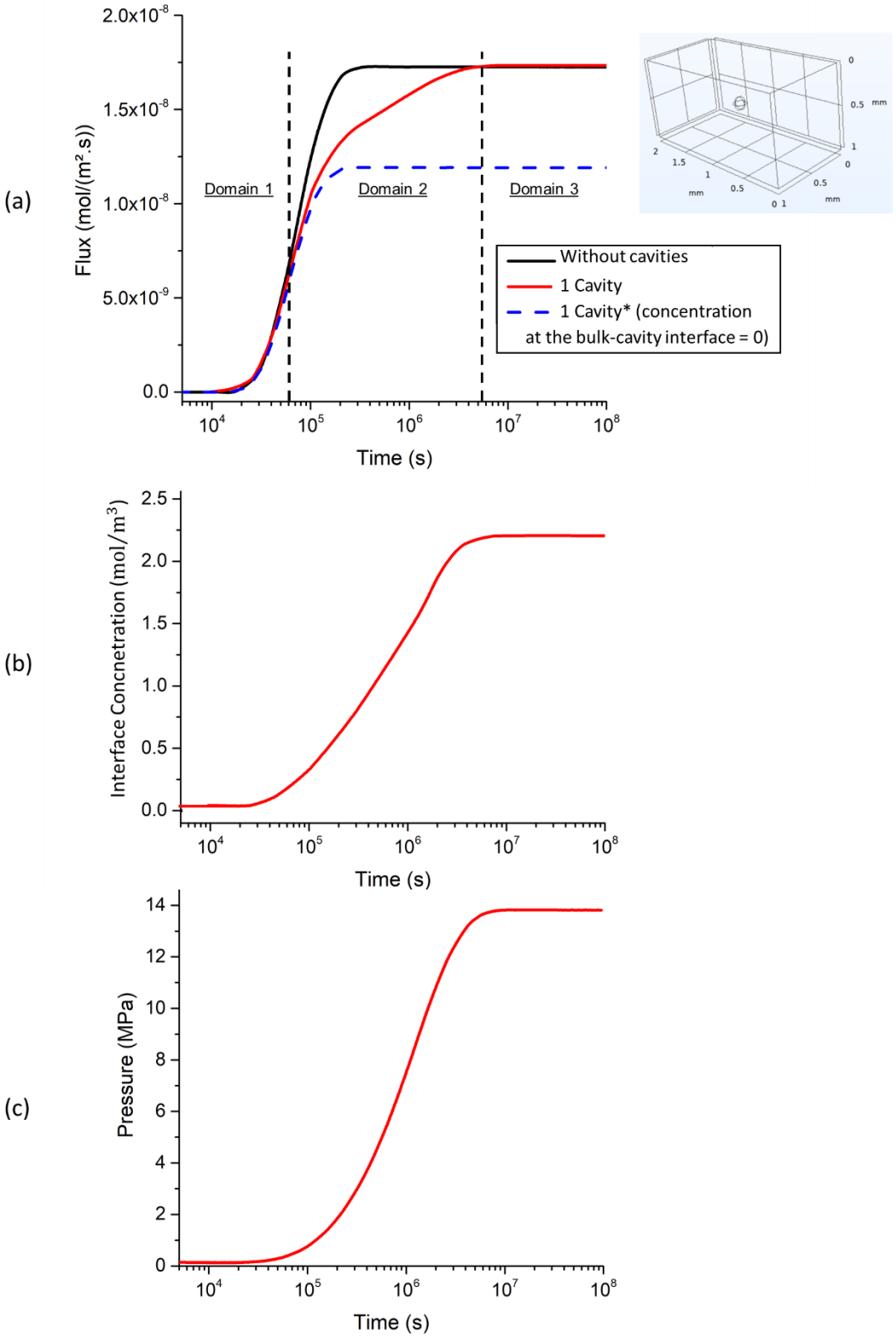

Figure 61: (a) Comparison of the hydrogen permeation flux obtained by numerical simulations for a case without cavity (black curve), a case with one cavity (red curve) and a case with one cavity with a zero concentration imposed on the bulk-cavity interface. Solubility coefficient: 0.18 mol/(m^3×$bar^{0.5}$). Porosity fraction: 0.04%. The simulation without cavity reaches the steady state before the simulation with one cavity. The delay in the permeation curve is associated to the hydrogen trapping in the cavity. (b) Hydrogen concentration at the bulk-cavity interface. (c) Time evolution of the pressure inside the cavity.

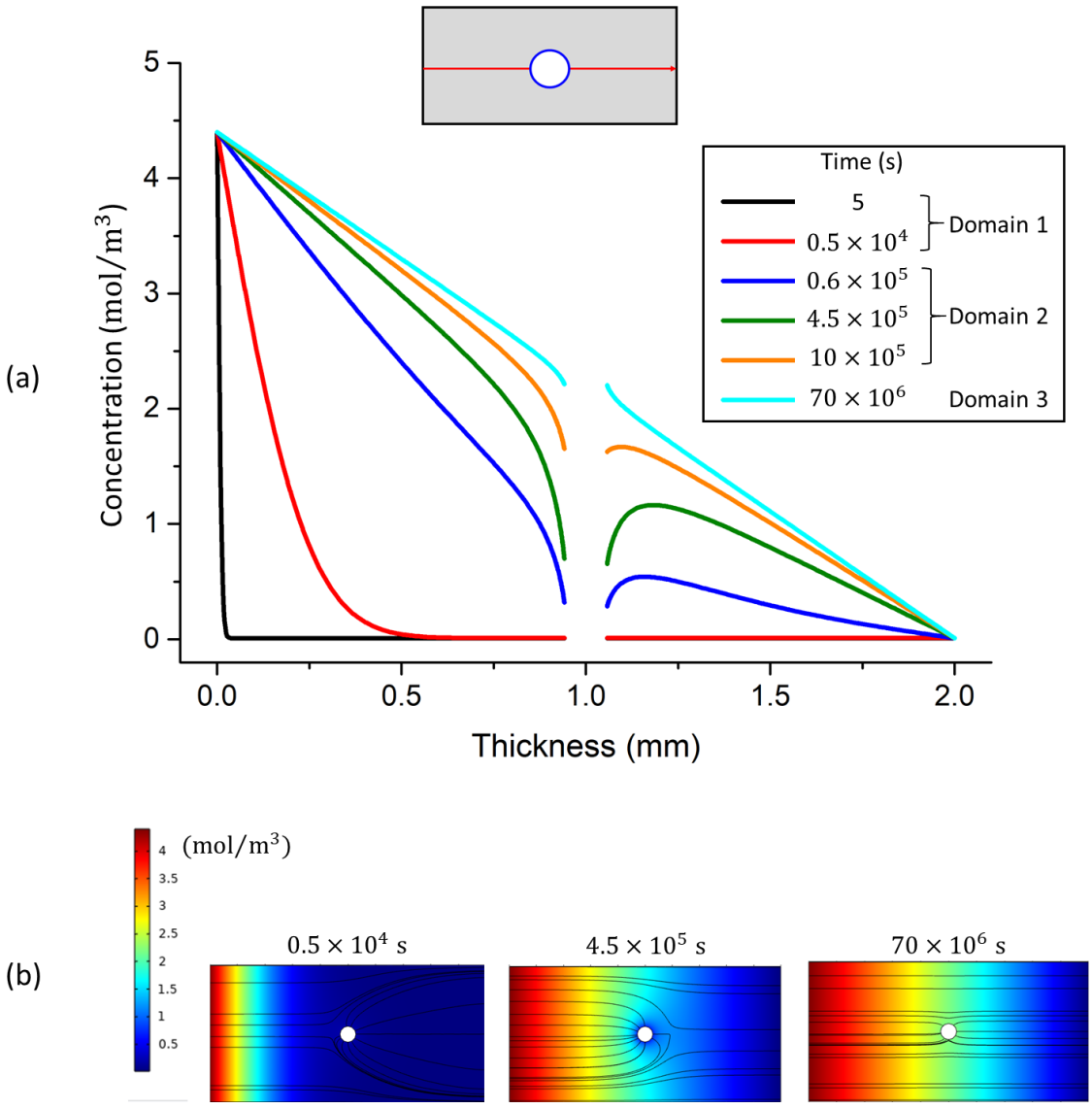

Figure 62: The time evolution of the hydrogen concentration along the sample. The solubility coefficient: 0.18 mol/(m^3×$bar^{0.5}$). Porosity fraction: 0.04%. (a) Hydrogen concentration profiles along the thickness at different times. The concentration at the bulk-cavity interface increases with permeation time until reaching the local equilibrium concentration (described by Sieverts' law). At the steady state, the concentration is linearly distributed and the chemical potential of hydrogen in the bulk is locally equal to the chemical potential of hydrogen inside the cavity. (b) The maps of hydrogen concentration at different times. The concentration increases (from left to right) with permeation time. The lines represent the local hydrogen fluxes, showing the trapping effect of the cavity.

IV.4.1.4 Multiple cavity case

All the results presented earlier were based on simulations performed on a box with just one cavity. In this section, the results were obtained from several simulations performed on boxes that have different numbers of cavities. The aim was to highlight the effect of number of cavities on the permeation behavior. It should be noted that the porosity fraction was

maintained constant at the same value (0.04%) for all the simulations in order to exclude the effect of the porosity fraction on the results (this point is discussed in details in section IV.4.3.1). Therefore, the box size, the side length to be more accurate, had to be modified in order to maintain the same porosity fraction (the thickness was kept the same 2 mm). Table 8 summarizes the geometric parameters and the different characteristics of the simulation boxes used in this work.

Figure 63 shows two simulation boxes. The first one (Figure 63 (a)) corresponds to the simulation box with one cavity and the second one (Figure 63 (b)) represents a simulation box containing 5 cavities of the same radius.

Table 8: The characteristics and the geometric parameters of the 3D simulation boxes.

Number of cavities	0	1	2	5	10	20
Inter-cavity distance (mm)	-	-	1	0.4	0.2	0.1
Cavity radius (µm)	-	78	39	16	8	4
Specimen thickness (mm)	2	2	2	2	2	2
Side length (mm)	1	1	0.5	0.2	0.1	0.05
Porosity fraction (%)	0.04	0.04	0.04	0.04	0.04	0.04

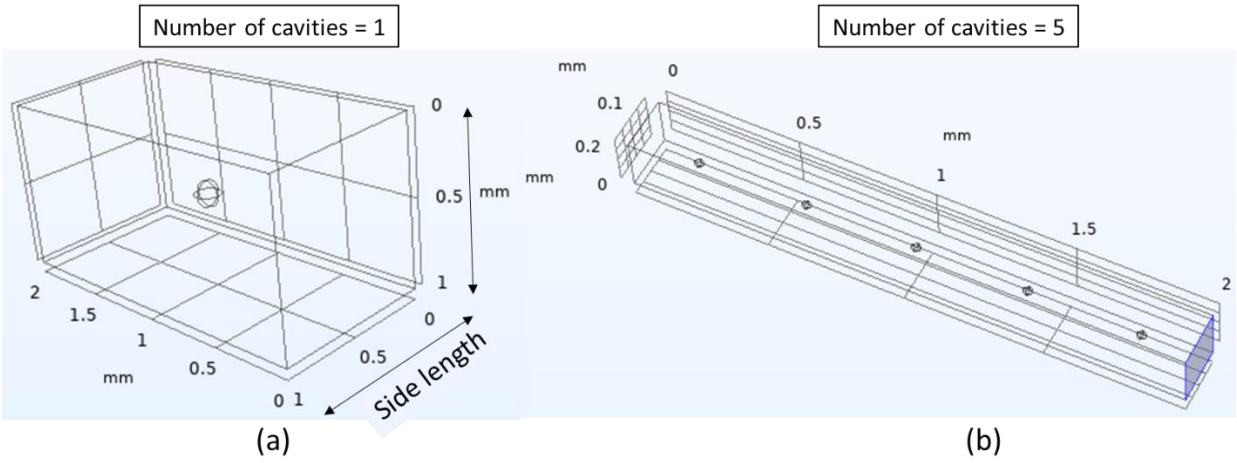

Figure 63: Examples of the 3D simulation boxes used in this study. The porosity fraction is equal to 0.04% and the specimen thickness is equal to 2 mm (a) Simulation box with one cavity placed in the center. (b) Simulation box with 5 cavities of the same radius. Periodic boundary condition consisting of a zero hydrogen flux was imposed along the lateral sides.

All the numerical simulations were performed using the same solubility coefficient (0.18 mol/(m^3×$bar^{0.5}$)). Figure 64 shows the influence of the number of cavities on the permeation flux. The hydrogen flux for all the simulations starts to rise at 2×10^4 s and then the increase of the flux becomes different from one case to another. The flux of the simulation without cavity increases faster than the others and it reaches the steady state first (around 3×10^5 s) because hydrogen diffuses without being trapped whereas, in the other cases, hydrogen was trapped in the cavities. By comparing the different curves, it is obvious, until 5×10^5 s approximately, that their slope decreases with increasing the number of cavities. Actually, the increase of number of cavities can be seen as increasing the probability of hydrogen trapping in the cavities: the more cavities there are, the more probable it is that hydrogen can be trapped. Thus, less hydrogen is available to diffuse and reach the detection side, which explains the slower increase in the hydrogen flux. This is related to the increase of bulk-cavity interface area when the number of cavities is increased. However, it was found that the number of cavities has no more effect on the permeation behavior for simulations with 10 cavities or more. On the other hand, after 4×10^5 s, there is a change in the permeation behavior. The simulation with one cavity reaches the steady state last. Again, this difference is obviously related to the interaction between cavities and hydrogen. In fact, the amount of hydrogen required to reach local equilibrium in the one cavity simulation is higher than that in the others cases simply because the cavity volume is larger. Consequently, more time was needed in order to fill the cavity and as a result, the steady state was delayed. Figure 65 shows the time

evolution of the pressure inside the cavities for the simulation with 10 cavities. It is important to recall that all cavities have the same radius. The pressure stays very low at the beginning and then when hydrogen atoms reach each cavity, the pressure starts to rise, but at different moment depending on the cavity position. The cavity near the charging side has the highest pressure and the cavity near the detection side has the lowest as it can be expected. It is remarkable that the pressure inside each cavity reaches the local equilibrium pressure at the same time as the others do.

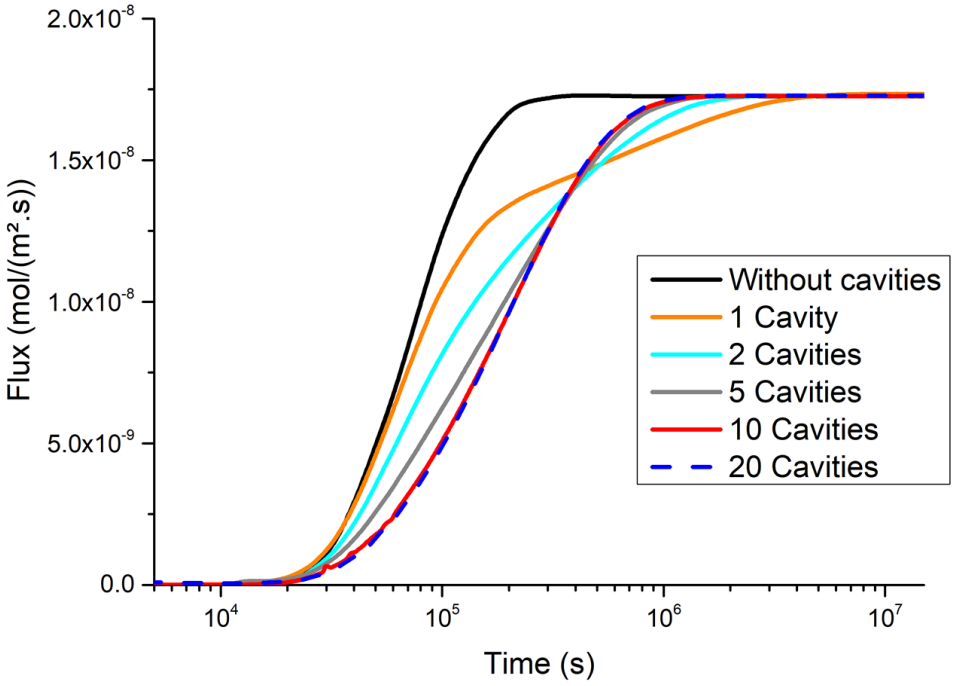

Figure 64: The effect of the number of cavities on the hydrogen permeation flux. Solubility coefficient: 0.18 mol/(m^3×$bar^{0.5}$). Porosity fraction: 0.04%. For the simulations with 10 cavities and 20 cavities, the same curves were obtained.

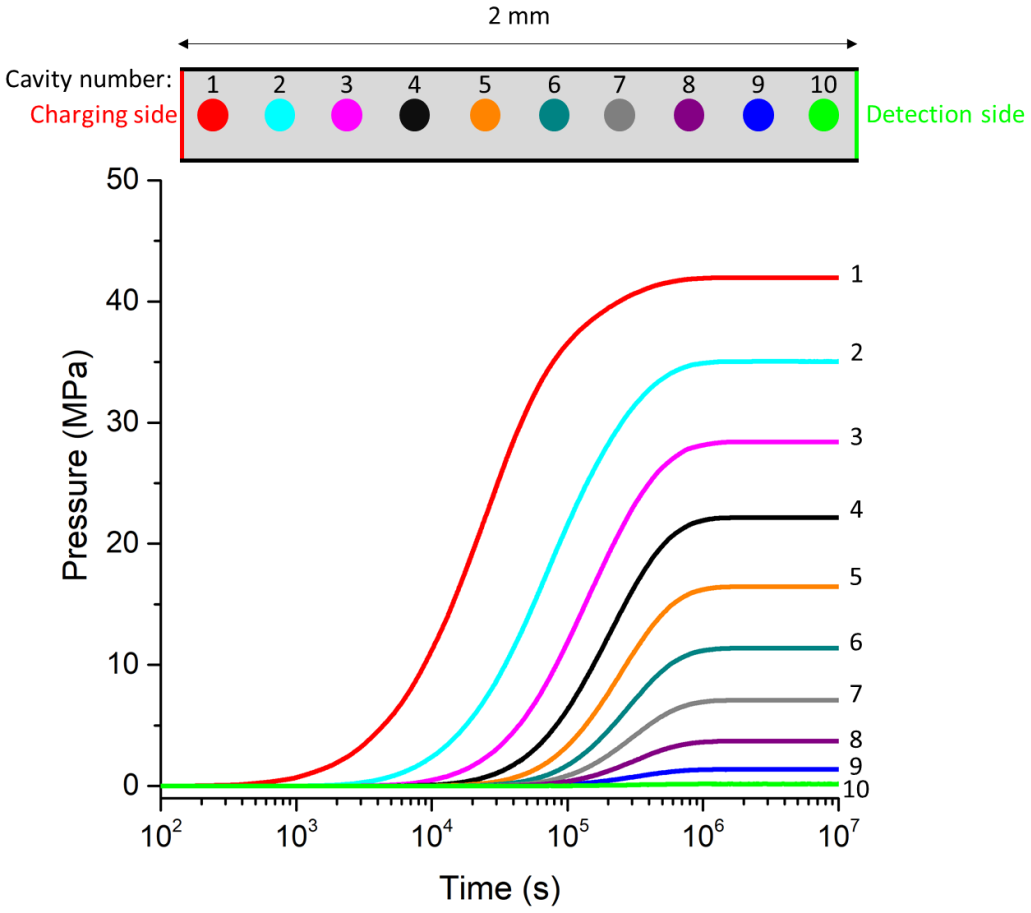

Figure 65: Time evolution of the pressure inside the cavities. Solubility coefficient: 0.18 mol/(m3×bar0.5). Porosity fraction: 0.04%. The pressure inside each cavity reaches the local equilibrium pressure at the same time.

IV.4.2 Comparison between the two models

Firstly, we should recall that the same parameters and the same conditions were used in the simulations using the non-equilibrium model and the equilibrium model as well. The results presented previously in Figure 64 shows clearly that the simulations performed using the non-equilibrium model with a number of cavities of 10 or more (with the same porosity fraction) produce the same permeation behavior. In the present section, the simulations obtained earlier (Figure 64) will be compared to the simulation results of the equilibrium model. Figure 66 (a) presents the obtained permeation fluxes as a function of time using the two models. The porosity fraction was 0.04% and the solubility was 0.18 mol/(m^3×$bar^{0.5}$). The red dashed curve corresponds to the result of the non-equilibrium model with 10 cavities and the black curve corresponds to the result of the equilibrium model simulation. Interestingly, the same permeation behavior was found in the two cases: the fluxes rise at the same time

and reach the same steady state flux at the same moment. This shows that the two models are equivalents when the non-equilibrium model is used with a sufficiently high number of cavities. For further confirmation of this conclusion, the pressure profiles across the specimen were also compared for the two models. Figure 66 (b) presents the pressure profiles at steady-state for the non-equilibrium (red dots) and the equilibrium (black curve) models. The same values of pressure are obtained, which confirms the equivalence between the two models when a large number of cavities is used in the non-equilibrium model. This is made possible by the larger bulk-cavity interface area and the smaller cavity volume, which facilitates the establishment of local equilibrium. This equivalence is an important point because the equilibrium model is easier and simpler than the non-equilibrium model. In particular, the calculation time is incomparable. The simulation takes only a few minutes to run for the equilibrium model whereas it takes hours for the non-equilibrium model using the same machine.

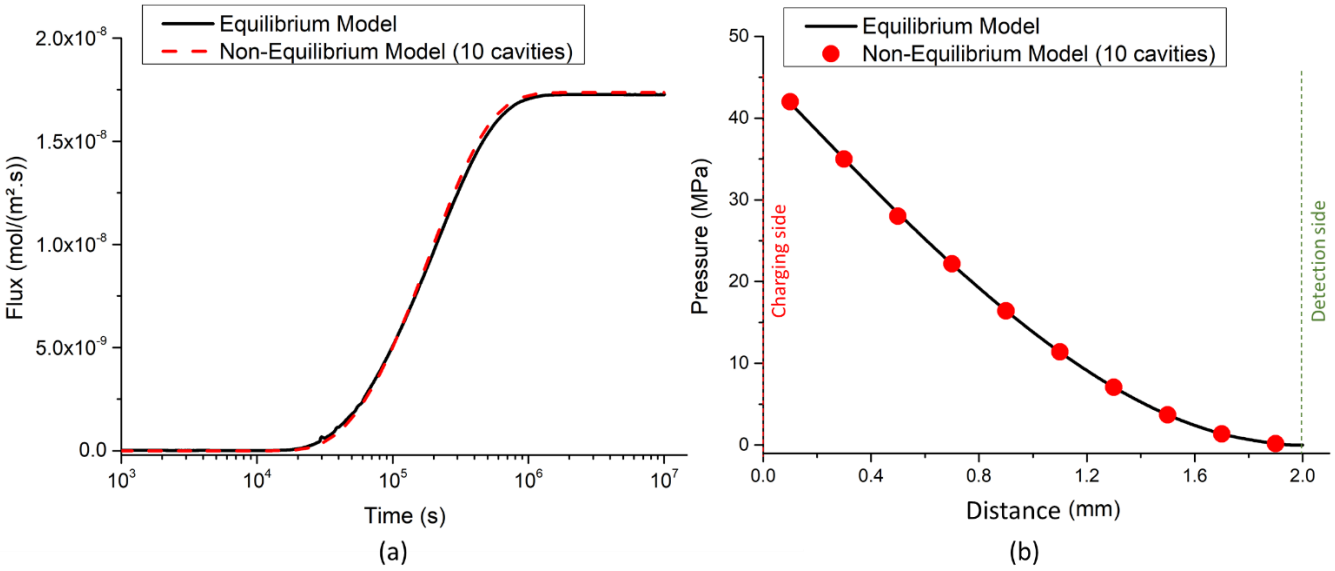

Figure 66: Comparison between the non-equilibrium model and the equilibrium model. Solubility coefficient: 0.18 mol/(m^3×$bar^{0.5}$). Porosity fraction: 0.04%. (a) The hydrogen permeation flux as a function of time and (b) steady state pressure profile in the cavities across the specimen thickness. The obtained results point out that the two models are equivalents in the case of simulations with 10 cavities or more for the non-equilibrium model.

IV.4.3 Parametric study using the equilibrium model

The equilibrium model presented in this work makes it easier to study the effect of different parameters on the hydrogen permeation behavior compared to the non-equilibrium

model, which requires a 3D FEM resolution. In the following sections, the equilibrium model was used to study the influence of the porosity fraction, the solubility coefficient and the fugacity of the charging medium on the permeation behavior.

IV.4.3.1 Porosity fraction effect

Figure 67 (a) summarizes the results of various simulations performed with different porosity fractions. The porosity fraction vary from 0% to 0.4%. The computed results showed that not only the time needed to reach the steady state increases with increasing the porosity fraction but also the time needed for the first hydrogen atoms to reach the detection side increases. For the simulation without porosity, the steady state was reached faster because hydrogen diffuses without being trapped. For the other simulations, the increase of the porosity fraction means an increase of the amount of trapped hydrogen. Consequently, less hydrogen is available to diffuse to the detection side without being trapped and therefore hydrogen flux increases more slowly. In Figure 67 (b), the time needed to reach J_{max} / 2 is correlated to the porosity fraction. It shows that, under the conditions tested here, the diffusion time increases linearly with increasing the porosity fraction, which is in agreement with the expression of the apparent diffusion coefficient (D_{app}) presented in Eq.(17).

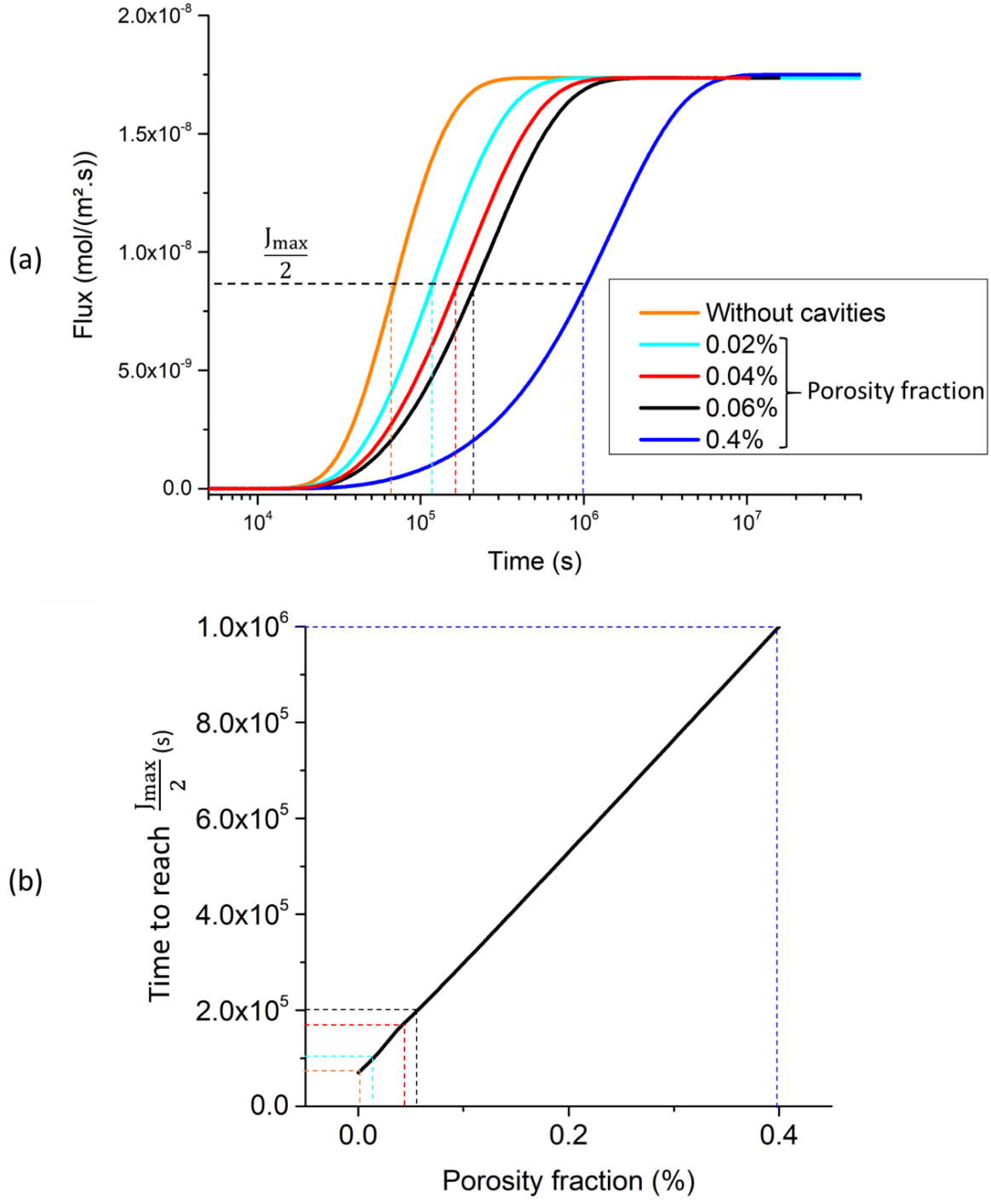

Figure 67: The influence of the porosity fraction on the hydrogen permeation flux. Simulations were performed using the equilibrium model. Solubility coefficient: 0.18 mol/(m^3×$bar^{0.5}$). (a) The simulated permeation curves. (b) The time to reach J_{max} /2 as a function of the porosity fraction. The permeation time increases linearly with increasing the porosity fraction.

IV.4.3.2 Hydrogen solubility effect

Four different calculations have been performed in order to determine the influence of the solubility on the permeation behavior. Figure 68 (a) provides the results of these simulations, performed under identical conditions but with different solubility coefficients. The porosity fraction was also the same in the four simulations and it was equal to 0.04%. It should be mentioned that the hydrogen concentration on the charging side was different from one case to another. Actually, as mentioned earlier, a constant fugacity of 600 atm was applied on the charging side, thus the hydrogen concentration varies when varying the solubility coefficient. As a result, the steady state flux was not the same for all the simulations. In order to make the comparison easier, the normalized flux (J/J_{max}) is plotted in Figure 68 (b). First, note that the orange curve corresponds to a simulation based on a solubility coefficient found in literature [63] while the blue, red and light blue curves were simulated using the solubility coefficient calculated in the previous chapter (0.180 ± 0.045 $mol.m^{-3}.bar^{-1/2}$). The results showed that increasing the solubility tends to decrease the permeation time. As already shown, increasing hydrogen solubility reduces the trapping effect of the porosity. Therefore, the hydrogen flux increases faster. In Figure 68 (c), the time to reach the J_{max} / 2 is plotted with respect to the solubility coefficient. It indicates that the permeation time and the solubility coefficient have an inverse relationship, which is in agreement with Eq.(17).

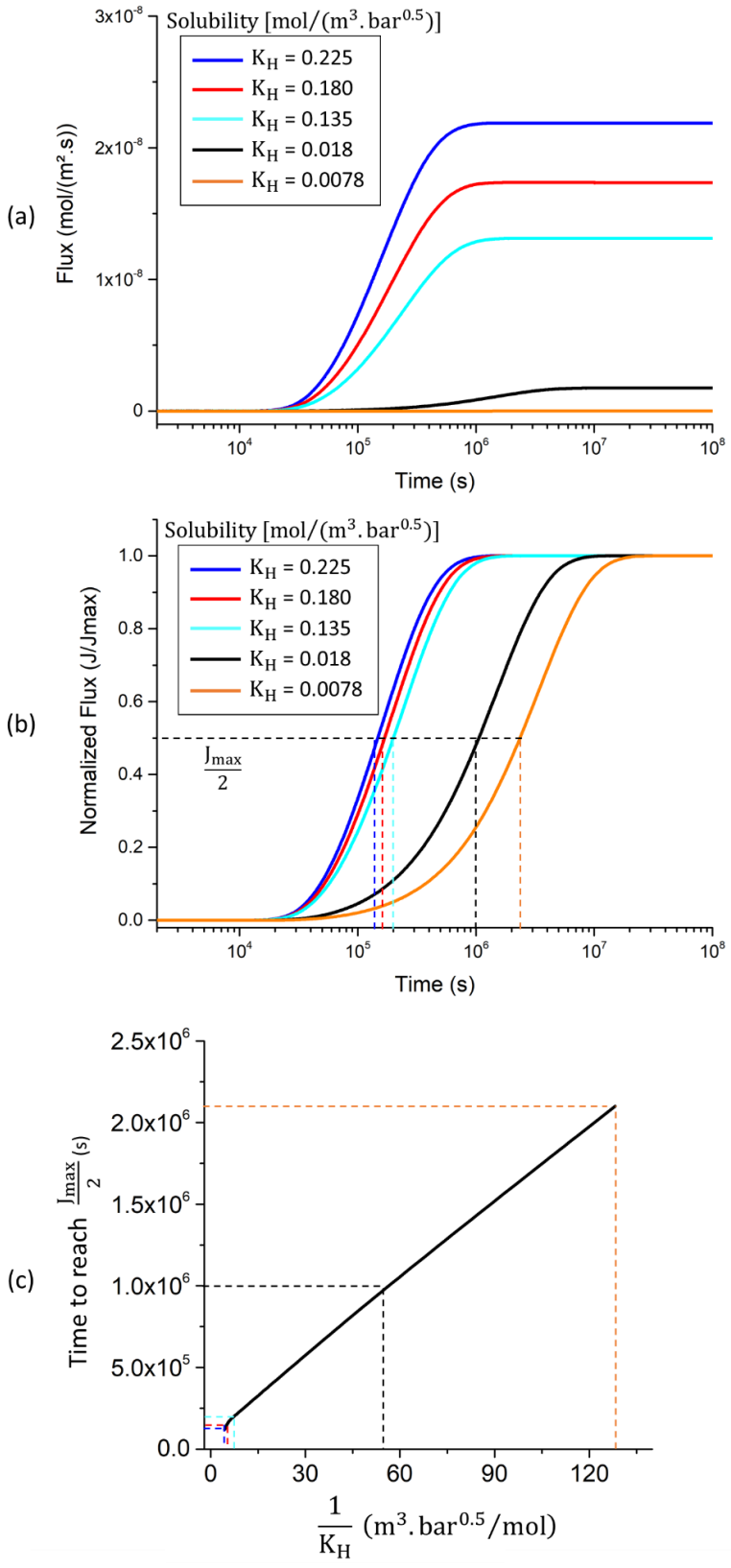

Figure 68: The effect of the solubility coefficient on the hydrogen permeation flux. Simulations were performed using the equilibrium model. Porosity fraction: 0.04%. (a) The simulated permeation curves before normalization. (b) The simulated permeation curves after normalization. (c) The time needed to reach J_{max} /2 as a function of the solubility coefficient. The permeation time is inversely proportional to the solubility coefficient.

IV.4.3.3 Hydrogen fugacity effect

In this section, the influence of hydrogen fugacity of the charging medium, i.e. at the entry side, on the permeation behavior was discussed. For all the simulations, the porosity fraction was equal to 0.04% and the solubility coefficient was equal to 0.18 mol/(m^3×$bar^{0.5}$). Figure 69 (a) shows the normalized permeation curves for different hydrogen fugacities. As it can be seen, the hydrogen flux rises faster and reaches the steady state earlier in the case of low fugacities compared to high fugacities. In order to better visualize this effect, the relationship between the time needed to reach J_{max} / 2 and hydrogen fugacity is presented in Figure 69 (b). The relationship indicates that the permeation time increases approximately as the square root of hydrogen fugacity. Once again, this conclusion is in concordance with the expression given in Eq.(17).

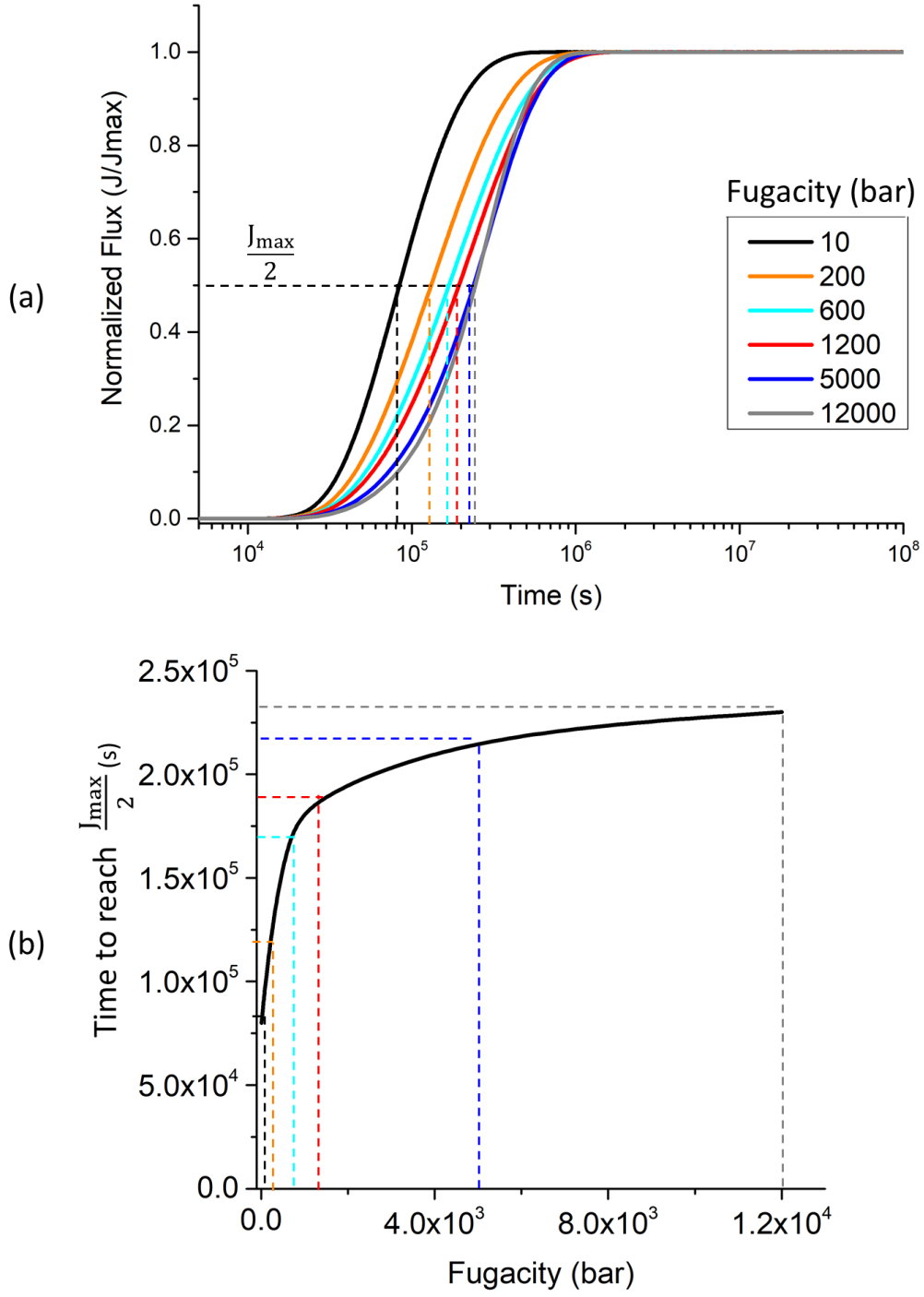

Figure 69: The influence of hydrogen fugacity at the entry side on the permeation behavior. Porosity fraction: 0.04%. Solubility coefficient: 0.18 mol/(m^3×$bar^{0.5}$). (a) Simulated permeation curves. (b) The time needed to reach J_{max} /2 as a function of hydrogen fugacity. The permeation time increases as the square root of fugacity.

IV.4.4 Comparison to the experimental data

In the previous chapter, electrochemical permeation tests were conducted on a cast sample with a porosity fraction of 0.04 ± 0.02% and a forged sample in order to highlight the effect of the porosity in hydrogen diffusion and trapping. Furthermore, hydrogen solubility in the forged material was determined and it was found equal to 0.18 ± 0.045 mol/(m^3×$bar^{0.5}$). X-ray tomography measurements presented in the previous chapter (Table 2) have shown that the average inter-cavity distance is of 138 µm. This means that there are approximately 15 cavities along the thickness of the permeation specimen (2 mm). Considering the equivalence between the equilibrium and non-equilibrium models for "large" numbers of cavities (> 10 in this case), only the equilibrium model was used here. In the current section, a comparison was made between the experimental and the numerical permeation curves in order to estimate the model predictivity. Figure 70 shows the obtained permeation curves: the solid curves represent the experimental data from electrochemical permeation and the dashed curves represent the simulations. The red and blue curves correspond to the forged (without cavities) and the cast (with a porosity fraction of 0.04%) samples, respectively. It should be recalled that the diffusion coefficient used in the numerical simulations is the apparent diffusion coefficient of the forged sample obtained from the experimental curve by the time-lag method (see Table 7). The zone colored in light blue corresponds to the uncertainty zone for the computed curve considering the uncertainty of the porosity fraction and the solubility coefficient. It ranges between two extreme cases: the first case (the upper limit) is a simulation with a porosity fraction 0.06% and a solubility coefficient of 0.135 mol/(m^3×$bar^{0.5}$). The second case (the lower limit) is a simulation with a porosity fraction 0.02% and a solubility coefficient of 0.225 mol/(m^3×$bar^{0.5}$). First, it is important to mention that the increase of the flux at the beginning of the test ($t \approx 10^3$ s) for the experimental data was explained in the previous chapter by a microstructure effect and that this point is not discussed here. Then, in both cases, experimental and simulated, the forged sample reaches the steady state before the cast sample because of the hydrogen trapping in the cavities as explained previously. The simulation result of the forged material is close to the experimental curve especially at $J_{max}/2$, which can be totally expected because the simulation was performed using the apparent diffusion coefficient extracted from this particular experimental curve. Based on the experimental curves, the cast material needed almost twice the time to reach $J_{max}/2$ compared

to the forged one. This same factor is around 2.3 for the numerical simulations. Accordingly, it is safe to conclude that the delaying effect of porosity is reasonably predicted by the numerical model. Moreover, it is important to note that the numerical results were obtained without any parameter adjustment. However, as it can be seen in Figure 70, the slope is different between the simulated and the experimental curves especially in the case of the cast sample, the experimental slope being steeper. This difference in the slope could be explained by the hydrogen interaction with microstructural defects [131][132]. This was not considered in the proposed model that focuses on the effect of porosity only.

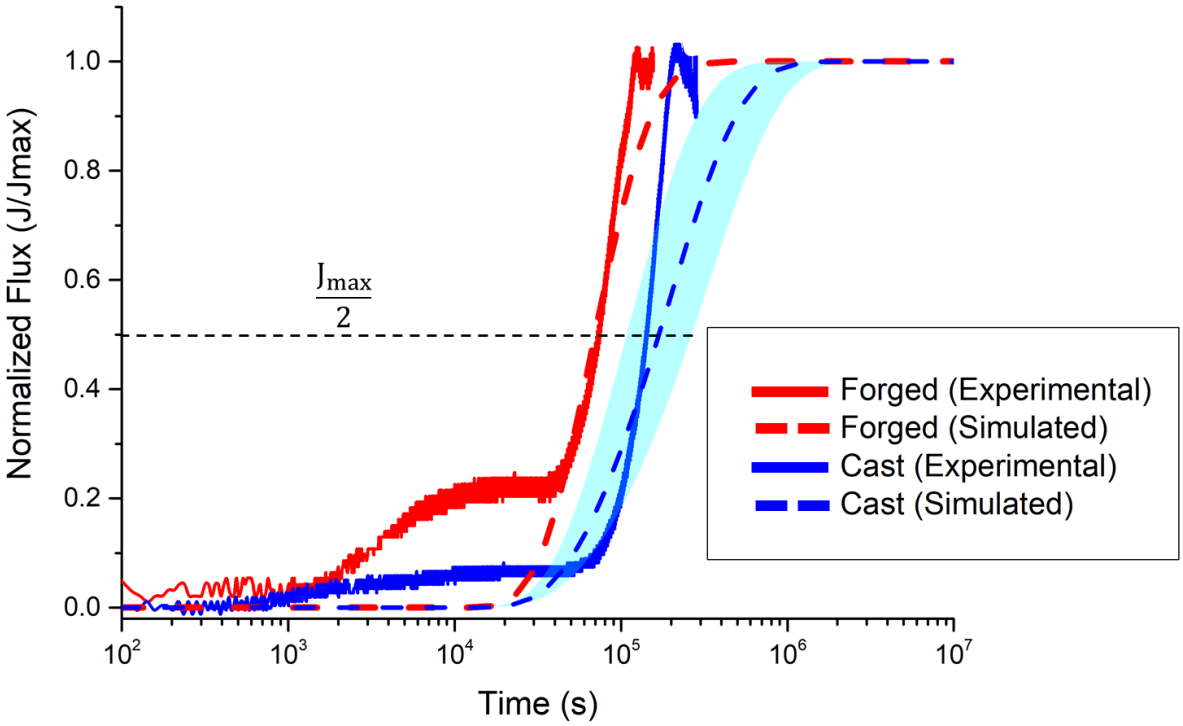

Figure 70: Comparison between the experimental and simulated permeation curves. The red color corresponds to the forged material (without cavities) and the blue color corresponds to the cast material (porosity fraction is equal to 0.04%). The solid curves: experimental; the dashed curves: simulated. The solubility coefficient was 0.18 mol/(m^3×$bar^{0.5}$) for the blue dashed simulation. The light blue zone represents the uncertainty zone and it was defined based on two simulations: the lower limit simulation using a porosity fraction of 0.02% and a solubility coefficient of 0.225 mol/(m^3×$bar^{0.5}$) and the upper limit simulation using a porosity fraction of 0.06% and a solubility coefficient of 0.135 mol/(m^3×$bar^{0.5}$).

IV.5 Conclusions

In this study, two numerical models have been proposed in order to simulate hydrogen permeation for a steel containing porosity. These two models take into account the trapping of gaseous hydrogen in cavities. They are based on two different approaches: the first model is based on a non-equilibrium approach, where a reaction flux is considered at the bulk-cavity interface and the second model is based on a local equilibrium approach, between hydrogen dissolved in the bulk and gaseous hydrogen in the cavities. It should be mentioned that the second model is simpler and less time consuming compared to the first model. The numerical models were discussed in details first and then the results were compared to the permeation experimental data presented in the previous chapter. It is important to note that the two models were developed based on a refined EOS, which permits to perform simulations on a wide range of pressure [0, 2000 MPa]. The following main conclusions can be drawn:

- For the non-equilibrium model, an expression of hydrogen flux due to the recombination reaction of atomic hydrogen into molecular hydrogen at the bulk-cavity interface was developed based on a non-equilibrium approach. The flux orientation (inward or outward) is controlled by the hydrogen concentration at the interface and hydrogen fugacity inside the cavity. A choice was made in this study to work in a diffusion-limited regime instead of an interface reaction-limited regime.
- The permeation behavior across a simulation box containing one single cavity was studied in details. The time evolution of cavity pressure, bulk-cavity interface concentration and permeation flux was found consistent.
- The effect of the number of cavities in the simulation box was studied. For a given porosity fraction, increasing the number of cavities results in larger bulk-cavity interface area and lower cavity volume, which facilitates local equilibrium. When the number of cavities is large enough, the non-equilibrium model gives the same results as the equilibrium model.
- A parametric study using the equilibrium model was conducted. The permeation time was found to vary linearly with X_P and $\frac{1}{K_H}$ where X_P is the porosity fraction in the specimen and K_H is the hydrogen solubility in the bulk material (Sieverts' constant).

In addition, it was found that the permeation time increases as the square root of hydrogen fugacity (f_{H2}) at the entry side.

- Finally, a comparison between permeation experiments and simulations was made and showed a good agreement, although no input parameter was adjusted. However, the numerical models need further refinement (other type of traps should be included) in order to improve their predictivity.

Chapter 5: Hydrogen embrittlement

V.1 Introduction

The issue of Hydrogen Embrittlement (HE) has been extensively studied for more than a century starting from the early 1870s [83]. Since then, it has been well proven that hydrogen induces degradation in the mechanical properties of steels [133][134][135]. However, it is still difficult to clearly identify which HE mechanism is responsible for a given failure. As demonstrated previously, cast steels have porosities and these porosities represent reversible trap sites for hydrogen. Furthermore, the majority of trapped hydrogen is located at the porosity. For these reasons, the focus was set in in this chapter on the combined effect of hydrogen and porosity on the mechanical properties of the studied materials. As mentioned in the general introduction, previous investigations made by the industrial partner showed the presence of a special defect on the fracture surface of some tensile specimens related to hydrogen known as “fish-eyes”. These fish-eyes present a round shape brittle area centered on a defect, which is usually a non-metallic inclusion or a void. The few studies that were performed on this topic were detailed in the first chapter. Some of these studies assumed that the fish-eye defect is a result of the high pressure of hydrogen inside a void or at the matrix-inclusion interface. They mentioned also that the fish-eye formation could occur with or without external load.

In this work, several tensile tests were performed on uncharged forged and cast specimens first in order to determine their mechanical properties before hydrogen charging. Then, tensile tests were performed on hydrogen pre-charged specimens. The hydrogen charging was conducted in a NH4SCN solution heated at 50°C. At this point, it is important to recall that the pressure inside the voids, after charging in a 5% NH4SCN solution, was estimated to be around 8 MPa (Table 6), which is far below the mechanical strength of the material. Therefore, it is not possible, in our case, to explain the fish-eye formation (if found) by the internal pressure theory. After that, the fractured pre-charged and uncharged specimens were observed using scanning electron microscopy (SEM) in order to investigate the fracture surface and try to correlate porosity and hydrogen to the failure behavior. Finally, a mechanism of fish-eye formation was proposed in our case.

V.2 Results and discussions

V.2.1 Uncharged specimens

Figure 71 shows the engineering stress-strain curves for three forged specimens and six cast specimens without any hydrogen charging. The tensile properties of both materials are given in Table 9. As it can be seen, the forged and the cast specimens exhibit almost the same yield strength and the same UTS. However, the total elongation of the forged material (19.9 ± 0.3%) is higher than that of the cast material (18 ± 1.1%), which is probably due to the porosity. The dispersion of the total elongation for the cast specimens is not only related to the volume fraction of porosity but also to the shape of voids. Unfortunately, these two informations are not available for the tensile specimens used here. That is why no detailed discussion was undertaken here about the relationship between the elongation values and the porosity.

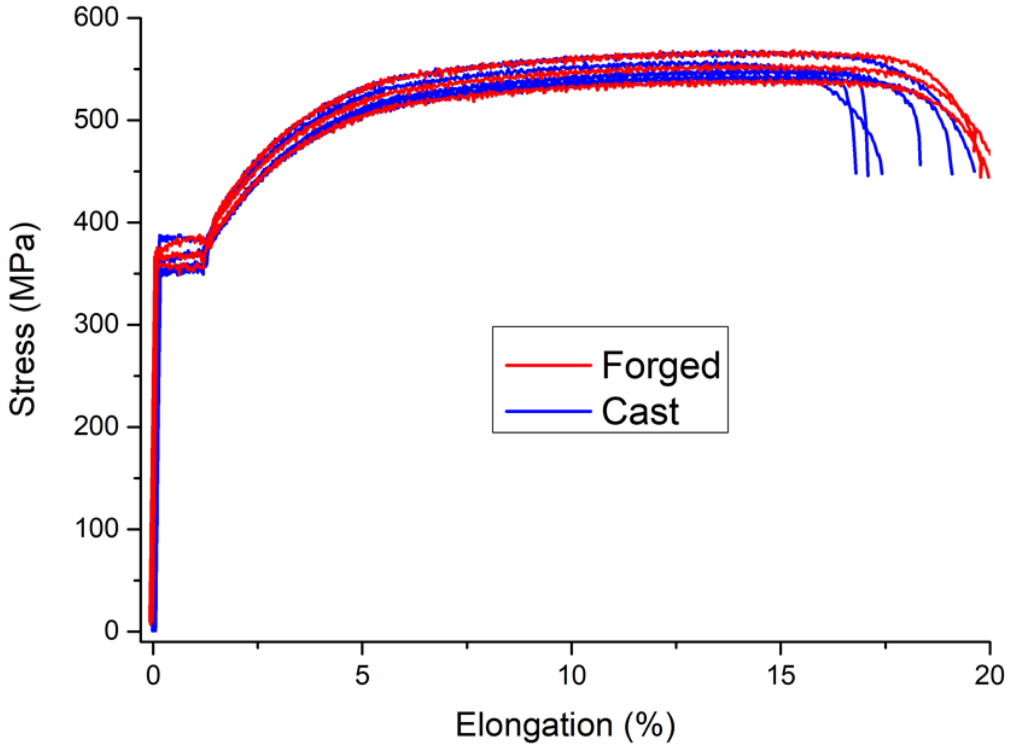

Figure 71: Stress-strain curves for forged (red curves) and cast (blue curves) specimens without hydrogen charging. The strain rate was 3×10^{-4} s^{-1}. The total elongation of the cast specimens is more widely distributed than that of the forged specimens due to porosity.

Table 9: Mechanical properties of the forged and the cast materials obtained from the tensile curves of Figure 71.

	Forged	Cast
Yield strength (MPa)	365 ± 18	360 ± 13
UTS (MPa)	553 ± 36	551 ± 9
Total elongation (%)	19.9 ± 0.3	18.0 ± 1.1

V.2.2 Pre-charged specimens

In order to explore the effect of voids and hydrogen on the mechanical properties of the cast material, especially the loss of ductility, tensile tests were performed on hydrogen pre-charged specimens. It is worth noting that all tensile tests were conducted under the same conditions (at room temperature and with a strain rate equals to 3×10^{-4} s^{-1}). Two forged and three cast specimens were charged in a 5% NH_4SCN solution heated at 50°C while two other cast specimens were charged in a 1% NH_4SCN solution heated also at 50°C. The aim of using two solutions with different NH_4SCN concentrations is to modify the hydrogen content in the specimens. This will permit to investigate the effect of hydrogen concentration on the mechanical properties of the cast material. Before hydrogen charging, the porosity fraction was measured for each cast sample using hydrostatic weighing. The results are given in Table 10.

Table 10: The volume fraction of porosity for six different cast specimens. The uncertainty of the porosity fraction is estimated at ± 0.01%.

Specimen	C1	C2	C3	C4	C5
Porosity fraction (%)	0.16	0.13	0.16	0.16	0.17

Figure 72 shows the engineering stress-strain curves for the pre-charged specimens. In addition, the stress-strain curves of a forged specimen and a cast specimen without hydrogen charging were plotted in the same graph to facilitate the comparison. These two curves represent the median curve for each material (forged and cast) based on the dataset presented in Figure 71. The tensile properties of the different specimens are given in Table 11. There is no remarkable change in the yield strength nor the ultimate strength values for both

materials whereas, for the forged specimens and for the cast specimens as well, hydrogen reduces the total elongation. A similar result was found in others works [41][86][87] as mentioned in the first chapter. To better visualize the effect of hydrogen on the material ductility, the total elongation (elongation to fracture) for each specimen are presented in Figure 73. For the forged specimens, the total elongation of the uncharged specimen is 20% whereas it is equal to 17.8% on average for the H-pre-charged specimens. For the cast material, the specimens that were charged in the 5% NH_4SCN solution lost 25% of the initial elongation (from 18.4% to an average of 13.8%). However, the ones charged in the 1% NH_4SCN solution lost only 4% (from 18.4% to an average of 17.7%). Hydrogen content in the different specimens was deduced from the TDS measurements that were performed in the previous chapter. In fact, it is possible to estimate the hydrogen content in these specimens based on the relationship between the hydrogen content and the porosity fraction presented in Figure 52. In addition, the graph of Figure 48 that shows the influence of the NH_4SCN concentration on the hydrogen content helps to deduce an approximation of hydrogen content in the 1% NH_4SCN charging (see Figure 48). Based on these findings, the total hydrogen content (C_{Total}) is around 0.2 wt ppm for the forged specimens whereas, it is about 1.1 wt ppm and 0.5 wt ppm for the cast specimens charged the 5% and 1% NH_4SCN solutions, respectively. At this point, it is important to recall that the only difference between the two materials lies in the porosity and that C_{Total} is the sum of bulk hydrogen C_B (lattice hydrogen + hydrogen in the reversible traps besides the porosity) and hydrogen in the porosity C_P . Therefore, C_{Total} is equal to C_B for the forged specimens (no porosity in the forged material). In addition, C_B is the same for the forged and the cast specimens (0.2 wt ppm) that were charged in the 5% NH_4SCN solution (same microstructure). Finally, C_B for the cast specimens charged in the 1% NH_4SCN solution was not determined at this point but it is certainly inferior to 0.2 wt ppm.

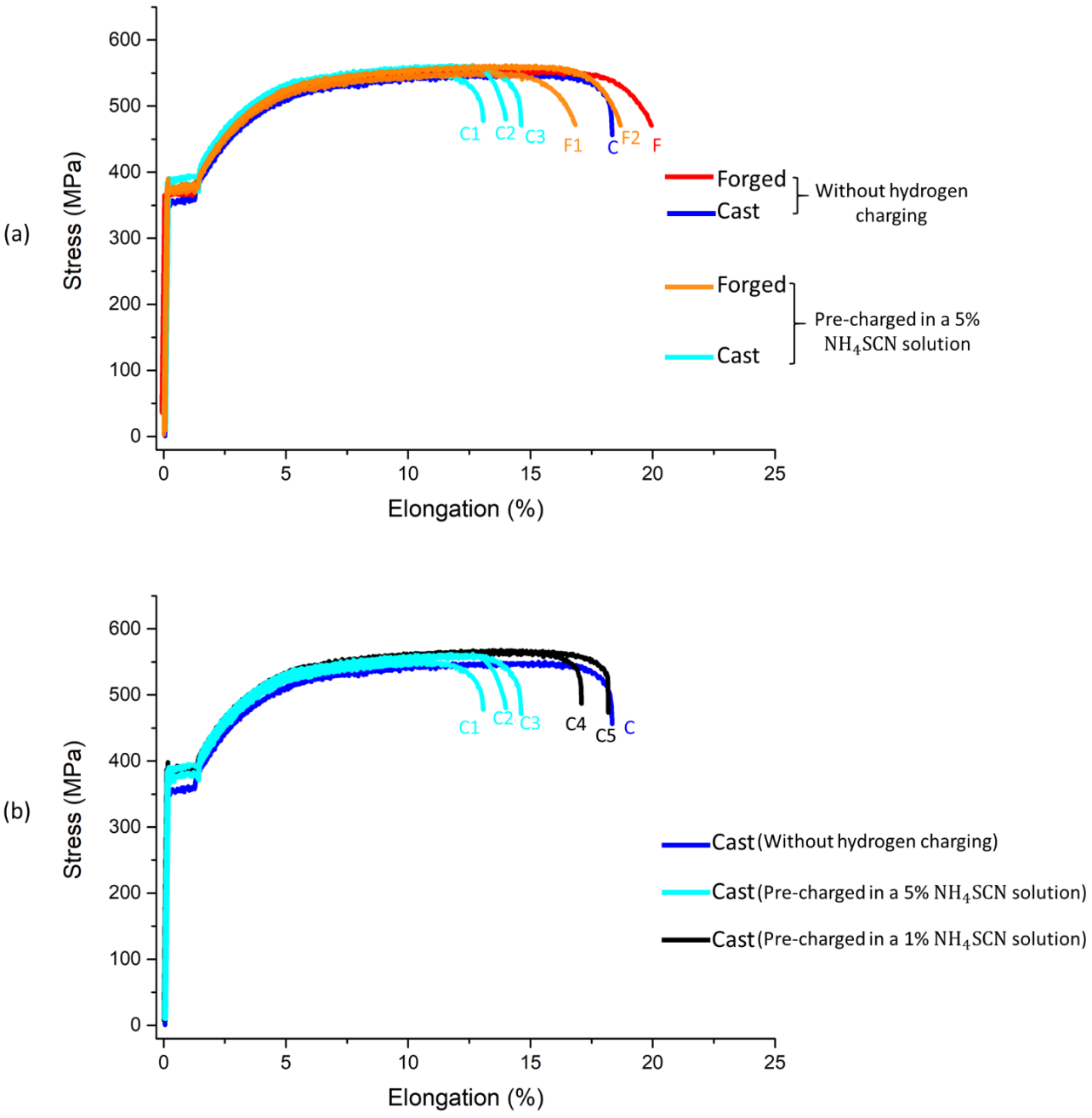

Figure 72: Tensile tests of charged and uncharged specimens. The strain rate was 3×10^{-4} s^{-1}. (a) A comparison between the forged and the cast material. The specimens (forged and cast) were charged in a 5% NH_4SCN solution. (b) A comparison between cast specimens pre-charged in two different NH_4SCN solutions. The presence of hydrogen reduces the total elongation for both material. For the cast specimens, the higher the NH_4SCN concentration in the H-charging solution, the higher the loss of ductility.

Table 11: Porosity fraction and mechanical properties of the charged and the uncharged specimens.

		Porosity fraction (%)	Yield strength (MPa)	UTS (MPa)	Total elongation (%)
Forged	Uncharged forged	-	367	552	20.0
	F1 (5% NH_4SCN)	0	370	550	16.8
	F2 (5% NH_4SCN)	0	371	560	18.7
Cast	Uncharged cast	-	360	549	18.4
	C1 (5% NH_4SCN)	0.16	384	560	13.0
	C2 (5% NH_4SCN)	0.13	373	554	13.9
	C3 (5% NH_4SCN)	0.16	375	548	14.5
	C4 (1% NH_4SCN)	0.16	378	565	17.1
	C5 (1% NH_4SCN)	0.17	382	566	18.2

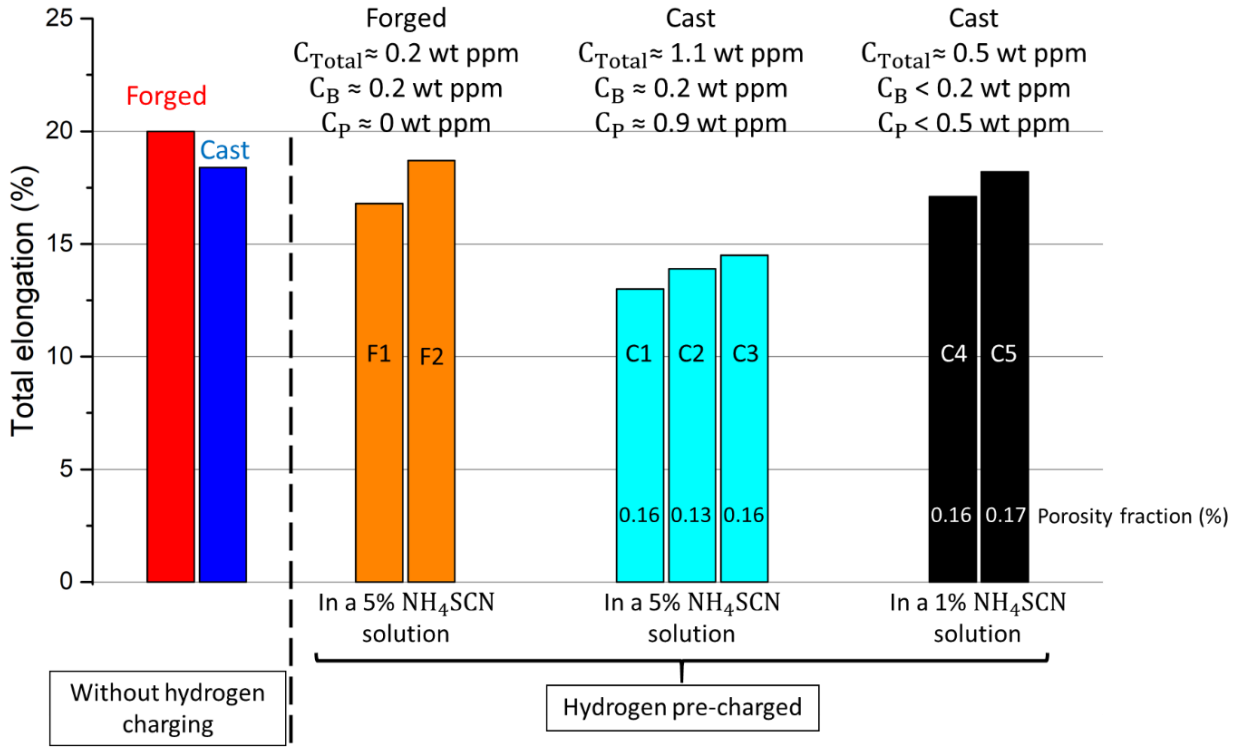

Figure 73: The total elongation for the uncharged and pre-charged specimens. The tensile tests were performed with a strain rate of 3×10^{-4} s^{-1}. Hydrogen decreases the total elongation for both materials. For the cast specimens, the loss of ductility increases with increasing hydrogen content. C_{Total} represents the total hydrogen content obtained from TDS measurements. C_{Total} is the sum of bulk hydrogen C_B (lattice hydrogen + hydrogen in the reversible traps besides the porosity) and hydrogen in the porosity C_P.

One of the ways to evaluate the susceptibility of a material to HE is the embrittlement index (EI). This index can be defined as:

$$EI = \frac{A_{in\ air} - A_H}{A_{in\ air}} \quad (38)$$

where $A_{in\ air}$ is the total elongation of the specimen without hydrogen charging and A_H corresponds to the total elongation of the hydrogen pre-charged specimen. If after hydrogen charging, the specimen becomes very brittle and breaks without any elongation (0%), the EI is equal to 1. In the other case where hydrogen does not have any effect on the total elongation, the EI is equal to zero. Thus, a higher EI means that the material is more susceptible to HE. Figure 74 summarizes the calculated EI for all the specimens. It is to be noted first that the average EI for the forged specimens is 0.12. This is definitely above the measurement error, which shows that hydrogen has a detrimental effect even in the absence of porosities. As it

can be seen, the EI of the cast specimens that were charged in the 5% NH_4SCN solution (EI = 0.25 on average) is higher than that of the cast specimens charged in the 1% NH_4SCN solution (EI = 0.04 on average). This is in concordance with their respective hydrogen contents (1.1 and 0.5 wt ppm). Consequently, the susceptibility of cast steels to HE increases with increasing the hydrogen content. On the other hand, the forged specimens charged in the 5% NH_4SCN solution (C_{Total} = 0.2 wt ppm) have an EI of 0.12 on average, which is three times higher than that of the cast specimens charged in a 1% NH_4SCN solution (C_{Total} = 0.5 wt ppm) despite the fact that the forged material has in total less hydrogen. This illustrates that there is in general no direct relationship between the EI and the total H content. In fact, this difference in hydrogen concentration is due to the hydrogen stored in the porosity as demonstrated in the third chapter (see Figure 50). It seems that the EI correlates better with the hydrogen concentration in the bulk (C_B). This concentration is equal to 0.2 wt ppm for the forged material, which is higher than that of the cast material charged in 1% NH_4SCN solution.

We now compare the forged and cast specimens charged in the 5% NH_4SCN solution. As mentioned earlier, C_B is the same in both cases. Furthermore, the cast specimens have a higher EI than the forged ones for a 5% NH_4SCN charging. Therefore, the loss of ductility for the cast specimens charged in the 5% NH_4SCN is caused by a combination of the hydrogen in the bulk and the hydrogen trapped in the porosity which had a significant role in this case in contrast to the case with 1% NH_4SCN charging.

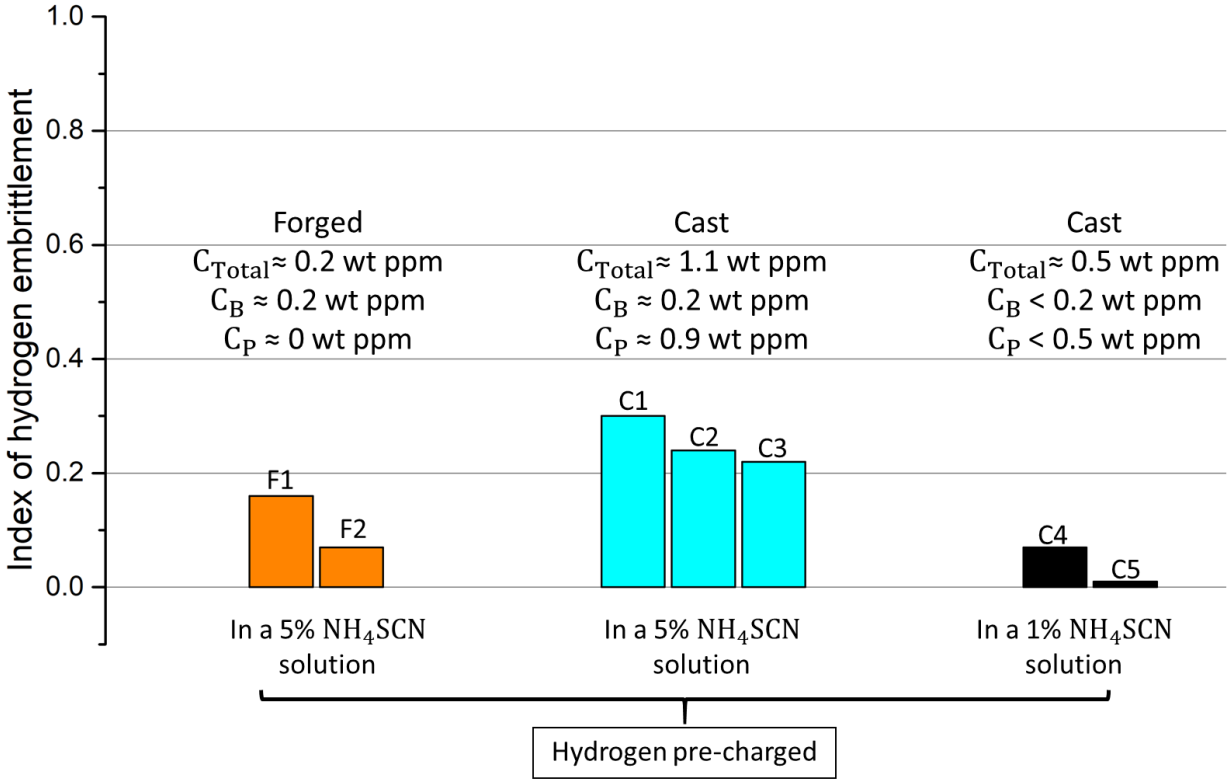

Figure 74: Hydrogen embrittlement index for the pre-charged (forged and cast) specimens calculated using Eq.(38). The tensile tests were performed with a strain rate of 3×10^{-4} s^{-1}. C_{Total} represents the total hydrogen content obtained from TDS measurements. C_{Total} is the sum of bulk hydrogen C_B (lattice hydrogen + hydrogen in the reversible traps besides the porosity) and hydrogen in the porosity C_P.

V.2.3 Fracture surface analysis

To evaluate the effect of hydrogen on the fracture behavior of the forged and the cast specimens, the fractured specimens were investigated using a scanning electron microscope (SEM). Figure 75 summarizes the fracture surfaces of five different specimens. It is important to mention that all tensile tests were performed under the same conditions (at room temperature and with a strain rate of 3×10^{-4} s^{-1}). The fracture surfaces are presented in Figure 75. For the uncharged specimens (Figure 75 (a) and (b)), the fractographs show a typical ductile failure mode. These surfaces are characterized by the presence of dimples as shown in the higher magnification observations of Figure 76 (a) and (b). In addition, no significant difference in dimple shape or size were observed between the uncharged cast and forged specimens. The fracture surface of the H-precharged forged specimen (Figure 75 (c)) is close to that of the uncharged specimens (cast and forged). The same ductile appearance is

observed at higher magnification in Figure 76 (c). No occurrence of brittle areas was observed on the fracture surface despite the fact that the material was embrittled by hydrogen as discussed in the previous section. A similar result was found in the work of T.Neeraj et al. [93][94] who observed the absence of brittle areas on the fracture surface of hydrogen pre-charged specimens, showing 30% of reduction in elongation. The material used in their study was a ferritic-pearlitic steel (X65), which is close to our material. The authors stated that there was evidence for hydrogen-enhanced plastic flow localization in the pre-charged tensile specimens, which explains the decrease in the total elongation. Liang et al. have investigated the hydrogen effect on local plastic instabilities and they showed that hydrogen can promote localized shear band formation through the HELP mechanism [136]. It is important to mention that, for the uncharged specimens (forged and cast) and for the pre-charged forged specimens, large zones of the fracture surfaces make a 45° angle with the tensile axis, which reflects the importance of the shear stress in the failure process.

A similar fracture surface morphology was found for the cast specimens charged in the 5% and the 1% NH_4SCN solutions (Figure 75 (d) and (e)). It is composed of large ductile zones with dimples and small brittle zones located around voids. These brittle zones (inside the red circles) represent a special defect known as “fish-eyes” [95]. Some of these fish-eyes are located in the central part of the specimens while others are detected near the surface. Furthermore, it seems that the number of fish-eyes does not depend only on hydrogen concentration because we found 5 fish-eyes in the case of 5% NH_4SCN charging while 9 fish-eyes were detected in the case of 1% NH_4SCN charging. In our case, we assume that the number of fish-eyes depends also on the number of voids present in the necking region. Interestingly, all the detected fisheyes in the two cases are perpendicular to the load axis, which indicates that, in our case, the formation of fish-eyes is due to the external tensile load. If the internal cavity pressure did trigger the formation of the fish-eyes, more random orientation of fish-eyes planes would be expected, which is not the case here. Our observation that the formation of fish-eyes is related to the external tensile load is also consistent with the low cavity pressure in our material (8 MPa), i.e. well below the material strength. Figure 77 presents a closer view of the fish-eye morphology. It shows the defect in the center, the void in our case, serving as initiation site and a circular zone around the void that has been

fractured in a quasi-cleavage mode due to hydrogen, while the outer region presents a ductile fracture mode.

In summary, the SEM observations showed the presence of fish-eyes in the cast material (for both hydrogen concentrations) and its absence in the forged material. Moreover, the number of fish-eyes was higher for the specimens charged in the 1% NH_4SCN solution than the ones charged in the 5% NH_4SCN solution. However, the loss of ductility was higher in the case of the 5% NH_4SCN solution. Hence, it can be concluded that the loss of ductility is not related only to fish-eye formation. In parallel, the contribution of the hydrogen trapped in the porosity was insignificant in terms of loss of ductility for the cast specimens that were pre-charged in a 1% NH_4SCN solution compared to the ones pre-charged in the 5% NH_4SCN solution. In fact, there was apparently a considerable contribution of the hydrogen trapped in the porosity in the case of the 5% NH_4SCN charging. We assume that the loss of ductility here was due to two distinct contributions: on one hand, the localization of plastic flow due to bulk hydrogen (as in the case of the H-pre-charged forged material) and on the other hand, the interaction between hydrogen and voids (fish-eyes included).

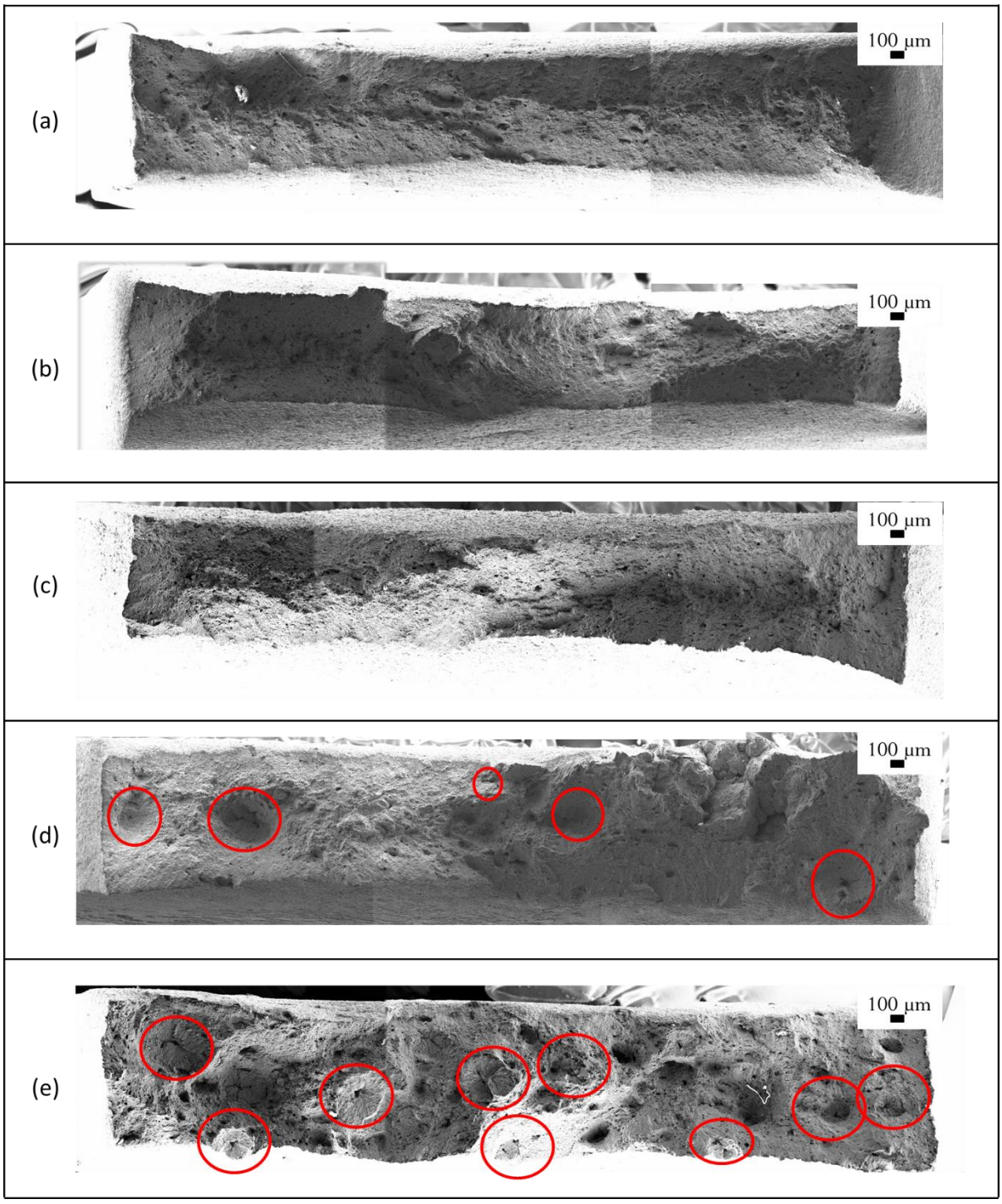

Figure 75: Fracture surfaces after tensile tests at a strain rate of 3×10^{-4} s^{-1}. (a) uncharged forged specimen (b) uncharged cast specimen (c) forged specimen pre-charged in a 5% NH_4SCN solution heated at 50°C. These three fractographs shows a typical ductile fracture. (d) cast specimen pre-charged in a 5% NH_4SCN solution heated at 50°C and (e) cast specimen pre-charged in a 1% NH_4SCN solution heated at 50°C. The red circles present the detected fish-eyes.

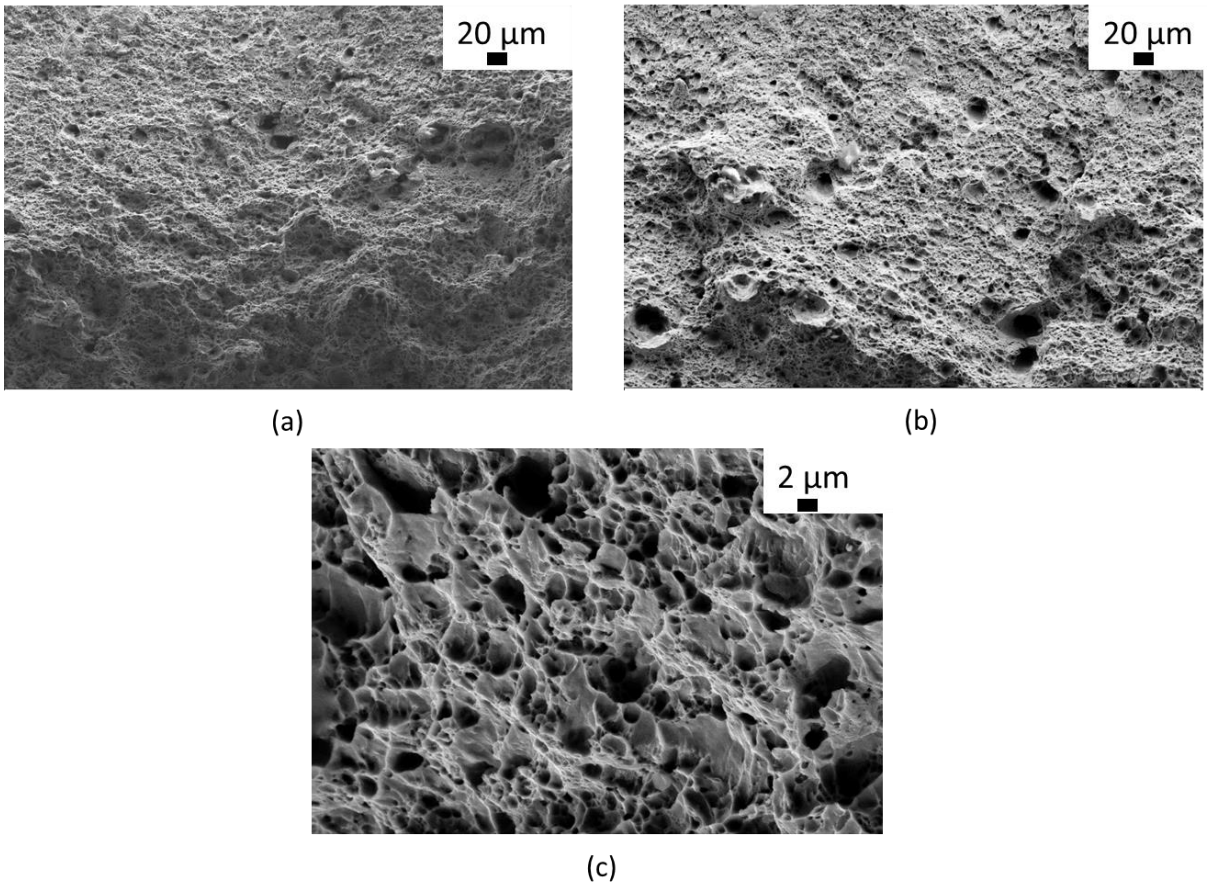

Figure 76: Fracture surface under higher magnification showing a typical ductile fracture. (a) uncharged forged specimen (b) uncharged cast specimen and (c) forged specimen pre-charged in a 5% NH_4SCN solution.

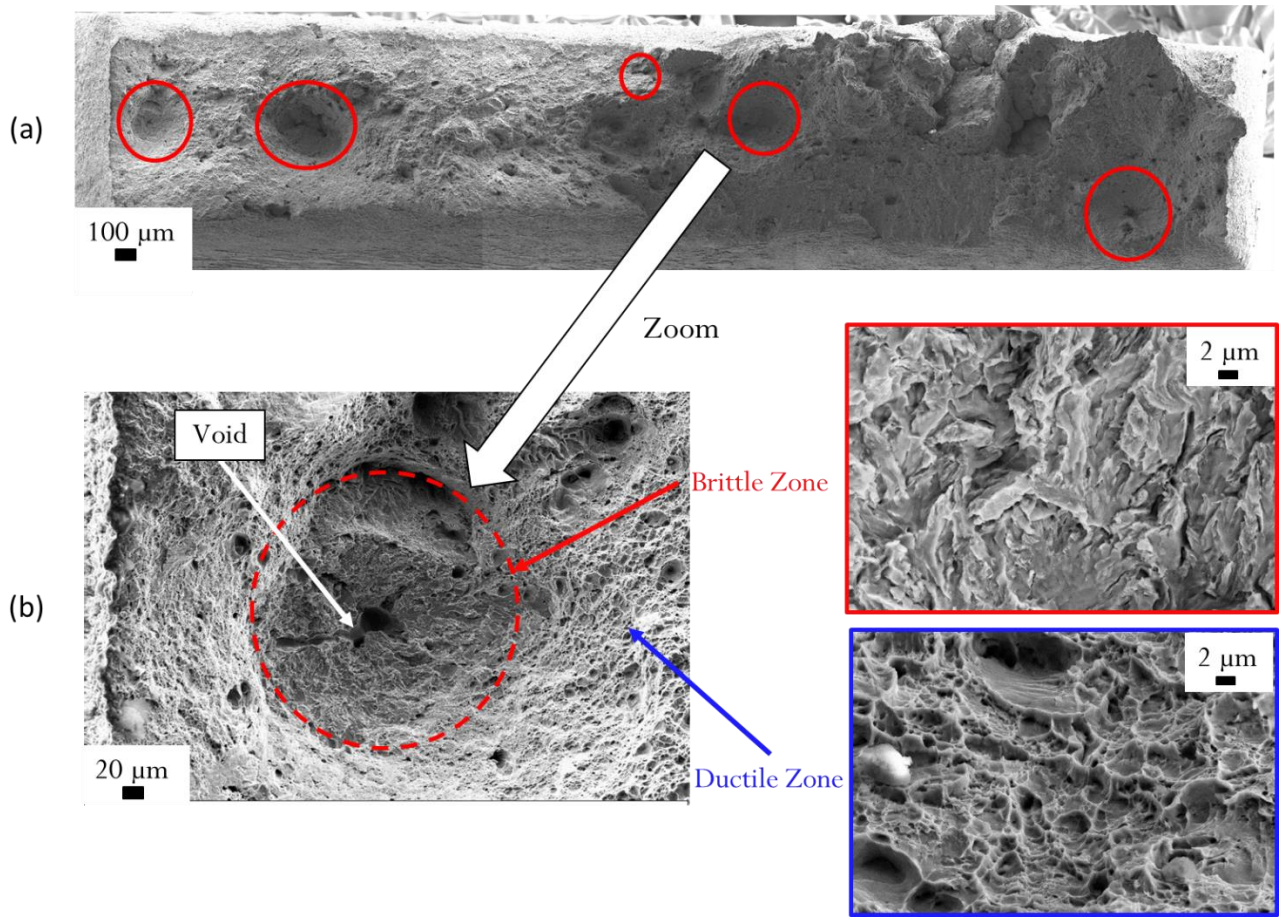

Figure 77: (a) Fracture surface of a cast specimen pre-charged in a 5% NH_4SCN solution after tensile testing. (b) The morphology of the fish-eye defect. The void is located at the center and the brittle zone around it. The outer region presents a ductile fracture.

V.2.4 Fish-eye formation at low pressures

Firstly, it is important to point out that no fish-eye was detected in the case of the uncharged cast specimens. Therefore, the fish-eye formation requires hydrogen. Secondly, for the pre-charged specimens in 5% NH_4SCN solution, the pressure inside the voids was around 8 MPa as already demonstrated previously. For this reason, it is not possible that the fish-eyes were formed due to the high cavity pressure of hydrogen as proposed in the study of Möser and Schmidt [95]. For this reason, an external load was needed, in our case, to initiate the crack. Furthermore, the detected fish-eyes were centered on the voids and not elsewhere. In fact, these voids present a sink for hydrogen where a huge amount of hydrogen can segregate in the gaseous form as demonstrated in the previous chapters. This means that the formation of fish-eyes requires a certain amount of hydrogen localized at a defect. Figure 78 (a) presents a sequence of events of a possible scenario for fish-eye formation during the tensile testing. At the start of the test, the specimen is already charged with hydrogen, which is stored mainly

in the voids as H_2 gas and adsorbed atomic hydrogen. Then, since voids present a favorable site of crack initiation because of the stress concentration, a crack will initiate when the stress exceed a certain threshold. We assume that the adsorbed hydrogen promotes the initiation and the growth of the crack. After the initiation, hydrogen, supplied by the void, is now adsorbed on the surfaces of the new crack, which should facilitate the propagation of the crack in a brittle manner as the load continues to increase. The exact mechanism responsible for the crack propagation was not entirely clarified in this work, but the HEDE (Hydrogen Decohesion) is a possibility as presented in Cialone and Asaro's work [96]. Figure 78 (b) shows a schematic representation of the fracture surface after the tensile test showing a typical morphology of a fish-eye. It shows the void at the center where a huge amount of hydrogen can be stored locally compared to the amount in the bulk, a brittle zone around the void, which is the result of crack propagation in a brittle manner and an outer region characterized by a ductile fracture. In summary, in the process of fish-eye formation, the porosity here behaves (1) as a stress concentration site and (2) a reservoir of available hydrogen. Both these effects will facilitate crack initiation and propagation. It is to be mentioned however that an external load is needed in our case, as the pressure inside the porosity (8 MPa) is far below the material strength.

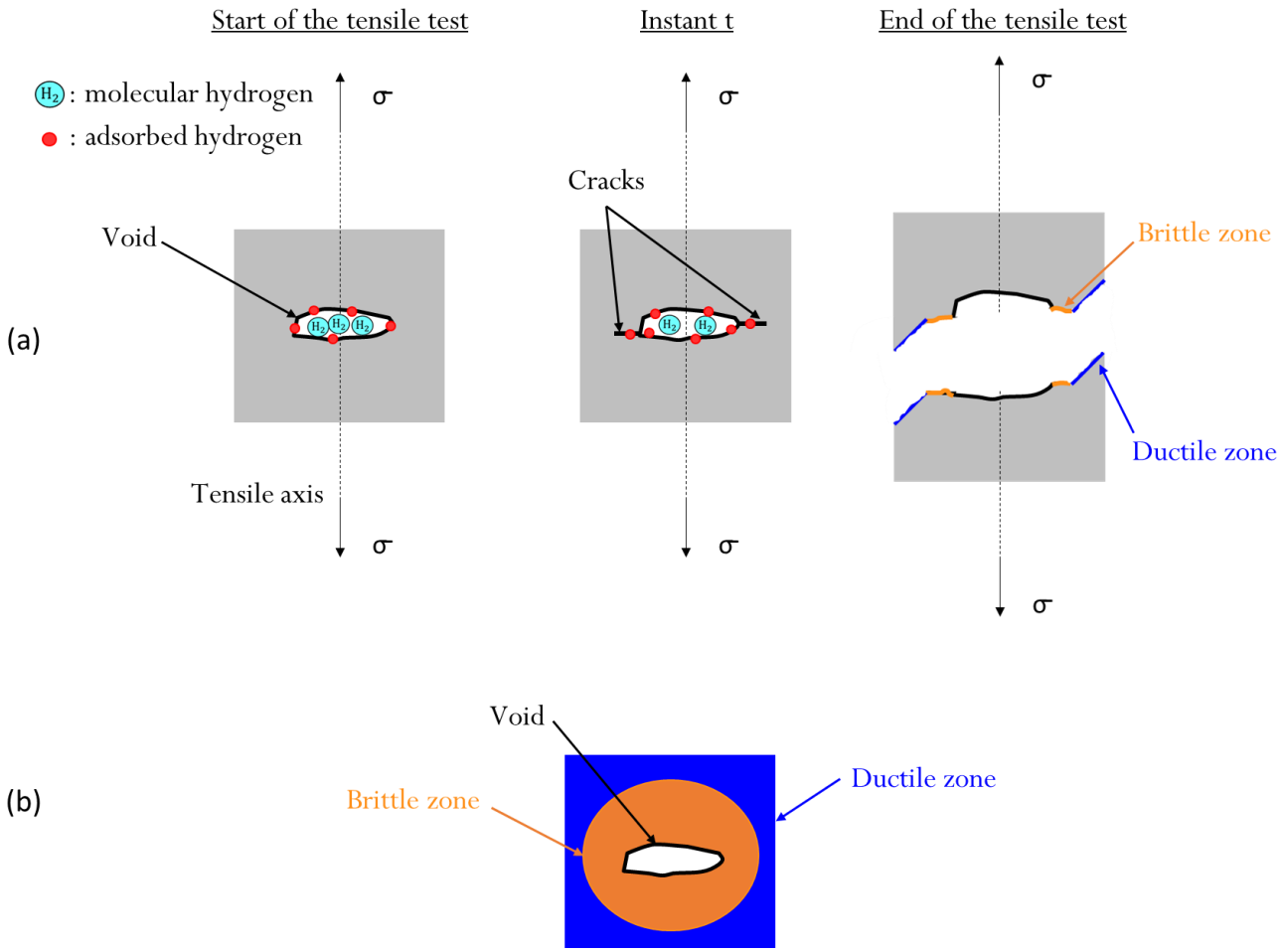

Figure 78: (a) schematic representation of the fish-eye formation during the tensile test. (b) top view of the fracture surface after tensile test.

V.3 Conclusions

In this chapter, the susceptibility to HE of the forged and the cast material was studied. The comparison between the two materials permitted to understand the combined effect of hydrogen and voids on the mechanical properties. In addition, the fracture surface investigations performed on the pre-charged cast specimens showed the presence of a defect related to hydrogen known as “fish-eyes”. The major conclusions are summarized as follows:

- Tensile tests showed no significant change in the yield strength or the UTS for the pre-charged specimens (forged and cast). However, the total elongation was affected by hydrogen.
- It was found that hydrogen did embrittle the forged specimens charged in 5% NH_4SCN solution despite the low hydrogen content (0.2 wt ppm). However, no brittle area was found on the fracture surface. We assume that the embrittlement is due the HELP mechanism.
- For the cast specimens charged in the 5% NH_4SCN solution, it seems that the loss of ductility is a result of combination between the hydrogen in the bulk through the HELP mechanism and the hydrogen trapped in the cavities, which led to fish-eyes formation.
- No direct relationship was found between HE and the different hydrogen concentrations (H_{Total}, H_{Bulk} and $H_{Porosity}$). Nevertheless, the HE was a combination of the plastic localization induced by the hydrogen in the bulk and the fish-eyes created by the hydrogen in the porosity.
- In the case of hydrogen charging at low pressures, a mechanism of fish-eye formation was proposed. The formation of this defect requires an external load and a preferential crack initiation site where a high amount of hydrogen is available.

Conclusions and prospects

Conclusions

In the present work, the aim was to increase our knowledge about the phenomenon of hydrogen embrittlement for low-alloy cast steels. As cast steels usually have porosity defects for different reasons as explained in the first chapter, the interaction between hydrogen and porosity was particularly investigated. A literature review was conducted about this interaction but the findings were not completely clear and contradictory in some cases. For instance, no firm conclusion about the nature of hydrogen trapping (reversible or irreversible) in the porosity was reached. In order to clarify this point and to investigate other issues, a comparative study was made between two states of the same material: a porous state (cast) and a non-porous state (forged). This comparison was very useful to highlight the role of porosity in hydrogen diffusion and trapping.

First, material characterization, using optical microscopy and X-ray tomography, confirmed that the only difference between the forged and the cast material was lying in the porosity. Then, the influence of porosity in the hydrogen diffusion and trapping processes has been studied by means of electrochemical permeation (EP) and thermal desorption spectroscopy (TDS). It is important to point out that a TDS measurement methodology was carefully developed (chapter 2) in order to provide reliable results and especially to avoid the contribution of the adsorbed water on the sample surfaces to the TDS signal. In fact, it was found that even a small exposure time of the sample to the atmosphere is capable to interfere with the measurement. It produces hydrogen peaks, in our case, at high temperatures even for samples without hydrogen charging. It was demonstrated that these peaks are mainly associated with the decomposition of water on the sample surfaces. Finally, it should be mentioned that the hydrogen was chemically introduced in TDS samples using a NH_4SCN aqueous solution heated at 50°C.

EP tests have shown that the diffusivity of hydrogen in the cast samples was lower than in the forged samples. This was due to the porosity, which acts as trap sites. In addition, the comparison of the decay transients between the forged and the cast samples showed that the majority of the absorbed hydrogen was trapped in voids. The same conclusion was made through TDS measurements. Furthermore, EP and TDS experiments have clearly shown that the hydrogen trapped in voids desorbed spontaneously at room temperature. This proves that

the porosity acts as a reversible trap for hydrogen at room temperature. Moreover, TDS measurements, performed on samples with different volume fraction of porosity, indicated that the total hydrogen content increases linearly with the increase of the volume fraction of porosity. Based on these findings, a method was proposed to calculate the hydrogen fugacity of the charging solution and the hydrogen solubility of the steel (Sieverts' constant) at 50°C. It was found that the hydrogen fugacity and solubility were estimated to 85 bar and $2.2x10^{-2}$ wt ppm.$bar^{-1/2}$**,** respectively. Finally, it was shown that hydrogen was mainly trapped in voids under the gaseous form in our case.

In parallel, two numerical models have been proposed in order to simulate hydrogen permeation for a steel containing porosity. These two models take into account the trapping of gaseous hydrogen in voids. It is important to note that the two models were developed based on a refined EOS, which permits to perform simulations on a wide range of pressure [0, 2000 MPa]. The models are based on two different approaches: the first model is based on a non-equilibrium approach, where a reaction flux is considered at the bulk-cavity interface and the second model is based on a local equilibrium approach, between hydrogen dissolved in the bulk and gaseous hydrogen in the voids. It should be mentioned that the second model is simpler and less time consuming than the first one. First, an expression of hydrogen flux due to the recombination reaction of atomic hydrogen into molecular hydrogen at the bulk-cavity interface was developed based on a non-equilibrium approach. In addition, a choice was made in this study to work in a diffusion-limited regime instead of an interface reaction-limited regime for the non-equilibrium model. Then, the effect of the number of cavities in the simulation box was studied and it was shown that for a given porosity fraction, increasing the number of cavities results in larger bulk-cavity interface area and lower cavity volume, which facilitates local equilibrium. Thus, when the number of cavities is large enough, the non-equilibrium model gives the same results as the equilibrium model. It was deduced that the equilibrium model is appropriate to simulate permeation in our specimens, containing numerous voids across the thickness. A parametric study using the equilibrium model was conducted and the simulations showed that permeation time varies linearly with the porosity fraction and the inverse of hydrogen solubility (Sieverts' constant). It was found also that the permeation time increases as the square root of hydrogen fugacity at the entry side. Finally, a

comparison between permeation experiments and simulations was made and showed a reasonable agreement, considering that no input parameter was adjusted.

This thesis also discussed the susceptibility to HE of the forged and the cast material. In fact, the comparison between the two materials permitted to understand the combined effect of hydrogen and voids on the mechanical properties. Tensile tests showed no significant change in the yield strength or the UTS for the pre-charged specimens (forged and cast). However, the total elongation was affected by hydrogen. SEM fractography of the pre-charged cast specimens has shown the presence of a defect related to hydrogen known as “fish-eyes”. First, it is important to mention that no direct relationship was found between HE and the different hydrogen concentrations (H_{Total}, H_{Bulk} and $H_{Porosity}$). In addition, no brittle area was found on the fracture surface of the forged specimens charged in 5% NH_4SCN solution (0.2 wt ppm) despite the reduction in the total elongation. It seems that the HE for the cast specimens was a combination of the plastic localization induced by the hydrogen in the bulk and the fish-eyes initiated by the hydrogen in the porosity. Finally, a possible mechanism of fish-eye formation was proposed for the case of hydrogen charging at low pressures. In this condition, it appears that the formation of this defect requires an external load and a preferential crack initiation site, where a high amount of hydrogen can be trapped.

Future works

As mentioned earlier, there is a lack of studies about the issue of HE for cast steels. Therefore, we think that more work has to be done on this topic and especially to explore further the interaction between hydrogen and porosity. The following suggestions, also including possible improvements of the experimental methods, are provided for future works:

Improvement of experimental methods:

- The TDS calibration curve presented in chapter 2 was not perfectly linear. This non-linearity should be confirmed and explained. It is also recommended to use other standards with a hydrogen mass below 8×10^{-6} g, i.e. closer to the hydrogen mass observed in the specimens, in order to provide more accurate results.
- The contribution of the adsorbed water in the TDS signal has been well established in this work. A systematic determination of the background signal (the same sample without hydrogen charging) has to be done in order to avoid biased results.

Scientific perspectives:

- Samples with significant difference in the porosity fraction should be used for the EP experiments in order to confirm that the permeation time increases linearly with the porosity fraction, which is predicted by the simulations
- Additional tensile tests should be performed with a lower strain rate to investigate further the role of hydrogen trapped in the porosity. In this manner, hydrogen will have more time to diffuse in the specimen, and this can affect the embrittlement observed.
- It would also be interesting to investigate the formation of fish-eyes at high hydrogen pressures to verify if they can be created “spontaneously”, i.e. without any external load or not. This would require charging the specimens at higher hydrogen fugacity, using for example cathodic charging, instead of chemical charging.
- Interrupted tensile tests coupled with SEM and EBSD (Electron Backscatter Diffraction) investigations can be performed on H-precharged specimens in order

to understand better the formation of fish-eyes. This can provide information about the crack initiation and propagation.

- In our numerical models, we only considered the trapping effect of porosity. However, as discussed earlier, other traps are present in the studied material. Therefore, it would be interesting to take in consideration the other traps in order improve the predictivity of our models in particular concerning the slope of the permeation rising transients.
- It would be also interesting to use the models developed in this study to fit the experimental TDS curves. This can help us to determine the temperature dependence of the hydrogen diffusion coefficient and possibly hydrogen solubility.

Industrial perspectives:

- Hydrogen degassing treatment (known as “baking”) is one of the important tool used in the industry to decrease hydrogen concentration in the product below a certain threshold. However, baking time can be very long especially for products with high thickness. Thus, it would be very useful to simulate these operations in order to estimate the baking time needed. For this purpose, it is possible to use the local equilibrium model presented in this work, or even possibly a simple diffusion model (it was demonstrated that at high temperatures the majority of hydrogen is in the bulk), to simulate baking operations. However, hydrogen diffusivity data at high temperatures are needed. This data can be extracted from literature (however, there are very few studies) or from a fit procedure of our TDS measurements as explained previously.

References

[1] Srinath Viswanathan et al., 'ASM Handbook, Volume 15: Casting', Dec. 2008.

[2] K. Chatterjee, D. Dollimore, and K. Alexander, 'A new application for the Antoine equation in formulation development', Int. J. Pharm., vol. 213, no. 1, pp. 31–44, Feb. 2001.

[3] R. P. Frohmberg, W. J. Barnett, and A. R. Troiano, 'DELAYED FAILURE AND HYDROGEN EMBRITTLEMENT IN STEEL':, Defense Technical Information Center, Fort Belvoir, VA, Jun. 1954.

[4] J.-C. BOSSON, 'Analyse de l'hydrogène dans les aciers', techniques de l'ingénieur - 'Étude et propriétés des métaux', Apr. 10, 1993..

[5] Jean-Marcel MASSON, 'Fonderie et moulage de l'acier - Cas pratiques : Élaboration au four à arcs, techniques de l'ingénieur', Dec. 2005.

[6] S. I. Rudyuk, É. I. Fel'dman, E. I. Chernov, and V. F. Korobeinik, 'Effect of sulfur and phosphorus on the properties of steel 18B', Met. Sci. Heat Treat., vol. 16, no. 12, pp. 1056–1059, Dec. 1974.

[7] Jean-Marcel MASSON, 'Élaboration de l'acier moulé - Analyse des processus métallurgiques. | Techniques de l'Ingénieur', Mar. 2007.

[8] J. L. Jorstad, 'ASM International, Volume 15, Electric Arc Furnace Melting', Dec. 2008..

[9] R. Singh, '5 - Production of steel', in Applied Welding Engineering (Third Edition), R. Singh, Ed. Butterworth-Heinemann, pp. 35–52, 2020.

[10] Jean-Marcel MASSON 'Élaboration de l'acier moulé - Analyse des processus métallurgiques : Désoxydation. Réglages analytiques finaux | Techniques de l'Ingénieur, 2007.

[11] Jean-Paul AYMARD , Marie-Thérèse LEGER, 'Manuel des aciers moulés', Jul. 1996.

[12] R. D. Pehlke, 'Formation of Porosity During Solidification of Cast Metals', in Foundry Processes: Their Chemistry and Physics, S. Katz and C. F. Landefeld, Eds. Boston, MA: Springer US, pp. 427–445, 1988.

[13] N. Mahomed, Shrinkage Porosity in Steel Sand Castings: Formation, Classification and Inspection. IntechOpen, 2020.

[14] M. Riedler, S. Michelic, and C. Bernhard, 'Formation of shrinkage porosity during solidification of steel: Numerical simulation and experimental validation', IOP Conf. Ser.: Mater. Sci. Eng., vol. 143, p. 012035, Jul. 2016.

[15] Jonathan A. Dantzig, Michel Rappaz, 'Solidification - 2nd Edition - Revised & Expanded - (EAN13 : 9782940222971)', EPFL Press. https://www.epflpress.org/produit/501/9782940222971/solidification (accessed Oct. 28, 2021).

[16] R. J. Fruehan and P. N. Anyalebechi, 'Gases in Metals', vol. Casting, volume 15, Dec. 2008.

[17] S.L Semiati et al., 'ASM Handbook Volume 14: Forming and forging- ASM International', 2005.

[18] S. Pillot and L. Coudreuse, '2 - Hydrogen-induced disbonding and embrittlement of steels used in petrochemical refining', in Gaseous Hydrogen Embrittlement of Materials in Energy Technologies, vol. 2, R. P. Gangloff and B. P. Somerday, Eds. Woodhead Publishing, 2012, pp. 51–93. doi: 10.1533/9780857093899.1.51.

[19] Anne-Marie Brass, Jacques Chêne, Lionel Coudreuse 'Fragilisation des aciers par l'hydrogène : étude et prévention : Manifestations industrielles des problèmes de fragilisation | Techniques de l'Ingénieur, 10 juin 2000.

[20] W. L. Kerlie and J. H. Richards, 'Origin and elimination of hydrogen in basic open-hearth steels', JOM, vol. 9, no. 12, pp. 1541–1548, Dec. 1957.

[21] H. Epstein, J. Chipman, and N. J. Grant, 'Hydrogen in steelmaking practice', JOM, vol. 9, no. 4, pp. 597–608, Apr. 1957.

[22] S. R. Bragança et al., 'Hydrogen Potential Sources in Refractory Materials during Steel Casting', Steel Res. Int., vol. 77, no. 6, pp. 400–403, 2006.

[23] Fruehan, Richard J; Misra, Siddhartha , Hydrogen and Nitrogen Control in Ladle and Casting, Technical Report, American Iron and Steel Institute, 2005 .

[24] L.-Q. Chen, 'Chemical potential and Gibbs free energy', MRS Bull., vol. 44, no. 7, pp. 520–523, Jul. 2019.

[25] D. A. Vallero, 'Chapter 4 - Environmental partitioning', in Air Pollution Calculations, D. A. Vallero, Ed. Elsevier, pp. 73–105, 2019..

[26] H. F. Hemond and E. J. Fechner, 'Chapter 1 - Basic Concepts', in Chemical Fate and Transport in the Environment (Third Edition), H. F. Hemond and E. J. Fechner, Eds. Boston: Academic Press, pp. 1–73, 2015.

[27] B. L. Murphy, 'Chapter 7 - Chemical Partitioning and Transport in the Environment', in Introduction to Environmental Forensics (Third Edition), B. L. Murphy and R. D. Morrison, Eds. San Diego: Academic Press, pp. 165–197, 2015.

[28] I. Tosun, 'Chapter 5 - Fugacity of a Pure Component', in The Thermodynamics of Phase and Reaction Equilibria, I. Tosun, Ed. Amsterdam: Elsevier, pp. 119–162, 2013.

[29] C. S. Marchi, B. P. Somerday, and S. L. Robinson, 'Permeability, solubility and diffusivity of hydrogen isotopes in stainless steels at high gas pressures', Int. J. Hydrog. Energy, vol. 32, no. 1, pp. 100–116, Jan. 2007.

[30] A. Sieverts, 'Absorption of Gases by Metals', Zeitschrift für Metallkunde, Vol. 21, pp. 37-46 1929.

[31] Chiranjib Kumar Gupta 'Thermodynamics and Kinetics', in Chemical Metallurgy, John Wiley & Sons, Ltd, pp. 225–342, 2003.

[32] B. P. Somerday and C. S. Marchi, '3 - Hydrogen containment materials', in Solid-State Hydrogen Storage, G. Walker, Ed. Woodhead Publishing, pp. 51–81, 2008.

[33] J.-G. Sezgin, C. Bosch, A. Montouchet, G. Perrin, and K. Wolski, 'Modelling and simulation of hydrogen redistribution in a heterogeneous alloy during the cooling down to 200 °C', Int. J. Hydrog. Energy, vol. 42, no. 30, pp. 19346–19358, Jul. 2017.

[34] F. Martin, X. Feaugas, A. Oudriss, D. Tanguy, L. Briottet, and J. Kittel, '8 - State of Hydrogen in Matter: Fundamental Ad/Absorption, Trapping and Transport Mechanisms', in Mechanics - Microstructure - Corrosion Coupling, C. Blanc and I. Aubert, Eds. Elsevier, pp. 171–197, 2019.

[35] A. Turnbull, '4 - Hydrogen diffusion and trapping in metals', in Gaseous Hydrogen Embrittlement of Materials in Energy Technologies, vol. 1, R. P. Gangloff and B. P. Somerday, Eds. Woodhead Publishing, pp. 89–128, 2012.

[36] H. Mehrer, Diffusion in Solids: Fundamentals, Methods, Materials, Diffusion-Controlled Processes. Berlin Heidelberg: Springer-Verlag, 2007.

[37] J.-Y. Lee and J.-L. Lee, 'A trapping theory of hydrogen in pure iron', Philos. Mag. A, vol. 56, no. 3, pp. 293–309, Sep. 1987.

[38] T. Depover and K. Verbeken, 'Hydrogen diffusion in metals: a topic requiring specific attention from the experimentalist', in Hydrogen Technologies for Sustainable Economy, vol. 2, De Gruyter, pp. 247–280, 2021.

[39] M. Dadfarnia, P. Sofronis, and T. Neeraj, 'Hydrogen interaction with multiple traps: Can it be used to mitigate embrittlement?', Int. J. Hydrog. Energy, vol. 36, no. 16, pp. 10141–10148, Aug. 2011.

[40] H. Grabke and E. Riecke, 'H. J. Grabke, E. Riecke: Absorption and diffusion of hydrogen in steels. Mater. Technol. 34(6)331(2000).

[41] S. L. I. Chan and J. A. Charles, 'Effect of carbon content on hydrogen occlusivity and embrittlement of ferrite–pearlite steels', Mater. Sci. Technol., vol. 2, no. 9, pp. 956–962, Sep. 1986.

[42] K. Takai and R. Watanuki, 'Hydrogen in Trapping States Innocuous to Environmental Degradation of High-strength Steels', ISIJ Int., vol. 43, no. 4, pp. 520–526, 2003.

[43] J. S. Kim, Y. H. Lee, D. L. Lee, K.-T. Park, and C. S. Lee, 'Microstructural influences on hydrogen delayed fracture of high strength steels', Mater. Sci. Eng. A, vol. 505, no. 1, pp. 105–110, Apr. 2009.

[44] A. H. Bott, D. S. Dos Santos, and P. E. V. De Miranda, 'Influence of cementite morphology on the hydrogen permeation parameters of low-carbon steel', J. Mater. Sci. Lett., vol. 12, no. 6, pp. 390–393, Jan. 1993.

[45] G.-W. Hong and J.-Y. Lee, 'The interaction of hydrogen and the cementite-ferrite interface in carbon steel', J. Mater. Sci., vol. 18, no. 1, pp. 271–277, Jan. 1983.

[46] McNabb, A. ; Foster, P. K., 'A New Analysis of the Diffusion of Hydrogen in Iron and Ferritic Steels', Trans Met Soc AIME, 227, pp. 618-627, 1963..

[47] B. Yang, L. Li, and L. Cheng, 'Numerical Evaluation on Analysis Methods of Trapping Site Density in Steels Based on Hydrogen Permeation Curve', Materials, vol. 13, no. 17, p. 3712, Aug. 2020.

[48] R. A. Oriani, 'The diffusion and trapping of hydrogen in steel', Acta Metall., vol. 18, no. 1, pp. 147–157, Jan. 1970.

[49] A. Turnbull, M. W. Carroll, and D. H. Ferriss, 'Analysis of hydrogen diffusion and trapping in a 13% chromium martensitic stainless steel', Acta Metall., vol. 37, no. 7, pp. 2039–2046, Jul. 1989.

[50] J. B. Leblond and D. Dubois, 'A general mathematical description of hydrogen diffusion in steels—I. Derivation of diffusion equations from boltzmann-type transport equations', Acta Metall., vol. 31, no. 10, pp. 1459–1469, Oct. 1983.

[51] J. Svoboda and F. D. Fischer, 'Modelling for hydrogen diffusion in metals with traps revisited', Acta Mater., vol. 60, no. 3, pp. 1211–1220, Feb. 2012.

[52] F. D. Fischer, G. Mori, and J. Svoboda, 'Modelling the influence of trapping on hydrogen permeation in metals', Corros. Sci., vol. 76, pp. 382–389, Nov. 2013.

[53] J. Svoboda, G. Mori, A. Prethaler, and F. D. Fischer, 'Determination of trapping parameters and the chemical diffusion coefficient from hydrogen permeation experiments', Corros. Sci., vol. 82, pp. 93–100, May 2014.

[54] E. Legrand, X. Feaugas, and J. Bouhattate, 'Generalized model of desorption kinetics: Characterization of hydrogen trapping in a homogeneous membrane', Int. J. Hydrog. Energy, vol. 39, no. 16, pp. 8374–8384, May 2014.

[55] B. Osman Hoch, A. Metsue, J. Bouhattate, and X. Feaugas, 'Effects of grain-boundary networks on the macroscopic diffusivity of hydrogen in polycrystalline materials', Comput. Mater. Sci., vol. 97, pp. 276–284, Feb. 2015.

[56] M. A. Stopher, P. Lang, E. Kozeschnik, and P. E. J. Rivera-Diaz-del-Castillo, 'Modelling hydrogen migration and trapping in steels', Mater. Des., vol. 106, pp. 205–215, Sep. 2016.

[57] Zapffe CA and Sims CE, 'Hydrogen embrittlement, internal stress and defects in steel', Trans AIME 145, pp. 225–261, 1941.

[58] A. Krom, A. Bakker, and R. Koers, 'Modelling hydrogen-induced cracking in steel using a coupled diffusion stress finite element analysis', 1997.

[59] A. Traidia, M. Alfano, G. Lubineau, S. Duval, and A. Sherik, 'An effective finite element model for the prediction of hydrogen induced cracking in steel pipelines', Int. J. Hydrog. Energy, vol. 37, no. 21, pp. 16214–16230, Nov. 2012.

[60] A. Traidia, A. M. El-Sherik, S. Duval, G. Lubineau, and J. El-Yagoubi, 'Model of Parameters Controlling Resistance of Pipeline Steels to Hydrogen-Induced Cracking', Corrosion, vol. 70, no. 1, pp. 87–94, Nov. 2013.

[61] D. M. Allen-Booth and J. Hewitt, 'A mathematical model describing the effects of micro voids upon the diffusion of hydrogen in iron and steel', Acta Metall., vol. 22, no. 2, pp. 171–175, Feb. 1974.

[62] J. Fan, L. Yan, H. Zhou, and E. Cao, 'Variation of cavity hydrogen pressure in the forming process of heavy forging', Int. J. Adv. Manuf. Technol., vol. 89, no. 5, pp. 1259–1267, Mar. 2017.

[63] J.-G. Sezgin, C. Bosch, A. Montouchet, G. Perrin, and K. Wolski, 'Modelling and simulation of hydrogen redistribution in a heterogeneous alloy during the cooling down to 200 °C', Int. J. Hydrog. Energy, vol. 42, no. 30, pp. 19346–19358, Jul. 2017.

[64] J.-G. Sezgin, C. Bosch, A. Montouchet, G. Perrin, and K. Wolski, 'Modelling of hydrogen induced pressurization of internal cavities', Int. J. Hydrog. Energy, vol. 42, no. 22, pp. 15403–15414, Jun. 2017.

[65] S.-M. Lee and J.-Y. Lee, 'Hydrogen trapping by voids in nickel', Scr. Metall., vol. 21, no. 12, pp. 1655–1658, Dec. 1987.

[66] J. L. Lee and J. Y. Lee, 'Hydrogen trapping in AISI 4340 steel', Met. Sci., vol. 17, no. 9, pp. 426–432, Sep. 1983.

[67] G. Padhy, 'Diffusible hydrogen in steel weldments - a status review', Accessed: Jun. 09, 2021. [Online].Available:https://www.academia.edu/8767562/Diffusible_hydrogen_in_steel_weldments_a_status_review.

[68] B. A. Szost, R. H. Vegter, and P. E. J. Rivera-Díaz-del-Castillo, 'Hydrogen-Trapping Mechanisms in Nanostructured Steels', Metall. Mater. Trans. A, vol. 44, no. 10, pp. 4542–4550, Oct. 2013.

[69] A. H. M. Krom and A. Bakker, 'Hydrogen trapping models in steel', Metall. Mater. Trans. B, vol. 31, no. 6, pp. 1475–1482, Dec. 2000.

[70] W. Y. Choo and J. Y. Lee, 'Thermal analysis of trapped hydrogen in pure iron', Metall. Trans. A, vol. 13, no. 1, pp. 135–140, Jan. 1982.

[71] K. C. Wong, 'Void trapping of hydrogen in sintered iron', Thesis, Jan. 09, 1976. https://digital.library.unt.edu/ark:/67531/metadc1444559/ (accessed Jun. 06, 2021).

[72] K. M. Hangos and I. T. Cameron, Eds., '4 - Constitutive Relations', in Process Systems Engineering, vol. 4, Academic Press, pp. 65–82, 2001.

[73] J.-G. Sezgin, 'Modélisation de la formation des décohésions dues à l'hydrogène dans l'acier 18MND5', PhD thesis, Université de Lyon, 2017. Accessed: Aug. 07, 2018.

[74] B. Chew, 'A Void Model for Hydrogen Diffusion in Steel', Met. Sci. J., vol. 5, no. 1, pp. 195–200, Jan. 1971.

[75] H. Hagi, Y. Hayashi, and N. Ohtani, 'Diffusion Coefficient of Hydrogen in Pure Iron between 230 and 300 K', Trans. Jpn. Inst. Met., vol. 20, no. 7, pp. 349–357, 1979.

[76] D. G. Westlake, Generalized model for hydrogen embrittlement, ASM Amer Soc Met. Trans Quart 62 1000-6Dec 1969, Jan. 1969.

[77] R. Dutton, K. Nuttall, M. P. Puls, and L. A. Simpson, 'Mechanisms of hydrogen induced delayed cracking in hydride forming materials', Metall. Trans. A, vol. 8, no. 10, pp. 1553–1562, Oct. 1977.

[78] H. K. Birnbaum, 'Second phase embrittlement of solids', Scr. Metall., vol. 10, no. 8, pp. 747–750, Aug. 1976.

[79] A. R. Troiano, 'The Role of Hydrogen and Other Interstitials in the Mechanical Behavior of Metals', Metallogr. Microstruct. Anal., vol. 5, no. 6, pp. 557–569, Dec. 2016.

[80] R. A. Oriani, 'A mechanistic theory of hydrogen embrittlement of steels', Berichte Bunsenges. Für Phys. Chem., vol. 76, no. 8, pp. 848–857, 1972.

[81] R. A. Oriani, 'Hydrogen Embrittlement of Steels', Annu. Rev. Mater. Sci., vol. 8, no. 1, pp. 327–357, 1978.

[82] C. D. Beachem, 'A new model for hydrogen-assisted cracking (hydrogen "embrittlement")', Metall. Mater. Trans. B, vol. 3, no. 2, pp. 441–455, Feb. 1972.

[83] S. P. Lynch, 'Hydrogen embrittlement (HE) phenomena and mechanisms', in Stress Corrosion Cracking, Elsevier, pp. 90–130, 2011..

[84] S. P. Lynch, 'Environmentally assisted cracking: Overview of evidence for an adsorption-induced localised-slip process', Acta Metall., vol. 36, no. 10, pp. 2639–2661, Oct. 1988.

[85] S. K. Dwivedi and M. Vishwakarma, 'Hydrogen embrittlement in different materials: A review', Int. J. Hydrog. Energy, vol. 43, no. 46, pp. 21603–21616, Nov. 2018.

[86] I. Moro, L. Briottet, P. Lemoine, E. Andrieu, C. Blanc, and G. Odemer, 'Hydrogen embrittlement susceptibility of a high strength steel X80', Mater. Sci. Eng. A, vol. 527, no. 27, pp. 7252–7260, Oct. 2010.

[87] L. Briottet, R. Batisse, G. de Dinechin, P. Langlois, and L. Thiers, 'Recommendations on X80 steel for the design of hydrogen gas transmission pipelines', Int. J. Hydrog. Energy, vol. 11, no. 37, pp. 9423–9430, 2012.

[88] Y. Jiang et al., 'Hydrogen-assisted fracture features of a high strength ferrite-pearlite steel', J. Mater. Sci. Technol., vol. 35, no. 6, pp. 1081–1087, Jun. 2019.

[89] M. Hredil, H. Krechkovska, O. Student, and O. Tsyrulnyk, 'Brittle fracture manifestation in gas pipeline steels after long-term operation', Procedia Struct. Integr., vol. 28, pp. 1204–1211, Jan. 2020.

[90] H.-L. Lee and S. Lap-Ip Chan, 'Hydrogen embrittlement of AISI 4130 steel with an alternate ferrite/pearlite banded structure', Mater. Sci. Eng. A, vol. 142, no. 2, pp. 193–201, Aug. 1991.

[91] T. Zhang, W. Y. Chu, K. W. Gao, and L. J. Qiao, 'Study of correlation between hydrogen-induced stress and hydrogen embrittlement', Mater. Sci. Eng. A, vol. 347, no. 1, pp. 291–299, Apr. 2003.

[92] J. S. Kim, Y. H. Lee, D. L. Lee, K.-T. Park, and C. S. Lee, 'Microstructural influences on hydrogen delayed fracture of high strength steels', Mater. Sci. Eng. A, vol. 505, no. 1, pp. 105–110, Apr. 2009.

[93] R. Srinivasan and T. Neeraj, 'Hydrogen Embrittlement of Ferritic Steels: Deformation and Failure Mechanisms and Challenges in the Oil and Gas Industry', JOM, vol. 66, no. 8, pp. 1377–1382, Aug. 2014.

[94] T. Neeraj, R. Srinivasan, and J. Li, 'Hydrogen embrittlement of ferritic steels: Observations on deformation microstructure, nanoscale dimples and failure by nanovoiding', Acta Mater., vol. 60, no. 13, pp. 5160–5171, Aug. 2012.

[95] M. Möser and V. Schmidt, Fractography and mechanism of hydrogen cracking. The fish-eye concept, in Fracture 84, Elsevier, pp. 2459–2466, 1984.

[96] H. Cialone and R. J. Asaro, 'Hydrogen assisted fracture of spheroidized plain carbon steels', Metall. Mater. Trans. A, vol. 12, no. 8, pp. 1373–1387, Aug. 1981.

[97] G. Vibrans, 'Fisheyes in rolled steel exposed to hydrogen at room temperature', Metall. Trans. A, vol. 8, no. 8, pp. 1318–1320, Aug. 1977.

[98] J. Sojka, J. Galland, M. Sozanska, L. Hyspecká, and M. Tvrdy, 'Contribution à l'étude du mécanisme de formation des « œils de poisson » dans les aciers', Rev. Métallurgie, vol. 97, no. 9, pp. 1083–1091, Sep. 2000.

[99] P. Adamiec and J. Dziubinski, 'Hydrogen induced cracking in welded steel tubing', Weld. Int., vol. 15, no. 6, pp. 431–437, Jan. 2001.

[100] E. D. Merson, P. N. Myagkikh, G. V. Klevtsov, D. L. Merson, and A. Vinogradov, 'Effect of fracture mode on acoustic emission behavior in the hydrogen embrittled low-alloy steel', Eng. Fract. Mech., vol. 210, pp. 342–357, Apr. 2019.

[101] E. D. Merson, P. N. Myagkikh, V. A. Poluyanov, D. L. Merson, and A. Vinogradov, 'Features of the Hydrogen-Assisted Cracking Mechanism in the Low-Carbon Steel at Ex- and In-situ Hydrogen Charging', Procedia Struct. Integr., vol. 13, pp. 1141–1147, Jan. 2018.

[102] Cialone, H., & Asaro, R. J. (1981). Hydrogen assisted fracture of spheroidized plain carbon steels. Metallurgical and Materials Transactions A volume 12, pp. 1373–1387,1981.

[103] B. Wolf, 'Application of hydrostatic weighing to density determination of tiny porous samples', Rev. Sci. Instrum., vol. 66, no. 3, p. 2578, Jun. 1998.

[104] R. Rizzo, S. Baier, M. Rogowska, and R. Ambat, 'An electrochemical and X-ray computed tomography investigation of the effect of temperature on CO2 corrosion of 1Cr carbon steel', Corros. Sci., vol. 166, p. 108471, Apr. 2020.

[105] S. Robuschi, A. Tengattini, J. Dijkstra, I. Fernandez, and K. Lundgren, 'A closer look at corrosion of steel reinforcement bars in concrete using 3D neutron and X-ray computed tomography', Cem. Concr. Res., vol. 144, p. 106439, Jun. 2021.

[106] S. C. Wu, T. Q. Xiao, and P. J. Withers, 'The imaging of failure in structural materials by synchrotron radiation X-ray microtomography', Eng. Fract. Mech., vol. 182, pp. 127–156, Sep. 2017.

[107] R. Schoell et al., 'In situ synchrotron X-ray tomography of 304 stainless steels undergoing chlorine-induced stress corrosion cracking', Corros. Sci., vol. 170, p. 108687, Jul. 2020.

[108] M. C. Remillieux et al., ‘Detecting and imaging stress corrosion cracking in stainless steel, with application to inspecting storage canisters for spent nuclear fuel’, NDT E Int., vol. 109, p. 102180, Jan. 2020, doi: 10.1016/j.ndteint.2019.102180.

[109] ‘users-guide-avizo-software-2019.pdf’. Accessed: Jun. 11, 2021. [Online]. Available: https://assets.thermofisher.com/TFS-Assets/MSD/Product-Guides/users-guide-avizo-software-2019.pdf

[110] M. A. V. Devanathan and Z. Stachurski, ‘The Adsorption and Diffusion of Electrolytic Hydrogen in Palladium’, Proc. R. Soc. Lond. Ser. Math. Phys. Sci., vol. 270, no. 1340, pp. 90–102, 1962.

[111] M. J. Danielson, ‘Use of the Devanathan–Stachurski cell to measure hydrogen permeation in aluminum alloys’, Corros. Sci., vol. 44, no. 4, pp. 829–840, Apr. 2002.

[112] S. Samanta, P. Kumari, K. Mondal, M. Dutta, and S. B. Singh, ‘An alternative and comprehensive approach to estimate trapped hydrogen in steels using electrochemical permeation tests’, Int. J. Hydrog. Energy, vol. 45, no. 51, pp. 26666–26687, Oct. 2020.

[113] P. Manolatos, M. Jerome, and J. Galland, ‘Necessity of a palladium coating to ensure hydrogen oxidation during electrochemical permeation measurements on iron’, Electrochimica Acta, vol. 40, no. 7, pp. 867–871, May 1995.

[114] A. Oudriss, F. Martin, and X. Feaugas, ‘Experimental Techniques for Dosage and Detection of Hydrogen’, in Mechanics - Microstructure - Corrosion Coupling, Elsevier, pp. 245–268, 2019.

[115] M. Ichiba, J. Sakai, T. Doshida, and K. Takai, ‘Corrosion reaction and hydrogen absorption of steel for prestressed concrete in a 20mass% ammonium thiocyanate solution’, Scr. Mater., vol. 102, pp. 59–62, Jun. 2015.

[116] M. Nagumo, K. Takai, and N. Okuda, ‘Nature of hydrogen trapping sites in steels induced by plastic deformation’, J. Alloys Compd., vol. 293–295, pp. 310–316, Dec. 1999.

[117] A. K. Belyaev, A. M. Polyanskiy, V. A. Polyanskiy, Ch. Sommitsch, and Yu. A. Yakovlev, ‘Multichannel diffusion vs TDS model on example of energy spectra of bound hydrogen in 34CrNiMo6 steel after a typical heat treatment’, Int. J. Hydrog. Energy, vol. 41, no. 20, pp. 8627–8634, Jun. 2016.

[118] E. Tal-Gutelmacher, D. Eliezer, and E. Abramov, ‘Thermal desorption spectroscopy (TDS)—Application in quantitative study of hydrogen evolution and trapping in crystalline and non-crystalline materials’, Mater. Sci. Eng. A, vol. 445–446, pp. 625–631, Feb. 2007.

[119] S. Yamasaki, T. Manabe, and D. Hirakami, ‘Analysis of Hydrogen State in Steel and Trapping Using Thermal Desorption Method’, Nippon steel and Sumitomo metal, techniqcal report no. 116, p. 6, 2017.

[120] C. V. Tapia-Bastidas, A. Atrens, and E. MacA. Gray, ‘Thermal desorption spectrometer for measuring ppm concentrations of trapped hydrogen’, Int. J. Hydrog. Energy, vol. 43, no. 15, pp. 7600–7617, Apr. 2018.

[121] J. Venezuela et al., ‘Determination of the equivalent hydrogen fugacity during electrochemical charging of 3.5NiCrMoV steel’, Corros. Sci., vol. 132, pp. 90–106, Mar. 2018.

[122] Z. Silvestri et al., ‘Thermal desorption mass spectrometer for mass metrology’, Rev. Sci. Instrum., vol. 85, no. 4, p. 045111, Apr. 2014.

[123] K. Verbeken, ‘2 - Analysing hydrogen in metals: bulk thermal desorption spectroscopy (TDS) methods’, in Gaseous Hydrogen Embrittlement of Materials in Energy Technologies, vol. 1, R. P. Gangloff and B. P. Somerday, Eds. Woodhead Publishing, pp. 27–55, 2012.

[124] M. A. Liu, P. E. J. Rivera-Díaz-del-Castillo, J. I. Barraza-Fierro, H. Castaneda, and A. Srivastava, ‘Microstructural influence on hydrogen permeation and trapping in steels’, Mater. Des., vol. 167, p. 107605, Apr. 2019.

[125] H. Husby, M. Iannuzzi, R. Johnsen, M. Kappes, and A. Barnoush, ‘Effect of nickel on hydrogen permeation in ferritic/pearlitic low alloy steels’, Int. J. Hydrog. Energy, vol. 43, no. 7, pp. 3845–3861, Feb. 2018.

[126] S. Takagi, Y. Toji, M. Yoshino, and K. Hasegawa, ‘Hydrogen Embrittlement Resistance Evaluation of Ultra High Strength Steel Sheets for Automobiles’, ISIJ Int., vol. 52, no. 2, pp. 316–322, 2012.

[127] R. W. Pasco and P. J. Ficalora, ‘The adsorption of hydrogen on iron; A surface orbital modified occupancy — bond energy bond order calculation’, Surf. Sci., vol. 134, no. 2, pp. 476–498, Nov. 1983.

[128] A. Sieverts, ‘Absorption of Gases by Metals’, Zeitschrift für Metallkunde, Vol. 21, pp. 37-46 1929.

[129] M. Pekař, ‘Thermodynamic Driving Forces and Chemical Reaction Fluxes; Reflections on the Steady State’, Molecules 2020 Jan. 2020.

[130] ‘The Transport of Diluted Species Interface’. https://doc.comsol.com/5.6/doc/com.comsol.help.battery/battery_ug_chemsptrans.09.002.html (accessed Sep. 06, 2021).

[131] M. A. Liu, P. E. J. Rivera-Díaz-del-Castillo, J. I. Barraza-Fierro, H. Castaneda, and A. Srivastava, ‘Microstructural influence on hydrogen permeation and trapping in steels’, Mater. Des., vol. 167, p. 107605, Apr. 2019.

[132] L. Cheng, L. Li, X. Zhang, J. Liu, and K. Wu, ‘Numerical simulation of hydrogen permeation in steels’, Electrochimica Acta, vol. 270, pp. 77–86, Apr. 2018.

[133] Y. Murakami, ‘21 - Hydrogen embrittlement’, in Metal Fatigue (Second Edition), Y. Murakami, Ed. Academic Press, pp. 567–607, 2019.

[134] K. Xu, ‘14 - Hydrogen embrittlement of carbon steels and their welds’, in Gaseous Hydrogen Embrittlement of Materials in Energy Technologies, vol. 2, R. P. Gangloff and B. P. Somerday, Eds. Woodhead Publishing, pp. 526–561, 2012.

[135] M. R. Louthan, ‘Hydrogen Embrittlement of Metals: A Primer for the Failure Analyst’, J. Fail. Anal. Prev., vol. 8, no. 3, pp. 289–307, Jun. 2008.

[136] Y. Liang, P. Sofronis, and N. Aravas, ‘On the effect of hydrogen on plastic instabilities in metals’, Acta Mater., vol. 51, no. 9, pp. 2717–2730, May 2003.

Appendix

The chemical potential of lattice hydrogen can be written as:

$$\mu_L = \mu_L^0 + RT \ln \frac{\theta_L}{1-\theta_L} \quad (39)$$

where μ_L^0 is the chemical potential of lattice hydrogen in a reference state and θ_L represents the occupancy of lattice sites, $\theta_L = C_L/N_L$ where C_L is the volume concentration of lattice hydrogen (m^{-3}) and N_L is the number of lattice sites per unit volume (m^{-3}). It is possible also to define the chemical potential of molecular hydrogen inside the voids

$$\mu_{H_2} = \mu_{H_2}^0 + RT \ln f_{H_2} \quad (40)$$

where $\mu_{H_2}^0$ is the chemical potential of molecular hydrogen in a reference state and f_{H_2} is the fugacity of molecular hydrogen. At equilibrium, the chemical potential of hydrogen in lattice sites is equal to the chemical potential of hydrogen in the voids

$$\mu_L^0 + RT \ln \frac{\theta_L}{1-\theta_L} = \frac{1}{2}\mu_{H_2}^0 + \frac{1}{2}RT \ln f_{H_2} \quad (41)$$

and since the occupancy of lattice sites is very low ($\theta_L \ll 1$), Eq.(41) can be simplified to

$$\mu_L^0 + RT \ln \theta_L = \frac{1}{2}\mu_{H_2}^0 + \frac{1}{2}RT \ln f_{H_2} \quad (42)$$

The hydrogen concentration in lattice sites is obtained by substituting $\theta_L = C_L/N_L$ in Eq.(42)

$$C_L = K_L\sqrt{f_{H_2}} \quad (43)$$

where $K_L = N_L \exp\left(\frac{\frac{1}{2}\mu_{H_2}^0 - \mu_L^0}{RT}\right)$. This expression represents the Sieverts' law.

In addition, the chemical potential of atomic hydrogen in trap sites (besides the voids) can be expressed as follows

$$\mu_T = \mu_T^0 + RT \ln \frac{\theta_T}{1-\theta_T} \quad (44)$$

where μ_T^0 is the chemical potential of trapped hydrogen in a reference state and θ_T is the occupancy of trap sites $\theta_T = C_T/N_T$ with C_T is the volume concentration of hydrogen in trap sites (m^{-3}) and N_T is the number of trap sites per unit volume (m^{-3}). In the same way, at equilibrium, the chemical potential of hydrogen inside the voids must be equal to the chemical

potential of hydrogen in traps ($\frac{1}{2}\mu_{H_2} = \mu_T$) and assuming that $\theta_T \ll 1$, we obtain a similar equation to Eq.(43)

$$C_T = K_T\sqrt{f_{H_2}} \tag{45}$$

where $S_T = N_T\, exp\left(\frac{\frac{1}{2}\mu^0_{H_2} - \mu^0_T}{RT}\right)$. It has to be mentioned that this equation is only valid in cases where the occupancy of trap sites is low.

Finally, considering that the "dissolved" hydrogen in the bulk is a combination of lattice and trapped hydrogen ($C_B = C_L + C_T$), it is possible to express the concentration of the "dissolved" hydrogen by combining Eq.(43) and Eq.(45)

$$C_B = K_H\sqrt{f_{H_2}} \tag{46}$$

where $K_H = K_L + K_T$. Again an equation similar to Sieverts' law is obtained, provided that the trap occupancy is low.

École Nationale Supérieure des Mines
de Saint-Étienne

NNT : 2022LYSEM003

Ahmed YAKTITI

Hydrogen-porosity interaction in a low-alloy cast steel

Speciality : Materials Science and Engineering
Keywords : Cast steel, hydrogen, diffusion and trapping, void, porosity, TDS, permeation, modelling, fish-eye.

Abstract :

The interaction between hydrogen and porosity is a key factor to understand the issue of hydrogen embrittlement in cast steels. In this work, the focus was set on the effect of porosity on hydrogen diffusion and trapping for a low-alloy cast steel. To do so, two main techniques were used: electrochemical permeation and thermal desorption spectrometry. This study is based on a comparison between porous and non-porous samples obtained from the same material.

First, it was shown that the porosity has a delaying effect on hydrogen diffusion and that the absorbed hydrogen was mainly located in porosity, which behaves as a reversible trap at room temperature. In addition, a method was proposed to estimate the hydrogen fugacity of the charging solution and the hydrogen solubility of the material. In parallel, two numerical models have been developed in order to simulate hydrogen permeation for a porous material. These two models are based on two different approaches (a non-equilibrium approach and a local equilibrium one) and take into account the trapping of gaseous hydrogen in porosity. Furthermore, a parametric study was conducted in order to investigate the role of various parameters on hydrogen diffusion. Moreover, a comparison between permeation experiments and simulations was made and a reasonable agreement was found. Then, hydrogen embrittlement was studied using H-precharged specimens, which allowed to highlight the combined effect of hydrogen and porosity on the elongation to fracture. Finally, fracture surface investigations performed on H-pre-charged porous specimens showed the presence of a special defect related to hydrogen known as “fish-eyes”. The formation of this defect was discussed in the case of low hydrogen pressures and a possible mechanism was proposed.

École Nationale Supérieure des Mines
de Saint-Étienne

NNT : 2022LYSEM003

Ahmed YAKTITI

Fragilisation par l'hydrogène de pièces de fonderie de forte épaisseur en acier faiblement allié

Spécialité: Sciences et Génie des Matériaux
Mots clefs : Acier moulé, hydrogène, piégeage et diffusion, porosité, TDS, perméation, modélisation, « œil de poisson ».

Résumé :

L'interaction hydrogène-porosité représente un facteur clé pour comprendre la problématique de fragilisation par l'hydrogène des aciers moulés. Dans ce travail, une étude comparative, entre des échantillons poreux et des échantillons non poreux du même matériau, basée principalement sur deux techniques, la perméation électrochimique et la spectroscopie de thermodesorption, a permis de mieux comprendre l'effet de la porosité dans la diffusion et le piégeage de l'hydrogène.

D'abord, il a été démontré que la porosité a un effet retardateur sur la diffusion de l'hydrogène et que l'hydrogène absorbé est principalement localisé dans la porosité, qui constitue un piège réversible à température ambiante. De plus, une méthode a été proposée pour calculer la fugacité du milieu de chargement et la solubilité de l'hydrogène dans le matériau. Ensuite, deux modèles numériques ont été développés afin de simuler la perméation de l'hydrogène dans un matériau poreux. Ces modèles, basés sur deux approches différentes, permettent de prendre compte le piégeage de l'hydrogène gazeux dans la porosité. Une étude paramétrique a été menée afin d'évaluer l'effet de certains paramètres sur la diffusion. Un accord raisonnable a été obtenu entre les expériences de perméation et les simulations numériques. Enfin, des essais de traction sur des éprouvettes pré-chargées en hydrogène ont permis d'évaluer l'effet combiné de l'hydrogène et des porosités sur la fragilisation. Ils ont aussi montré la présence d'« œil de poisson » sur les faciès de rupture du matériau poreux. Finalement, un mécanisme de formation des « yeux de poisson » a été proposé dans le cas de basses pressions d'hydrogène.